Laminar-Turbulent transition on Wind Turbines

Martinez Hernandez, Gabriel Gerardo; Sørensen, Jens Nørkær; Shen, Wen Zhong

Publication date:
2012

Laminar-Turbulent transition on Wind Turbines

by

Gabriel Gerardo Martinez Hernandez

January 24, 2011

Preface

The present dissertation is submitted in partial fulfillment of the requirement for obtaining the degree of Doctor of Philosophy in Mechanical Engineering. It is based on the research carried on during the period December 2005 to December 2010 at the Technical University of Denmark. The research was financed by DAWE, DTU, CONACYT and UDLA-P to which I express my gratitude. The research work was supervised by Professor Jens Norkær Sørensen and Associate Professor Wen Zhong Shen, who I wish to express my appreciation for their patience and support, whit out their help this project would be never be finish. I take the opportunity to extend the acknowledgement to all the members of the Fluid Mechanics section, for their support, I have been inspired by a nice international ambient that have put color and strenght to my work. I wish to extend my gratitude to the Wind energy departmet at RISØ for the good discussions in several presentations and meetings. Special thanks to professor Van Ingen and Daniel Arnal for providing relevant references, material and some indications. Among the colleges I wish to thank Jens H. Walther for the support on the development of the Databases, and also good indications for effective programing. I really appreciate the support of Martin O.L. Hansen with good discussions, and the good sense of humor always inspiring. Special recognition to Stig Øye, for the good guide he has provide to some calculations, based on solid and profound knowledge in the area. Is really appreciated the introduction to Gliders. I have learn some danish words and phrases with the secretary of the section Ruth S. Vestergaard special recognition. Thanks to my friends Wei Jun Zhu and Niels Troldborg. Thanks to God for all the strength and courage, whit out this, the project will never be finish. To my father to give me the possibility to be involved in higher education since I was very young.

To my old friends Margrethe and Alexis Millardet, for taking my family as their own. To Karen and Martin and all latin and italian friends, where I have take breath and relax after long working periods. Warm thanks to all my family in special to my shiny stars my wife Liliana and beautiful daughter Danna, they have provide light and the strongest support in difficult moments, specially for the intolerable late working hours at the office.

January 2011, Lyngby, Denmark.

Abstract

The present thesis deals with the study of the rotational effects on the laminar-turbulent transition on wind turbine blades.

Linear stability theory is used to formulate the stability equations that include the effect of rotation. The mean flow required as an input to stability computations is obtained by a similarity transformation technique. This approach allows to transform the boundary layer equations that have included the effect of the Coriolis and centrifugal forces into a set of couple partial differential equations, that are more convenient to solve numerically. The solution have been parametrized and adapted to an wind turbine rotor geometry. The blade is resolved in radial sections along which calculations are performed. The obtained mean flow is classified according to the parameters used on the rotating configuration, geometry and operational conditions. The stability diagrams have been obtained by solving the stability equations as an eigenvalue problem. The Keller box Scheme that is second order accurate was used as a numerical method. Have found to be stable and effective in terms of computing time. The solution of the eigenvalue problem provide connection between the parameters used to define the resultant wave magnitude and direction. The propagation of disturbances in the boundary layers in three dimensional flows is relatively a complicated phenomena. The report discusses the available methods and techniques used to predict the transition location. Some common wind turbine airfoils are selected to performe parametrical studies with rotational effects. Finally a wind turbine rotor is used for comparison with transition experiments. The relative motion between the flow and the blade geometry defines the response of the flow to disturbances. Have been found that flow on the suction side of the blade has a stabilizating effect, while on the region from the stagnation point to the rotor plane has a destabilizating effect on the boundary layer. The tendency is that rotational effect stabilize the boundary layer on the wind turbine blade.

Resumé

Nærværende afhandling omhandler studiet af roterende effekter på laminar-turbulent transition i strømningen omkring vindmøllevinger. Lineær stabilitetsteori bruges til at formulere de styrende stabilitets ligninger, inklusive virkningen af rotation. Det tidsmidlede strømningsfelt, som indgår i stabilitetsanalysen, beregnes ved en Falkner-Skan transformation. Denne fremgangsmåde gør det muligt at omdanne grænselagsligningerne, inklusive effekten af Coriolis og centrifugale kræfter, ind i et sæt af partielle differentialligninger, der er mere praktiske at løse numerisk. Løsningen parametriseres og tilpasses til en vindmøllerotor geometri. Det aerodynamiske profil opdeles i radielle sektioner, hvori beregningerne udføres. De opnåede gennemsnitlige strømningsfelter klassificeres i henhold til de parametre, der anvendes på den roterende konfiguration, geometri og driftsforhold. Stabilitetgrænsen bestemmes ved at løse stabilitetligningerne, som udgør et egenværdi problem.

De diskrete ligninger løses ved hjælp Keller Box metode, som er anden ordens nøjagtig. Metoden har vist sig at være stabil og effektiv med hensyn til databehandlingstid. Løsningen af egenværdiproblemet forbinder de parametre, der anvendes til at definere problemets egenværdi og egenvektor. Udbredelsen af forstyrrelser i grænselag i den tredimensionelle strømning er et forholdsvis komplekst fænomen. Rapporten diskuterer de tilgængelige metoder og teknikker, der anvendes til at forudsige overgangen placering. Nogle standard vindmølleprofiler er udvalgt i forbindelse med parametrisk undersøgelser med roterende effekter. Endelig benyttes resultaterne fra en vindmøllerotor til sammenligning med eksperimentelle resultater.

Den relative bevægelse mellem strømning og profil geometri definerer responstiden af strømningen med hensyn til forstyrrelser. Undersøgelserne viser, at strømningen på sugesiden af bladet har en stabiliserende virkning, mens der på området fra stagnationspunktet til rotorplanet er en destabiliserende effekt på grænselag. Den generelle tendens er, at roterende effekter stabiliserer grænselaget på vindmøllevinge.

Contents

List of Figures

List of Tables

List of Symbols

Roman letters

a	Induction factor on tangential direction [-]
a'	Induction factor on radial direction [-]
c^*	Local chord at given radial location r^* of the blade [m]
C_f	Friction Coefficient [-]
c^*/r^*	Local solidity of the blade [-]
Cp	Performance coefficient [-]
F_{cr}	Critical dimensional frequency [Hz]
D	Operator: diferentiation whit respect to z coordinate d/dz
f'	Dimensionless velocity in tangential direction [-]
f''	Dimensionless shear stress in tangential direction [-]
$f''(0)$	Dimensionless wall shear stress in tangential direction [-]
f'''	Difussion along the boundary layer in tangential direction [-]
g'	Dimensionless velocity in radial direction [-]
g''	Dimensionless shear stress in radial direction [-]
$g''(0)$	Dimensionless wall shear stress in radial direction [-]
g'''	Difussion along the boundary layer in radial direction [-]
i	imaginary unit
K	wavenumber resolved in the direction ψ [-]
K_0	Inverse of local solitidy [-]
H_θ	Shape factor in tangential direction [-]
H_r	Shape factor in radial direction [-]
H_x	2D Shape factor
L_{ref}	Reference lenght
m	dimensionless pressure gradient on tangential direction [-]
n	dimensionless pressure gradient on radial direction [-]
Pro	Projection of the Coriolis force [-]
P	Pressure
P'	Pressure fluctuation
R^*	Total length of the blade [m]
r, θ, Z	Cylindrical coordinates
r^*	radial position on the blade [m]
r^*/R^*	Dimensionless radial position [-]

R	Reynolds number for cartesian coordinate system * Chapter 3
Re	Reynolds number for cylindrical coordinate system * Chapter 4
Re_c	Reynolds number based on the chord of the Blade.
Ro	Rotation number [-]
Ros	Rossby number [-]
S^*	arc length coordinate [m]
S_{tr}	Transition location measured from the stagnation point along [m]
sec	Blade section
sw	sign function (+) above the rotor plane (-) below the rotor plane
U_{xf}	Dimensionless potential flow velocity [-]
U_{ref}	Reference velocity
V_{rel}	Relative velocity of the blade $[m/s]$
V_∞	Wind speed $[m/s]$
V_g	Group velocity [-]
U	Velocity along x-axis
V	Velocity along y-axis
W	Velocity along z-axis
V_r	radial velocity
V_θ	circumferential velocity
V_z	axial velocity
x, y, z	Cartesian coordinates
x_{tr}	transition location on a flat plate
$x_a = x^*/c^*$	Dimensionless airfoil coordinate in the x direction
$y_a = y^*/c^*$	Dimensionless airfoil coordinate in the y direction

Greek letters

α	complex wave number [-] in x direction * Chapter 3
α	complex wave number [-] in radial direction * Chapter 4
α_0	Angle of attack
β	complex wave number [-] in y direction * Chapter 3
$\bar{\beta}$	complex wave number [-] in circumferential direction * Chapter 4
β_w	Wall shear stress angle [$\circ$]
β_e	edge velocity angle [$\circ$]
δ_θ	Dimensionless displacement thickness in tangential direction [-]
δ_θ	Dimensionless displacement thickness in tangential direction [-]
η	Similarity variable transformation (Blasius transformation parameter) [-]
γ_0	local pitch angle [$\circ$]
γ	$\gamma = tan(\psi)$ [-]
λ_x	wave lenght in the x direction $[1/m]$
λ	Tip speed ratio [-]
ν	Kinematic viscosity $[m^2/s]$

ω	radian (circular) frequency [-]
Ω^*	Rotational frequency $[rad/s]$
ω^*	dimensional frequency $[Hz]$
ϕ_0	Inflow angle [$\circ$]
ψ	Propagation angle [$\circ$]
ρ	Density $[kg/m^3]$
θ	Inboard angle to account for curvature of the blade [-]
θ_θ	Dimensionless momentum thickness in tangential direction [-]
θ_r	Dimensionless momentum thickness in radial direction [-]
ξ	dimensioness chord position

superscripts

$(\ )^*$	Dimensional quantity.
$(\ )'$	fluctuations and derivative with respect to η
$(\ )\tilde{.}$	On the blade reference system.

subscript

$(\ )_a$	airfoil coordinate
$(\ )_c$	Based on chord length
$(\ )_{cr}$	Critical
$(\ )_e$	edge
$(\ )_i$	imaginary part
$(\ )_{max}$	maximum.
$(\ )_n$	rotated coordinate
$(\ )_0$	Velocity triangle variable
$(\ )_p$	rotor plane
$(\ )_r$	radial * in the radial direction
$(\ )_r$	real part * related with the wave numbers only
$(\ )_{ref}$	Reference
$(\ )_{tr}$	transition location.
$(\ )_w$	wall
$(\ )_{xf}$	Xfoil
$(\ )_\theta$	tangential
$(\ )_\infty$	free stream

Acronyms

2D, 3D	(Two or Three-Dimensional)

BEM	(Blade Element Momentum method)
BLE	(Boundary Layer Equation)
CF	(Cross Flow)
CFD	(Computational Fluid Dynamics)
DNS	(Direct Numerical Simulation)
FD	(Finite Difference)
FS	(Falkner-Skan)
FSC	(Falkner-Skan-Cooke)
LSP	(Local Stagnation Point)
NS	(Navier-Stokes)
ODE	(Ordinary Differential equation)
PDE	(Partial Differential equation)
RE	(Rotational effects)
RFP	(Rotating Flat Plate)
TS	(Tollmien-Schlichting)
VP	(Velocity profile)

Chapter 1

Introduction

The main interest of the dissertation is to understand and model the effect of rotation on the stability of the boundary layer on a wind turbine blade. The intricate geometry and characteristics of the flow makes attractive the use of methods which are non expensive in terms of resources and computing time, and that can be coupled to a Navier-Stokes (NS) flow solver. Actually, most of the Computational Fluid Dynamics (CFD) codes assume that the boundary layer is completely turbulent or employ inadequate or oversimplified criteria for the prediction of the laminar-turbulent transition, and, as a result, tend to over predict the lift, under predict the drag force and fail to give the correct stall angle. The Database technique have been used effectively for 2D flows by Stock and Degenhart [106], however, the extension of this technique for rotational effects is not simple and requires a careful examination of the relation among the boundary layer parameters, such that the number of input velocity profiles for stability calculations is reduced and the size of the database is minimized. One of the critical parts is to specify the parameter range for the study, this needs to be related to the geometry and operational conditions of the blade. The solution of the boundary layer equations is based on the concept of similarity, which allows to transform the nature of Boundary Layer equations (BLE) that are Partial Differential equations (PDE) into an set of Ordinary Differential equations (ODE). The classical example is the Blasius flow over a flat plate. In practice the flow over rotating airfoils is non similar due to history effects created by the geometry, the operational conditions and the body forces.

The relative direction of the flow with respect to the motion of the rotor blade needs to be considered, as explained in the solution of the boundary layer equations over a rotating airfoil. This flow differs in complexity from the classical cases, like the rotating disk and the rotating channel flow. On the wind turbine blade both sides of the geometry need to be considered.

The boundary layer approximation is not valid after separation, and can not be used in the separation region. An approximation has been made by

Dumitrescu and Cardos [30]. The formal approach to model this region is to have a strong coupling between the viscous and inviscid solution Sørensen [107]. For transition prediction, however, some effort have been directed to obtain an approximate shape of the velocity profiles as suggested by Olsen [79] for the 2D case. In a similar manner the work of Pedersen provides the 2D solution on the attachment flow region.

Once the mean flow is calculated, the velocity profiles are mapped and stored in a Database. The next step is to perform stability calculations. A review of available transition techniques by the use of linear stability theory can be found in Reed et al. [86], Reed and Saric [87], the fundamentals of the e^n method is detailed explained by van Ingen [46] and van Ingen [47]. In similar manner the review of Arnal and Casalis [7], Arnal [6] and Arnal [8] provides the extension of the e^n method to three dimensional flows.

Mack [64] obtained simplified methods for transition prediction, of which some provide the basis for actual transition techniques. Mack [65] reviewed the available numerical methods for solving the stability equations. Determins the boundary condition with rotational effect is not a simple task and requires careful treatment, specially because it is not simple to localize the edge of the boundary layer, see McCroskey and Dwyer [74]. The numerical method plays a crucial part when dealing with stability calculations, and for that purpose the Keller box scheme Keller [51] provides a strong support on the solution of the stability equations, allowing a fast solution.

The approach for transition prediction was essentially developed in work done in the aircraft industry: swept wings Schrauf [92], Schrauf [93], Schrauf [94] and helicopter blades McCroskey [73], Fogarty [33], Tanner and Yaggy [110], Franklin [34], Blaser and Velkoff [12] and rotational machinery, ship propellers Mikkelsen et al. [77]. Another example is the prolate spheroid, that has been used as standard test case due to the fact that experimental data are available, Meier and Kreplin [76], Kreplin et al. [52]. For this particular case computations have been performed for transition prediction Stock [105], Cebeci [18], Cebeci et al. [19]. The previous cases differs in the kind of similarity to obtain the mean flow and the active linear terms in the stability equations, some rotate while other do not, but will have 3D features, some numerical techniques can be taken. The incoming turbulence intensity will differ in each case, for instance, on fly conditions the incoming turbulence level to the wing of the airplane are even lower that the ones found on a wind tunnel facility, in contrast with the incoming turbulence level on the wind turbine rotor area or the rotating machinery.

The closest experimental work that include rotational effects (RE)are the channel flow by Matsson and Alfredsson [71], and Alfredsson and Persson [2], the rotating disk by Lingwood [61] and Lingwood [60], and the flow visualization of Masuda and Matsubara on the rotating flat plate [69]. Although these experiments do not represent the real solution on a wind turbine blade, they give an indication of the effect of rotation on the stability of the bound-

ary layer. Very recent experimental data and results have been presented in Madsen et al. [67]. Unfortunately these data were not available at the time when this report was written. It is important to mention that inherent to the linear stability theory and the e^n method is implicit an error, however some results will be shown. Since full Direct Numerical Simulations (DNS) solutions and experiments at the present time can only be obtained for very specific cases and conditions, and due to the fact that the wind turbine is operating over a very different flow regimes and conditions, the use of simplified methods makes it attractive to incorporate in the design tools. To have a clear overview of the transition process the following figure is used:

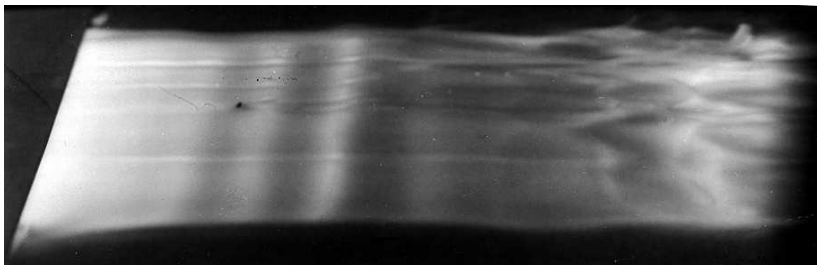

Figure 1.1: 2D Water Channel Flow visualization - ONERA

Taking as reference figure 1.1, it is possible to distinguish a sequence of processes, receptivity describe the means by which disturbance in the freestream, like sound or vorticity enter into the boundary layer. Instabilities can be induced by: the roughness, geometry and characteristics of the surface or its vibration. The path that the flow follows depends on the disturbance level. At the lower level the flow passes to a sequence of well defined states, the first part constitutes the growth of the Tollmien Schichting (TS), Gortler or Crossflow (CF) mechanisms, then a sequence of linear of process: transient growth, eigenmode growth, the non-linear part occurs when the parametric instabilities and mode interactions are dominant and the last stage is the breakdown with the formation of the Emmons spots and the turbulent flow Reshotko [88].

Rigorous modeling of this process is out of the actual capabilities, however transition prediction is required for design purposes. Besides the practical application, it is relevant to understand the physics behind the propagation of the disturbances in the boundary layer.

The report is written in the following form: In Chapter 2 the solution of the boundary layer equations in a rotating reference frame is presented and relations among the boundary layer parameters are obtained. Chapter 3 considers the study of the 2D Database, furthermore, it provides the analysis, and discuss the relation among the stability paramenters and the solution of the stability equations. Chapter 4 is the main motivation of the

project, discusses the formulation of the stability equations with rotational effects and the respective boundary conditions, that in the cases of rotating blade represent a major challenge. Some explanations are provided to the techniques and methods available to calculate transition. Each chapter provides extension of relevant references. The rotating flat plate case has provided some light into the effect of rotation on the stability of the boundary layer. On Chapter 5 a parametrical analysis is made for some of the most common airfoils used for wind turbines, and, in a similar manner, a real wind turbine blade is taken to perform full analysis. Finally, a summary of results and suggestions to improve the solution are presented.

Chapter 2

Boundary layer formulation

This Chapter provides the formulation of the Navier-Stokes (NS) equations on a wind turbine rotor. The method to solve the boundary layer equations by the use of similarity variables is presented, special atention is given to the formulation of the boundary condition, the obtained solution is parametrized and mapped in a Database that include rotational effects. Some of the velocity profiles from the Database are presented one case with positive pressure gradient, another on the negative gradient zone, close to the separation and the special case the rotating flat plate, that will be used extensively on this report. The work done on this chapter will be used as base flow for stability and transition prediction computations.

2.1 Governing equations

In order to study the rotational effects, the governing equations are written in a frame that rotates around the z^*-axis with a constant angular velocity Ω^*. The origin of the coordinate system is chosen at the rotor center and the radial axis passes through 1/4 chord position of a cross section from the leading edge, the velocity components along the radial direction of the blade is denoted V_r^*, V_θ^* is directed in the circumferencial direction, and V_z^* is aligned with the axis of rotation. To obtain the momentum and continuity equations relative to the blade, and considering that the flow passes over the blade, the following equation may be written:

$$\begin{pmatrix} \tilde{V}_r^* \\ \tilde{V}_\theta^* \\ \tilde{V}_z^* \end{pmatrix} = \begin{pmatrix} V_r^* \\ V_\theta^* \\ V_z^* \end{pmatrix} - \begin{pmatrix} 0 \\ \Omega^* r^* \\ 0 \end{pmatrix} \tag{2.1}$$

(for purpose of clarity asterisk indicates a dimensional quantity). To be able to describe the flow on the wind turbine blade, both sides of the geometry are considered, in contrast with the rotating disk where only one

side is used, this evidently make the formulation much more complicated. On the pressure side the blade Ω^* rotates in clockwise direction, from the local stagnation point (LSP) the follow will follow two paths, one to the rotor plane where V_θ^* is positive (region I) and the other to the trailing edge (region III), on this direction V_θ^* takes negative value. Once the flow has pass the rotor plane, on the suction side the blade, Ω^* rotates in counterclockwise direction and V_θ^* is negative , the zone is designated by (region II). The circumferential velocity can be written as $\tilde{V}_\theta^* = \theta^* - \Omega^* r^*$ for region I and II and $\tilde{V}_\theta^* = \Omega^* r^* - V_\theta$ for region III. The incoming wind velocity V_∞^* is pointing in the positive direction of z^* as shown in figure 2.1, for purpose of clarity the corresponding regions are visible on the reference system . Once the equations are formulated on the blade reference system the body forces appears in the r and θ momentum equations while the z momentum equation remains unchanged.

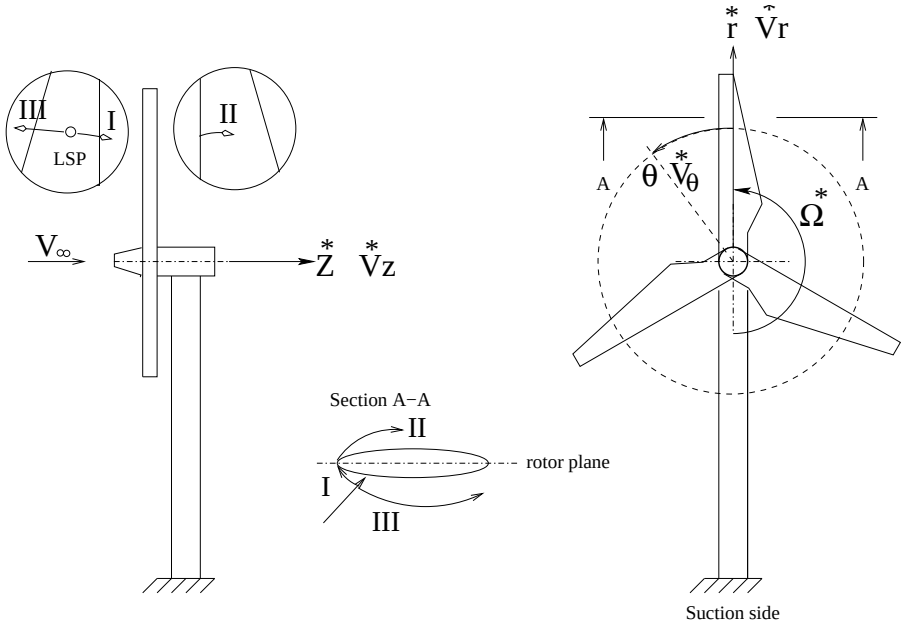

Figure 2.1: General wind turbine reference system

$$\frac{\partial \tilde{V}_r^*}{\partial r^*} + \frac{\tilde{V}_r^*}{r^*} + \frac{1}{r^*}\frac{\partial \tilde{V}_\theta^*}{\partial \theta} + \frac{\partial \tilde{V}_z^*}{\partial z^*} \tag{2.2}$$

$$\frac{\partial \tilde{V}_r^*}{\partial t^*} + \tilde{V}_r^*\frac{\partial \tilde{V}_r^*}{\partial r^*} + \frac{1}{r^*}\tilde{V}_\theta^*\frac{\partial \tilde{V}_r^*}{\partial \theta} + \tilde{V}_z^*\frac{\partial \tilde{V}_r^*}{\partial z^*} - \frac{1}{r^*}\left(\tilde{V}_\theta^* - \Omega^* r^*\right)^2 = \tag{2.3}$$
$$-\frac{1}{\rho^*}\frac{\partial \tilde{P}^*}{\partial r^*} + \nu^*\left[\Delta \tilde{V}_r^* - \left(\frac{1}{r^*}\right)^2\left(\tilde{V}_r^* + 2\frac{\partial \tilde{V}_\theta^*}{\partial \theta}\right)\right]$$

$$\frac{\partial \tilde{V}_\theta^*}{\partial t^*} + \tilde{V}_r^* \frac{\partial \tilde{V}_\theta^*}{\partial r^*} + \frac{1}{r^*}\tilde{V}_\theta^* \frac{\partial \tilde{V}_\theta^*}{\partial \theta} + \tilde{V}_z^* \frac{\partial \tilde{V}_\theta^*}{\partial z^*} + \frac{1}{r^*}\tilde{V}_r^* \left(\tilde{V}_\theta^* - 2\Omega^* r^*\right) = \quad (2.4)$$
$$-\frac{1}{\rho^* r^*}\frac{\partial \tilde{P}^*}{\partial \theta} + \nu^* \left[\Delta \tilde{V}_\theta^* - \left(\frac{1}{r^*}\right)^2 \left(\tilde{V}_\theta^* - 2\frac{\partial \tilde{V}_r^*}{\partial \theta}\right)\right]$$

$$\frac{\partial \tilde{V}_z^*}{\partial t^*} + \tilde{V}_r^* \frac{\partial \tilde{V}_z^*}{\partial r^*} + \frac{1}{r^*}\tilde{V}_\theta^* \frac{\partial \tilde{V}_z^*}{\partial \theta} + \tilde{V}_z^* \frac{\partial \tilde{V}_z^*}{\partial z^*} = -\frac{1}{\rho^*}\frac{\partial \tilde{P}^*}{\partial z^*} + \nu^* \left[\Delta \tilde{V}_z^*\right] \quad (2.5)$$

2.2 Boundary layer equations

The procedure to simplify the previous (NS) equations is to estimate the order of magnitude of the terms. Following the approach of Prandtl, on the formulation of the equations it is found that the shear stress variation along the radial and circumferential directions is small in comparison with the normal coordinate, meaning that the diffusion of vorticity on the boundary layer takes place mainly along the normal coordinate to the surface of the geometry. Neglecting the pressure variation along the normal coordinate, the z momentum equations degenerates to a simple expression, implying a constant pressure across the boundary layer. Assuming constant inflow and steady flow properties, the time derivatives are neglected from the equations. Finally terms scaling as $1/r^{*2}$ are neglected from the momentum equations, and we end up with the following set of equations

$$\frac{\partial \tilde{V}_r^*}{\partial r^*} + \frac{\tilde{V}_r^*}{r^*} + \frac{1}{r^*}\frac{\partial \tilde{V}_\theta^*}{\partial \theta} + \frac{\partial \tilde{V}_z^*}{\partial z^*} = 0 \quad (2.6)$$

$$\tilde{V}_r^* \frac{\partial \tilde{V}_r^*}{\partial r^*} + \frac{\tilde{V}_\theta^*}{r^*}\frac{\partial \tilde{V}_r^*}{\partial \theta} + \tilde{V}_z^* \frac{\partial \tilde{V}_r^*}{\partial z*} = -\frac{1}{\rho^*}\frac{\partial \tilde{P}^*}{\partial r^*} + \nu^* \frac{\partial^2 \tilde{V}_r^*}{\partial z^{*2}} + \frac{(\tilde{V}_\theta^* - \Omega^* r^*)^2}{r^*} \quad (2.7)$$

$$\tilde{V}_r^* \frac{\partial \tilde{V}_\theta^*}{\partial r*} + \frac{\tilde{V}_\theta^*}{r^*}\frac{\partial \tilde{V}_\theta^*}{\partial \theta} + \tilde{V}_z^* \frac{\partial \tilde{V}_\theta^*}{\partial z^*} = -\frac{1}{\rho^* r^*}\frac{\partial \tilde{P}^*}{\partial \theta} + \nu^* \frac{\partial^2 \tilde{V}_\theta^*}{\partial z^{*2}} + 2\Omega^* \tilde{V}_r^* - \frac{\tilde{V}_\theta^* \tilde{V}_r^*}{r^*} \quad (2.8)$$

The common way to solve the boundary layer equations is to find a similarity variable to transform the equations. By looking at the property of scale, two velocity profiles located at different positions are similar if they differ by a scale factor on the velocity component and the normal coordinate. This can simplify the solution by reducing the number of independent variables such that the partial differential equation can be transformed into an (ODE). The best example is the Blasius profile on a flat plate. Hansen [41] explained in great detail various methods and techniques that can be used

for boundary layer flows such as free parameter, separation of variables and group-theory method. Hansen and Herzig [40] formulated the 3D boundary layer equations in stationary Polar coordinates. The first attempt to test the numerical method was to calibrate with a known solution including 3D effects. In Yohner and Hansen [115], several cases were used for validation.

Cooke and Hall [25] gives a summary of the first approximation to 3D boundary layers. The inconvenience of the work is that rotational effects are not included and many of the solutions have been obtained for developable surfaces, such as cylinders or cones, with Gaussian curvature equal to zero. The flow over a rotating airfoil is non-similar. Dumitrescu and Cardos [29] presented a similarity approach to solve the three-dimensional boundary layer of a rotating flat plate. Considering a sectional cut, the similarity formulation was achieved for a flat plate aligned with the azimuth direction in the cylindrical coordinates. Since a flat plate wing is not used for wind turbines, it is thus needed to develop a technique to solve the three-dimensional boundary layer of a wind turbine wing by using a similar approach.

2.2.1 The role of the coordinate system

One of the complications with the present technique is that, in order to solve the differential boundary layer equations (BLE), it is needed to find a similarity variable to regroup the equations and then integrate them using some numerical techniques. Unfortunately, it is very difficult or even impossible to find a common similarity variable for 3D boundary layer equations on a rotating blade. The choice of reference system is crucial to obtain a solution. For some coordinates the transformation can not be applied. The formal way to solve the equations is to write them in a coordinate system that follows the curvature of the blade, this is normally done when a solution from a (NS) flow solver is taken and written in the form of the transformation parameters. If a 2D test is taken as an example, it is necessary to transform the equations into a different plane where curvature is included. This is the classical Falkner-Skan transformation on the Mangler transformed flow where the effect of the curvature is taken into account, a detailed derivation can be found on Cebeci and Bradshaw [14]. Once on this plane the similarity transformation can be applied. The parallel flow assumption is used to derive the stability equations, which is questionable to include the the in-plane curvature on the mean flow.
When using a non-orthogonal coordinate system, the shape of the similarity transformation will be the same except that more terms will be included in the expressions. The geometric parameters such as the metric coefficients and geodesic curvature of the coordinate lines appearing in the 3D (BLE) must be known prior to boundary layer calculations for a given free stream conditions and inviscid velocity distribution. A detailed derivation was made by Sørensen [107].

2.3 Derivation of the equations using similarity variables

The first step in the similarity analysis is to write the dependent variables in the form of product of functions in such a way that the similarity variable is involved:

$$\frac{\tilde{V}_\theta^*}{U_{xf}V_{rel}^*} = \frac{\partial f}{\partial \eta} = f'(\xi,\eta) \tag{2.9}$$

$$\frac{\tilde{V}_r^*}{U_{xf}V_{rel}^*} = \frac{\partial g}{\partial \eta} = g'(\xi,\eta) \tag{2.10}$$

On the previous equations the dimensionless variables f' and g' are a function of the tangential and radial similarity variables, U_{xf} is the dimensionless velocity obtained from a potential or viscous flow solver, for instance obtained with Xfoil, Drela[27], and V_{rel}^* is the relative velocity. The similarity variable used in the tangential direction is the Blasius transformation parameter (2.11).

$$\eta = z^*\sqrt{\frac{U_{xf}V_{rel}^*}{x^*\nu^*}} \tag{2.11}$$

$$\xi = \frac{r^*\theta}{c^*} = \frac{x^*}{c^*} \tag{2.12}$$

In the case of a rotating blade another expression is used to account for the similarity in the radial direction. From equation (2.12) the coordinate θ scales with the inverse of the local solidity c^*/r^*, (where c^* is the local chord of the blade and r^* the respective radious at that location), which is also used to make dimensionless the chord of a blade cross-seciton.

Applying the transformation parameters (2.9),(2.10),(2.11),(2.12) to equations (2.7),(2.8) and multiplying by the factor $\frac{x^*c^*}{c^*(U_{xf}V_{rel}^*)^2}$ yield the transformed system of (PDE) equations:

$$f''' + 0.5ff'' + \xi f_\xi f'' + \frac{c^*}{r^*}\xi g f'' - \xi f'_\xi f' + m\left(1 + 0.5ff'' - f'^2\right) + n\left(0.5f'' - f'g'\right) + \frac{c^*}{r^*}s_w\xi g'\left(\frac{2RoP_{ro}}{U_{xf}} - f'\right) + s_w g''\frac{\theta}{2}g + s_w\xi\theta g'' g_\xi - s_w\xi\theta g' g_\xi = 0 \quad (2.13)$$

$$g''' + 0.5fg'' + \xi f_\xi g'' + \frac{c^*}{r^*}\xi g g'' - \xi g'_\xi f' + m\left(0.5fg'' - f'g'\right) + n\left(\frac{1}{U_{xf}} + 0.5gg'' - g'^2\right) - \frac{c^*}{r^*}\xi f'\left(\frac{2Ro}{U_{xf}} - f'\right) - \frac{c^*}{r^*}\xi g' f' + s_w f''\frac{\theta}{2}g + s_w\xi\theta f'' g_\xi - s_w\xi\theta g' f'_\xi = 0 \quad (2.14)$$

where $\theta = (\xi - 0.25)\frac{c^*}{r^*}$

The set of equations (2.13), (2.14) was first derived by Dumitrescu and Cardos [29]. During the project the equations have been modified an parametrized to a wind turbine rotor. The θ terms does not appear on the original formulation, however, was used to test the effect of this extra terms, specially close to the rotating axis. Is important to note that the Reynolds number does not appear in the equations.

2.3.1 Input parameters for the solution of the system of (PDE)

The local rotation number Ro is defined as the ratio between the rotational velocity and the relative velocity of the blade.

$$Ro = \frac{\Omega^* r^*}{V^*_{rel}} = \frac{K_o}{Ros} = \frac{\lambda\frac{r^*}{R^*}}{\sqrt{\left(\lambda\frac{r^*}{R^*}\right)^2 + 1}} \quad (2.15)$$

Where λ is the tip speed ratio. Manipulating the expression can also be equivalent to the inverse of Rossby number Ros times the inverse of the local solidity of the blade K_o.
To calculate the pressure changes on tangential and radial direction the following parameters are used:

$$m = \frac{c^*}{r^*}\frac{1}{U_{xf}V^*_{rel}}\frac{\partial U_{xf}V^*_{rel}}{\partial\theta}\xi = \frac{x^*}{U_{xf}}\frac{dU_{xf}}{dx^*} = \frac{\xi}{U_{xf}}\frac{dU_{xf}}{d\xi} \quad (2.16)$$

$$n = \frac{c^*}{U_{xf}V^*_{rel}}\frac{\partial U_{xf}V^*_{rel}}{\partial r^*}\xi = \frac{c^*}{r^*}Ro^2\xi \quad (2.17)$$

The dimensionless pressure parameter in the tangential direction m describes the acceleration of the flow, which is clearly dependent on the geometry of the airfoil, the position on the blade, and the operational conditions. (This parameter can be related to the Cp). The parameter n characterizes the pressure variation in the radial direction and in contrast with the parameter m, does not depend on the curvature. To derive equations (2.15),(2.16) and (2.17), have been assumed that the induction factors in the tangential and radial direction are zero (ideal case with out energy losses). It should be point out that to obtain the Database of velocity profiles whit (RE) is not needed to know this parameters. Once a real case or aplication is defined, the Database can be accessed with the corrected values from equations (2.15),(2.16) and (2.17) that include the induction factors, for that pourpose interpolation among the families of (VP) is required.

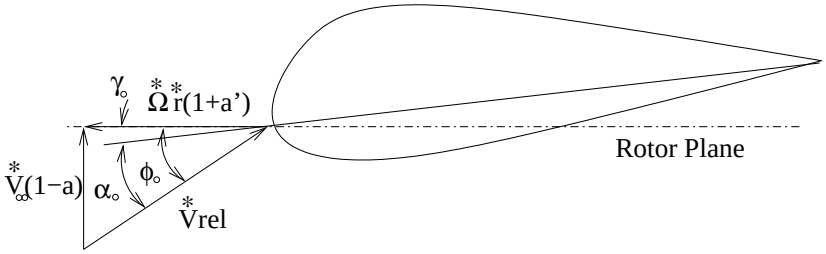

Figure 2.2: Velocity triangle at rotor plane

According to the flow triangle in figure 2.2, it can be shown that the inflow angle ϕ_o can be related to the rotation number by the following equation

$$\phi_o = cos^{-1} Ro \tag{2.18}$$

At some given radial location on the blade, the terms α_o represent the local angle of attack, while γ_o the local pitch angle of the blade. The induction factors, axial and tangential are respectively a and a' at that section. The wind velocity is designated by V_∞^* and the rotational frequency by Ω^*.

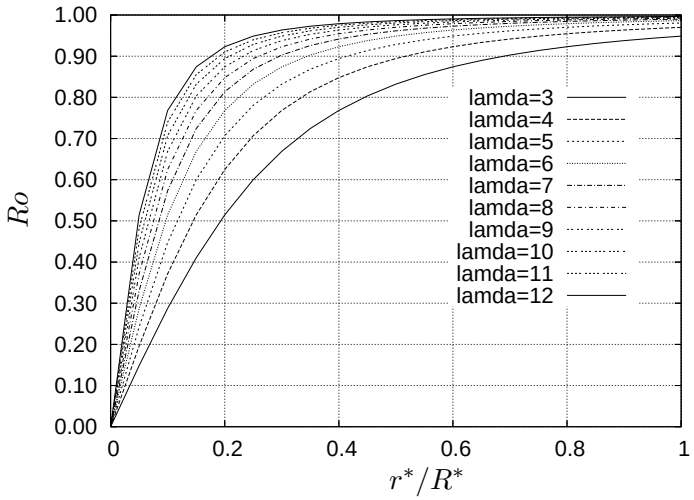

Figure 2.3: Rotation number as function of radial positions at various tip speed ratios

In figure (2.3) is shown the variation of the local rotation number Ro at different tip speed ratios λ as function of dimensionless position r^*/R^* along the blade span. The range of the rotation number for a wind turbine rotor is approximately $Ro \in$ [0.5-1], as the inner part of the rotor normally is of no importance for the performance. The local solidity c^*/r^* is given in the range $\in$ [0-0.35], the range for the dimensionless pressure gradient can be taken from $\in$ [1.935:-0.0908]. In practice the blade is operating at a rotational number close to 1.

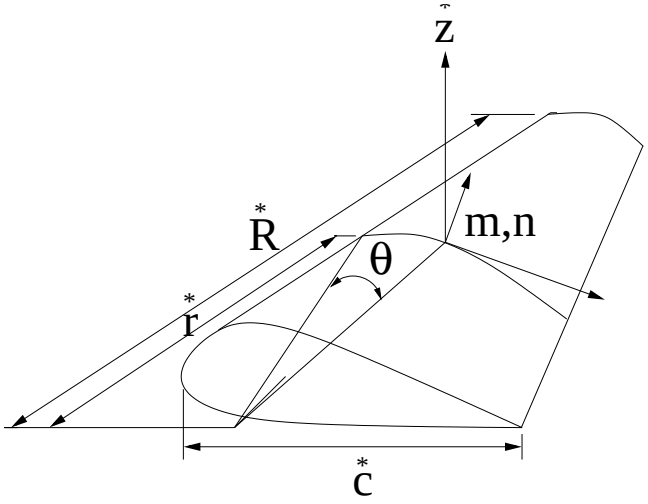

Figure 2.4: Squematic representation of the variables used to solve the set of equations on the transformed (FS) plane

2.3.2 Characteristics of the system of (PDE)

The main feature of the boundary layer equations is that they are parabolic in both the tangential and radial direction. Thus, due to the independence principle of the radial component of the inviscid flow, the overall problem is elliptic in the tangential direction and parabolic along the radious of the wing. Taking advantage of this property much computing time is saved by completing the solution at one cross section before marching to the next.

The previous system represents a coupled set of Partial Differential Equations, the terms f_ξ,f'_ξ,g_ξ,g'_ξ represent the so called memory of the flow, and makes the equations a (PDE) system, both in tangential and radial directions. As the value of c^*/r^* tends to zero the rotational effects have less effect on the solution of the (BLE). If $c^*/r^* = 0$ is set rotational effects are cancelled out, and the set reduces to the Falkner-Skan equations with history effect (one possible way to think about the memory is replacing the word by inertia due to acceleration of the flow). For some cases this acceleration or memory can suppress the breakdown of the (BLE) on the laminar separation bubble. For a real airfoil, however, in this region is needed a strong viscus-inviscid interaction to calculate the correct pressure gradient, and can not just be calculated from the potential flow around the airfoil. If the pressure gradient is kept constant on the 2D flow, then the solution at different ξ locations will be exactly the same, and the memory will not have effect. In this case our initial condition from the solution of the Falkner-Skan equation will be preserved. The Blasius solution for a flat plate is recovered when $m = 0$. If non zero values are allowed for the parameter c^*/r even when the

value of m is keep constant along the chord, or the marching taking place from $\xi = 0$ to $\xi = 1$, the memory terms on both equations will be active due to the fact that the rotational effects are playing a role on the solution of the coupled set of (PDE). The extra θ terms in the equations account for the curvature on the streamlines close to the inboard locations.

2.3.3 Position of the rotor plane

To be able to define the position of the rotor plane the following set of equations is used:

$$x_n = x_a cos(\gamma_o) - y_a sin(\gamma_o) \tag{2.19}$$

$$y_n = y_a cos(\gamma_o) + x_a sin(\gamma_o) \tag{2.20}$$

$$r_p = min(x_n) \tag{2.21}$$

$$P_{ro} = \left| cos\left(atan\left(\frac{dy}{dx}\right) - \gamma_o \right) \right| \tag{2.22}$$

On the equations (2.19) and (2.20) the coordinates (x_a, y_a) represent the airfoil geometry on a cartesian reference system, while (x_n, y_n) the rotation of the coordinates according to pitch angle . On equation (2.21) r_p represent the minimum value of x_n, this clearly indicates the position of the rotor plane. This equations allows to distinguish between the regions I,II and III from figure 2.1. The sign function s_w is negative below rotor plane on the pressure side and positive above, is found from equation 2.21. On given airfoil the direction of the Coriolis force and the circumferential velocity are not the same as mentioned in section 2.1, is also compulsory to project the Coriolis force according to the position on the blade, the angle of attack and the inflow angle.

The next step is to rotate the airfoil according to the angle between the rotor plane and the chord line going from the leading edge to the trailing edge see figure 2.2.

The term P_{ro} on equation(2.13) and (2.22) account for the projection of the Coriolis force.

2.3.4 Output parameters from the solution of the system of (PDE)

The skin friction coefficient $f''(0)$ and $g''(0)$ can be taken directly from the solution of the set of equations (2.13) and (2.14) evaluated at the wall of the boundary layer:

$$f''(0) \equiv \frac{1}{2} C_{f,V_\theta} \sqrt{Re_x} \tag{2.23}$$

$$g''(0) \equiv \frac{1}{2} C_{f,V_r} \sqrt{Re_x} \tag{2.24}$$

The wall shear stress angle β_w can be found by combining the previous definition:

$$\beta_w = atan\left(\frac{g''(0)}{f''(0)}\right) \tag{2.25}$$

To adapt to a real geometry with curvature, the boundary condition, as will be discussed in section 2.3.5, results in an angle that depends on the radial pressure gradient

$$\beta_e = atan\left(\frac{g'(\infty)}{f'(\infty)}\right) \tag{2.26}$$

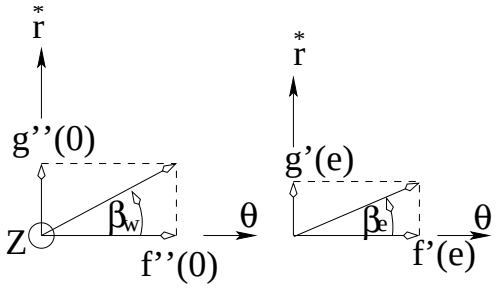

Figure 2.5: a) Skin friction angle b) Edge velocity angle

The previous angles have been calculated at the wall and edge of the boundary layer, and it is easily to extended all the boundary layer. To give an idea of the relative magnitude of the Coriolis and centrifugal forces, this gives an indication of the propagation of the disturbances.

Using the similarity variables the dimensionless displacement and momentum thickness in the tangential and radial directions are written as:

$$\delta_\theta = \int_0^\eta (1 - f')d\eta \tag{2.27}$$

$$\delta_r = -\int_0^\eta g' d\eta \tag{2.28}$$

$$\theta_{\theta\theta} = \int_0^\eta f'(1 - f')d\eta \tag{2.29}$$

$$\theta_{\theta r} = \int_0^\eta g'(1 - f')d\eta \tag{2.30}$$

$$\theta_{r\theta} = -\int_0^\eta f'g'\eta \tag{2.31}$$

$$\theta_{rr} = -\int_0^\eta g'g'\eta \tag{2.32}$$

$$H_{\theta\theta} = \frac{\delta_\theta}{\theta_{\theta\theta}} \tag{2.33}$$

$$H_{r\theta} = \frac{\delta_r}{\theta_{r\theta}} \tag{2.34}$$

Equation (2.27) and (2.28) represents the dimensionless displacement thickness in the tangential and radial directions respectively. The calculation of the dimensionless momentum thickness for the considered coordinates can be done in two different ways. The first is taking as reference the same tangential direction as shown on equations (2.29) or the radial direction as seen on(2.30). The same concept is used for the radial direction according to equations (2.31) or (2.32). The equations (2.27)-(2.32)have been adapted to the solution of the equations (2.13) and (2.14).

One characteristic of the rotational effect is the presence of the cross flow velocity profile. The next figure is used to parametrize the solution. The variable g'_{max} represents the maximum value of g' while η_{cr} the position of the inflection point, finally ge' describe the value of g' at which the velocity profile tend towards the leading edge where the similarity variable η takes the maximum value η_{max}.

2.3.5 Boundary condition

Regarding the boundary conditions some modifications with respect to the original formulation were found necessary. The original boundary conditions are $f = 0, f' = 0, g = 0, g' = 0$ at the wall $\eta = 0$, and at the edge of the boundary layer as $\eta \to \infty$ $f' = 1, g' = 0$. To set the correct pressure gradient it is difficult to set the cross flow zero at the edge of the boundary layer. Then instead of fixing the value of cross flow zero at the edge, we use the radial shear stress zero at the edge of the boundary layer $g''(\eta = \infty) = 0$, which is

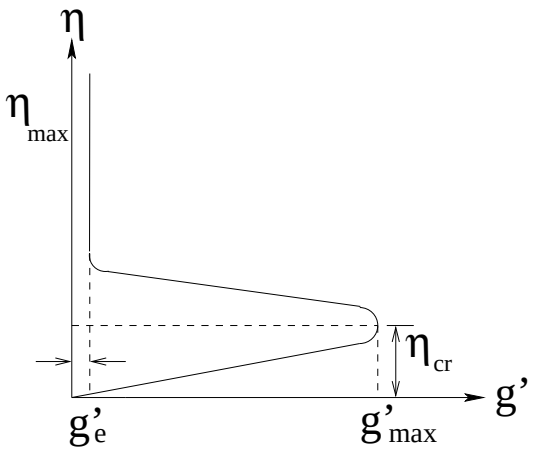

Figure 2.6: Sketch of the Cross flow velocity profile

more physical. Then the velocity profile go smoothly towards the edge of the boundary layer following a normal trajectory and it is not further needed to specify an additional condition to compensate from the misaligment with the normal path form the surface. This is very important for transition prediction since disturbances should damp out as the edge of the boundary layer is approached. However, for the case of a Integral formulation it is not possible to impose this condition on the solution. Instead an approximate expression is used to fix this boundary condition. McCroskey and Dwyer mentioned [74] that it is somehow difficult to find the edge condition on rotating boundary layers.

2.4 Principle of radial similarity and calculation of the potential flow

The core of the quasi 3D approximation is to obtain a simplified solution that retains the important features of the rotation of the flow and at the same time is capable of producing good results. The flow is solved in a 2D manner while keeping all the essential 3D information. The marching procedure takes place along a constant value of c^*/r^*. On a given rotating airfoil it is a requirement to calculate the potential flow (that enters in the parameter m) to be able to solve the equations. By considering an infinite cylinder with arbitrary cross section rotating at a constant angular velocity, about an axis normal to it, it was shown by Sears [97] that the inviscid velocity components could be expressed as:

$$V_\theta^* = \Omega^* r^* \frac{\partial \phi}{\partial x^*} \tag{2.35}$$

$$V_z^* = \Omega^* r^* \frac{\partial \phi}{\partial z^*} \tag{2.36}$$

$$V_r^* = \Omega^* [\phi - 2x^*] \tag{2.37}$$

In the equation $\phi = \phi(\theta, z)$ represents the equivalent 2D potential due to a blade in translational motion with a unit speed in the negative x direction. It is interesting that the inviscid spanwise velocity potential can be given by a simple expression that depends entirely on the 2D equivalent velocity potential. Even if the blade advances in the direction of the axis of rotation, it can be shown that the set of equations is unaltered, Fogarty and Sears [32]. In the case of the transformed equations (2.13),(2.14) the principle of similarity can be explained by considering a constant chord blade with arbitrary shape, the inviscid chord wise velocity is the same at all position r^*/R^* along the span locations. A real wind turbine blade shape does not have a constant chord, however, the method serves only as an approximation to the true 3D inviscid flow field.

2.5 Discretization and numerical integration

The system of equations (2.13)(2.14) with boundary conditions in section 2.3.5 represents a coupled set of non-linear third order partial differential equations. To be able to obtain a solution, it is required to express the equations as an equivalent first order system. This can be done by introducing new dependent variables as follows.

$$f' = u \tag{2.38}$$

$$u' = v = f'' \tag{2.39}$$

$$\begin{aligned} f''' = v' = -0.5fv - \xi f_\xi v - \frac{c^*}{r^*}\xi g v + \xi f'_\xi u - m\left(1 + 0.5fv - u^2\right) \\ -n\left(0.5v - uw\right) - \frac{c^*}{r^*} s_w \xi w \left(\frac{2RoP_{ro}}{U_{xf}} - u\right) \end{aligned} \tag{2.40}$$

$$g' = w \tag{2.41}$$

$$w' = t = g'' \tag{2.42}$$

$$\begin{aligned} g''' = t' = -0.5ft - \xi f_\xi t - \frac{c^*}{r^*}\xi g t + \xi g'_\xi u - m\left(0.5ft - uw\right) \\ -n\left(\frac{1}{U_{xf}} - 0.5gt - w^2\right) + \frac{c^*}{r^*}\xi u \left(\frac{2Ro}{U_{xf}} - u\right) \end{aligned} \tag{2.43}$$

After proceding with an evaluation of the effect of the variable θ on the solution of the set equations, it was found that does not affect the shape of

the resultant velocity profiles, therefore, the θ terms have been neglected in equations (2.38)-(2.43),

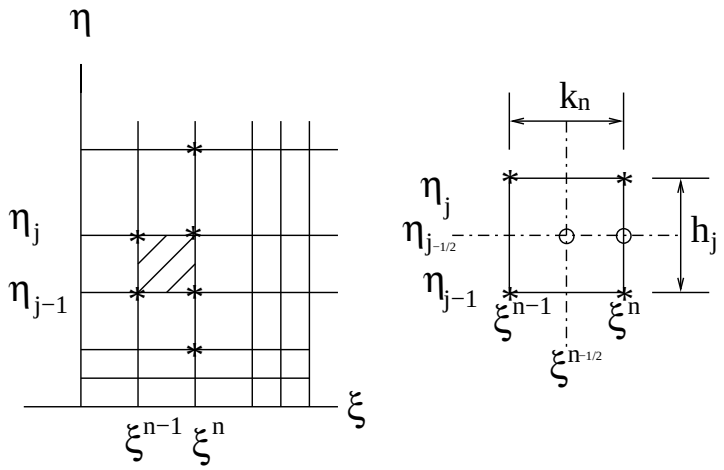

Figure 2.7: Discretization box

Taking as a reference the figure (2.7) the previous set of equations are discretized using centered-difference derivatives, n and j are only sequence numbers, not any particular indices or exponents, (the index n is not to be confused with the radial pressure gradient). reproduced from Cebeci and Bradshaw [14]. The following definitions are used to obtain the quantities midway on the net, for any variable y_j^n :

$$\xi^{n-1/2} \equiv \frac{1}{2}\left(\xi^n + \xi^{n-1}\right) \tag{2.44}$$

$$\eta_{j-1/2} \equiv \frac{1}{2}\left(\eta_j + \eta_{j-1}\right) \tag{2.45}$$

$$y_j^{n-1/2} \equiv \frac{1}{2}\left(y_j^n + y_j^{n-1}\right) \tag{2.46}$$

$$y_{j-1/2}^n \equiv \frac{1}{2}\left(y_j^n + y_{j-1}^n\right) \tag{2.47}$$

$$\frac{f_j^n - f_{j-1}^n}{h_j} = u_{j-1/2}^n \tag{2.48}$$

$$\frac{u_j^n - u_{j-1/2}^n}{h_j} = v_{j-1/2}^n \tag{2.49}$$

$$\begin{aligned}\frac{v_j^n - v_{j-1}^n}{h_j} = &-(fv)_{j-1/2}^n - \frac{c^*}{r^*}\xi^n (gv)_{j-1/2}^n \\ &-m^n \left[1 + 0.5(fv)_{j-1/2}^n - (u^2)_{j-1/2}^n\right] \\ &-n^n \left[0.5(f)_{j-1/2}^n - (uw)_{j-1/2}^n\right] \\ &-\frac{c^*}{r^*} s_w \xi^n (w)_{j-1/2}^n \left[\frac{2RoP_{ro}^n}{U_{xf}^n} - (u)_{j-1/2}^n\right] \\ &-\xi^{n-1/2} \frac{(f_{j-1/2}^n - f_{j-1/2}^{n-1})(v_{j-1/2}^n)}{K_n} \\ &+\xi^{n-1/2} \frac{(u_{j-1/2}^n - u_{j-1/2}^{n-1})(u_{j-1/2}^n)}{K_n}\end{aligned} \tag{2.50}$$

$$\frac{g_j^n - g_{j-1/2}^n}{h_j} = w_{j-1/2}^n \tag{2.51}$$

$$\frac{w_j^n - w_{j-1/2}^n}{h_j} = t_{j-1/2}^n \tag{2.52}$$

$$\begin{aligned}\frac{t_j^n - t_{j-1}^n}{h_j} = &-0.5(ft)_{j-1/2}^n - \frac{c^*}{r^*}\xi^n (gt)_{j-1/2}^n \\ &-m^n \left[0.5(ft)_{j-1/2}^n - (uw_{j-1/2}^n))\right] \\ &-n^n \left[\frac{1}{U_{xf}^n} - 0.5(gt)_{j-1/2}^n - (w^2)_{j-1/2}^n\right] \\ &-\frac{c^*}{r^*} s_w \xi^n (u)_{j-1/2}^n \left[\frac{2Ro}{U_{xf}^n} - (u)_{j-1/2}^n\right] \\ &-\xi^{n-1/2} \frac{(f_{j-1/2}^n - f_{j-1/2}^{n-1})(t_{j-1/2}^n)}{K_n} \\ &+\xi^{n-1/2} \frac{(w_{j-1/2}^n - w_{j-1/2}^{n-1})(u_{j-1/2}^n)}{K_n}\end{aligned} \tag{2.53}$$

The numerical technique used to solve the set of PDE system is a collocation method that uses the 3-stage Lobatto IIIa formula and the collocation polynomial provides a continuous solution that is fourth order accurate,

Kierzenka and Shampine [55]. The function bvp4c from MATLAB was used to solve the equations. The advantage of this approach is that is relatively easy to make changes in the formulation without the need of forming the matrices by hand. It is also found to be more stable that the classical shooting method by Keller [51], in a manner that can tolerate for wrong initial estimates. One of the restrictions of this approach is that, it takes relatively high amount of computing time in comparison with the Keller box method, which is 2nd order accurate, therefore can not be used for transition prediction.

2.6 Extension of the 2D Database to rotational effects

To extend the 2D Database that includes the (FS) velocity profiles (in the attached and separated region) for rotational effects, it is relevant to make an analysis of the boundary layer parameters and the relation among them. To begin the discussion the basic 2D solution of the Falkner-Skan equation is presented for the velocity profiles used on EllipSys3D code [108] on the attached flow region. The next figure show the variation of the boundary layer parameters according to the velocity profiles designated by cases.

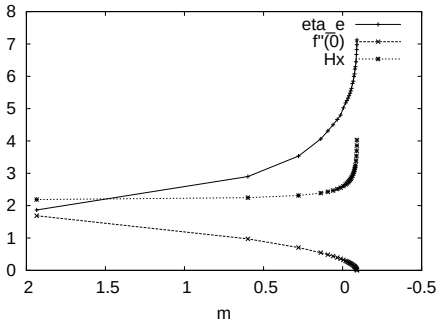

Figure 2.8: 2D boundary layer parameters

From the Figure (2.8) is shown that the shape factor H_x decreases when m increases and the edge value η_e in increasing, while, the skin friction coefficient $f''(0)$ decreases. From figure (2.9) the case 1 correspond to the higher pressure gradient m, as the pressure gradient decreases the case number increses, the minumum pressure gradient is found for case 27. One key information is that the shape of the velocity profile is uniquely defined if one of the previous parameters is given.

In Figure 2.9 it is shows the tangential velocity profile for the 2D Database. On the left part is shown the velocity profile, while in the right figure the

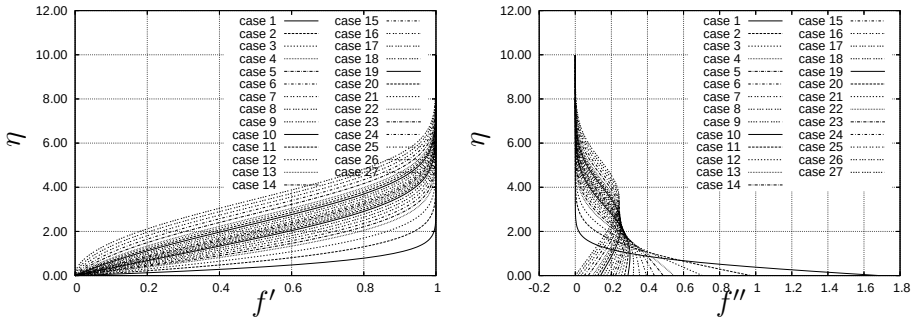

Figure 2.9: 2D boundary layer solution a)Velocity profile and b)Stress distribution

variation of the shear stress $f''(\eta)$ across the boundary layer.

From the Database three cases will be selected to evaluate the effect of rotation: 1) with a favorable pressure gradient, the classical example of the flow close to the stagnation point case 1, 2) a velocity profile with a pressure gradient close to 0 designated by case 8, 3) a velocity profile with an adverse pressure gradient, just before separation case 26. The numerical values of the boundary layers are visible on the next table.

Table 2.1: 2D Boundary layer Parameters

$Case$	η_e	m	$f''(0)$	δ_x	θ_x	H_x
1	1.867	1.9350	1.68790	0.48430	0.22140	2.189
8	4.800	.0126	.35653	1.65510	0.64740	2.558
26	6.975	-.0902	.01464	3.34456	0.86693	3.858

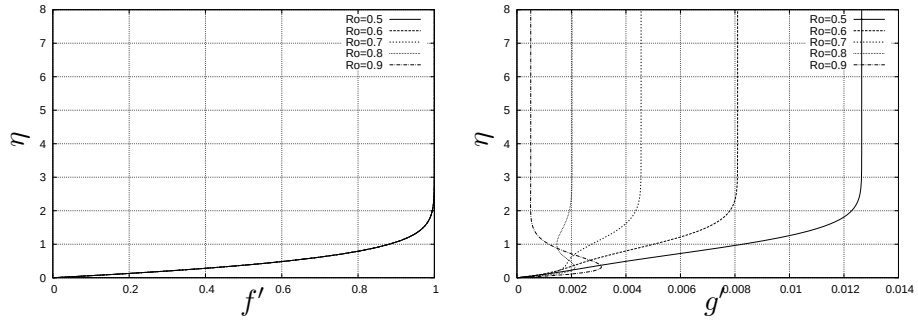

Figure 2.10: Velocity profiles for case 1 a) Tangential b) Radial

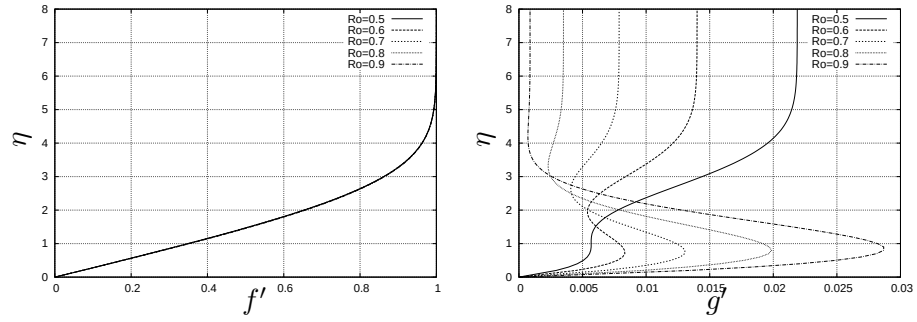

Figure 2.11: Velocity profiles for case 8 a) Tangential b) Radial

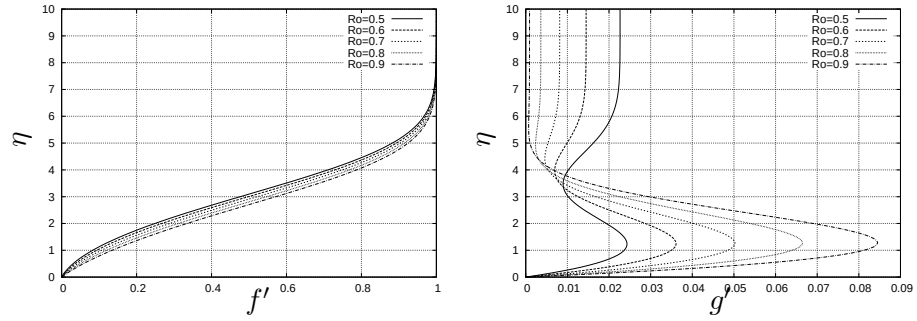

Figure 2.12: Velocity profiles for case 26 a) Tangential and b) Radial

Introducing rotational effect, figures (2.10),(2.11) and (2.12) reveal the shape of the crossflow and the respective tangential velocity at different rotation numbers ranging from 0.5 to 0.9 for the three different cases at a midway position $x^*/c^* = 0.5$, for a local solidity $c^*/r^* = 0.35$ close to the inboard location. The Database covers a set of simulations that cover the full range of parameters, is somehow difficult to show all the cases, we just take some representative example. From the plots it is clear that the maximum value g'_{max} occurs for the case 26 in the adverse pressure zone.

Looking at the shear stress distribution from figures (2.13) - (2.15) it is found that fixing the local rotation number Ro, as the value of c^*/r^* increases, the wall shear stress on the tangential direction also increases making the velocity profile more stable in this direction. For positive values of m corresponding to favorable pressure gradients, the effect of the rotation is not as high as on the region of negatives values of m. At the stagnation point the tangential flow is very stable, the magnitude of the cross flow is small , and before separation the rotational effects have strong stabilizing effect.

The relative importance of the Coriolis and Centrifugal forces on the

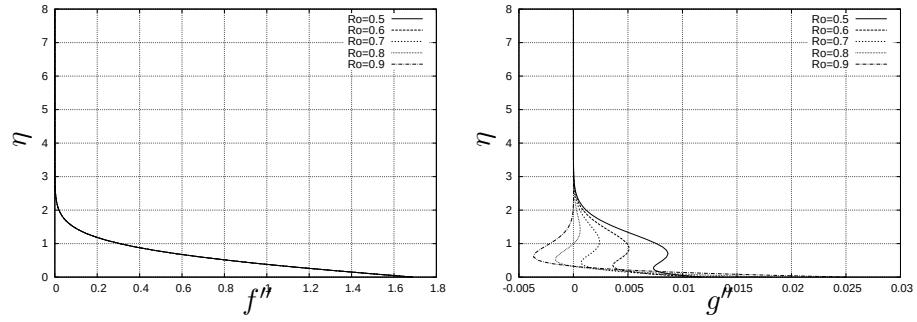

Figure 2.13: Stress distribution for case 1 a) Tangential b) Radial

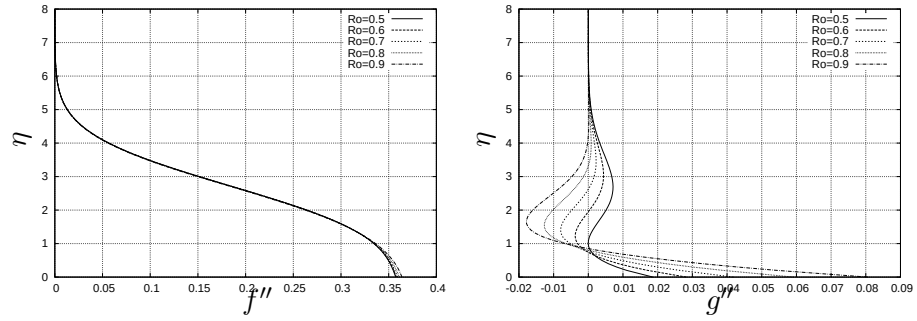

Figure 2.14: Stress distribution for case 8 a) Tangential b) Radial

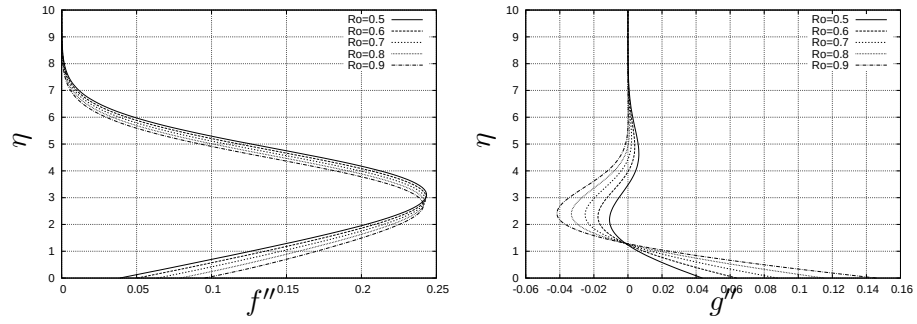

Figure 2.15: Stress distribution for case 26 a) Tangential b) Radial

boundary layer can be better understood by looking at the stress distributions in the figures (2.13), (2.14) and (2.15). The Coriolis force has no effect at the bottom of the boundary layer, as the η value is increasing this term produces a stronger force. The centrifugal force is all way long constant on the boundary layer and is directed toward the tip of the blade. It is

clear from figures (2.10)(2.11) and (2.12) that the stress distribution in the tangential direction is modified by the cross flow component.

The position of η_{cr} is set by the pressure gradient m and the local rotation number Ro, that for this case it is a higher value, in the favorable pressure gradient zone for cases 1 and 8, while the value of η_{cr} is lower than the one close to the separation.

For some combinations of parameters the cross flow can exhibit 2 inflection points, that make the flow very unstable in the radial direction. The same analysis has been performed at different positions on the span. The outcome from the analysis is that, by comparing different positions of the local solidity, the shape of the cross flow velocity profiles scale with an amount proportional to c^*/r^*. This is in agreement with the work done by Snel [99],[100] in the attached flow region. In a similar manner the computations made by Shen and Sørensen [101] that clearly showed the shape of the separation bubble, additional to the work of Chaviaropoulos and Hansen [24].

2.7 Rotating flat plate case

In this section computations along a rotating flat plate are presented. For this particular case m=0 , Ro=1 and $P_{ro} = 1$, and the stream lines are circular arcs and the value of $g'_e = 0$ according to figure (2.6). Fixing the rotation number implies that the position of the inflection point η_{cr} will be the same for different values of c^*/r^* and ξ. The height is located at $\eta_{cr} = 1$ (see figure (2.6)). The figures (2.17a) and(2.17b) reveal the increase of the wall shear stress for both velocity components . Plotting the wall shear stress of both velocity components (2.18a) and (2.18b) reveals that for all c^*/r^* values all the velocity profiles fit on that curve, this implies that the velocity profile shape is uniquely defined by specifying the dimensionless pressure gradient m, the rotation number Ro and the wall shear stress ratio. Is also possible to use another parameters instead of the wall shear stress ratio to define the shape. For example it is possible to set the value g'_{max}, the dimensionless pressure gradient n, or the radial shape factor $H_{r\theta}$. This can be seen in table (2.2) that accounts for the tangential direction and table (2.3) for the radial direction where one single family is defined from rows 2 and 4, another example from rows 3 and 7 and finally rows 6 and 8 . The key point is to understand that the shape of the cross flow velocity profile is set by the rotation number in combination with the tangential pressure gradient m. The same analysis can be generalized to different pressure gradient according to the cases shown on section 2.6. In the adverse pressure gradient zone a small deviation is observed since the profiles does not exactly fit on one single curve when the skin friction relation is plotted, as seen in figure (2.19b), Another interesting observation is that the shape

factors relation, is seen to be linear in figure (2.18a), however can not be a parameter to describe a velocity profile family as seen in figure (2.19a).

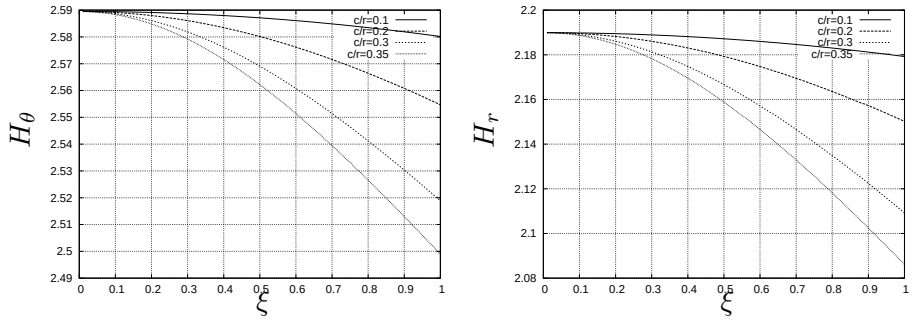

Figure 2.16: Variation of Shape factor a)Tangential b)radial

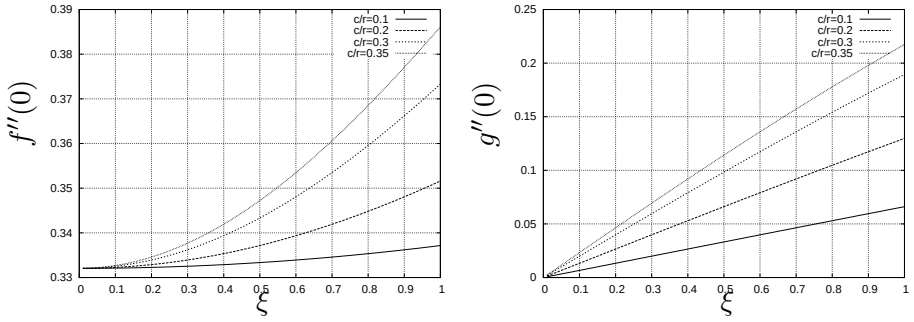

Figure 2.17: Variation of skin friction coefficient a)Tangential and b)radial

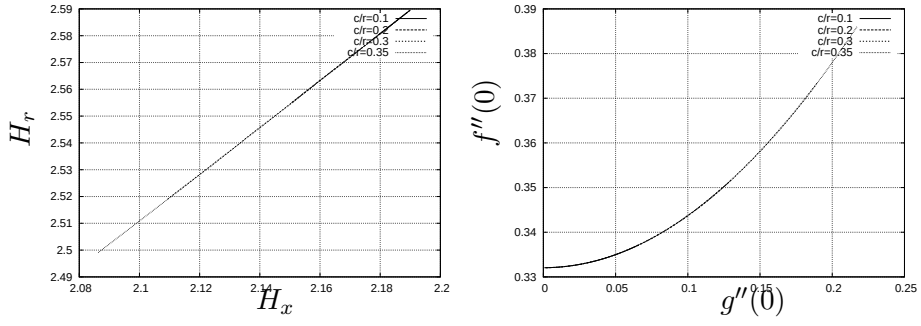

Figure 2.18: a) Shape factors relation and b)Wall skin friction relation for rotating flat plate

Performing a comparison of the solution of the equations (2.13), (2.14)

according to the parameters defined on section section (2.3.1), plotting the velocity profiles and the corresponding boundary layers properties, the following conclusions are obtained: From the parametrical study the shape of the cross flow velocity profile is uniquely defined if the value of m together with the Rotation number Ro are specified. It follows that the shape will scale according to the position on the blade ξ and with the local solidity c^*/r^* as shown. The position of the inflection point or points on the cross flow is set by these two parameters. The tendency is that decreasing the value of m increases the height of the inflection point as seen by comparing the cases for separation and for the rotating flat plate. This can be seen on the dimensionless radial pressure gradient $n = \xi Ro^2 c^*/r^*$. To explain the phenomenon, it is possible to look more closely to the terms on the transformed equations (2.13)(2.14): The Centrifugal force will always push the flow out from the blade root, and the Coriolis force on the radial direction will act agains, the resulting shape is a balance between the two forces and the pressure gradient m.

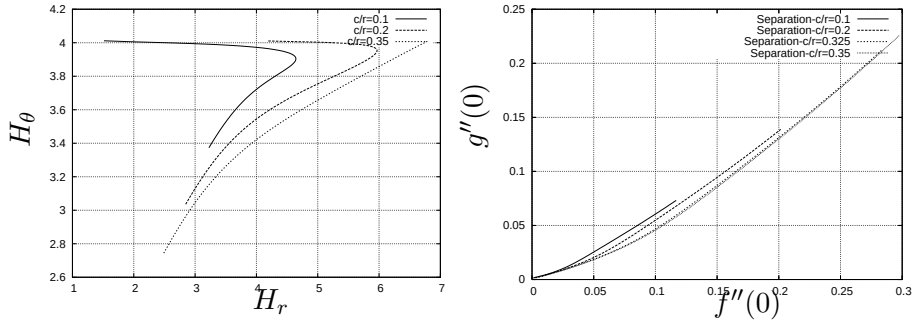

Figure 2.19: a) Shape factors relation b)Wall skin friction relation for separation

2.8 Summary

In this chapter the solution of the laminar boundary layer equations on a rotating wind turbine blade was presented. The parameters needed to describe the flow on the rotating configuration were established and the relation with the boundary layer properties was investigated. The original formulation from Dumitrescu and Cardos [29] was studied , parametrized and adapted to a real airfoil configuration. Finally the boundary condition was modified to obtain a smooth solution close to the edge of the boundary layer. All velocity profiles were mapped and stored in a Database that in the subsequent chapters will be used as a base flow for the transition prediction.

Table 2.2: Boundary layer properties for the rotating flate plate I

row	$H_{\theta\theta}$	$f''(0)$	$n(-)$	$c^*/r^*(-)$	δ_θ	$\theta_{\theta\theta}$
2D	2.591	0.33206	0	0	1.7207	0.66412
1	2.589	0.33238	0.0250	0.10	1.7204	0.66453
2	2.587	0.33335	0.0500	0.10	1.7181	0.66410
3	2.584	0.33494	0.0750	0.10	1.7143	0.66339
4	2.587	0.33335	0.0500	0.20	1.7181	0.66410
5	2.580	0.33717	0.1000	0.20	1.7090	0.66240
6	2.569	0.34333	0.1500	0.20	1.6947	0.65964
7	2.584	0.33496	0.0750	0.30	1.7143	0.66338
8	2.569	0.34334	0.1500	0.30	1.6946	0.65963
9	2.546	0.35646	0.0225	0.30	1.6646	0.65370
10	2.582	0.33600	0.0875	0.35	1.7118	0.66292
11	2.562	0.34724	0.1750	0.35	1.6856	0.65787
12	2.533	0.36449	0.2625	0.35	1.6465	0.65000

Table 2.3: Boundary layer properties for the rotating flate plate II

row	$H_{r\theta}$	$g''(0)$	$n(-)$	$c^*/r^*(-)$	g'_{max}	δ_r	$\theta_{r\theta}$
1	2.189	0.01662	0.0250	0.10	0.00691	-1.4270e-02	-6.5183e-03
2	2.187	0.03320	0.0500	0.10	0.01380	-2.8462e-02	-1.3013e-02
3	2.184	0.04971	0.0750	0.10	0.02060	-4.2501e-02	-1.9462e-02
4	2.187	0.03320	0.0500	0.20	0.01380	-2.8458e-02	-1.3011e-02
5	2.179	0.06609	0.1000	0.20	0.02730	-5.6311e-02	-2.5839e-02
6	2.167	0.09836	0.1500	0.20	0.04040	-8.3025e-02	-3.8320e-02
7	2.184	0.04970	0.0750	0.30	0.02060	-4.2495e-02	-1.9457e-02
8	2.167	0.09835	0.1500	0.30	0.04040	-8.3009e-02	-3.8311e-02
9	2.141	0.14509	0.0225	0.30	0.05890	-1.2006e-01	-5.6084e-02
10	2.182	0.05791	0.0875	0.35	0.02390	-4.9427e-02	-2.2654e-02
11	2.159	0.11417	0.1750	0.35	0.04670	-9.5785e-02	-4.4369e-02
12	2.126	0.16756	0.2625	0.35	0.06740	-1.3701e-01	-6.4455e-02

Chapter 3

Stability solution for Parallel flows

The present Chapter focuses on the formulation of the linear stability equations on external viscous flows. The foundation, limitations and use of the e^n method are presented. In a similar manner, is presented, the formulation of the database that cover velocity profiles with positive and adverse pressure gradients. The study and parametrization of the numerical solution and Database formulation will provide valuable information for the extension with rotational effects in the next chapters.

3.1 Introduction

The linear stability theory developed by Tollmien (1929) and Schlichting (1933) describes the growth of perturbations up to the point where nonlinear interactions and higher order instabilities become evident. However, this linear part represents a notable part of the transition process. The existence of the Tollmien-Schlichting (TS) waves was recognized in the experiments of Schubauer and Skramstad [96], the agreement with the theoretical curve is remarkably good. Before the success of this experiments some attempts in high turbulence level tunnels were accomplished. However, it was not possible to observe clearly the transition process due to the influence of the high turbulence intensity. Actually turbulence levels below 0.1% can be achieved in modern wind tunnels. Pretsch [83] extended the previous results for adverse and favorable pressure gradients. Some years later Wazzan et al. [112] improved and extended the calculations for different pressure gradients with both temporal and spatial approaches, and a more robust numerical method. The critical Reynolds number was accurately calculated. It is very important to mention that the stability or frequency diagrams indicate the response of the boundary layer to the external disturbances (whatever they are or came from), however it does not indicate the transition location. It

was some years later that Smith & Gamberoni (1956) and Van Ingen (1956), partially motivated by the results obtained by Schubauer and Skramstad, independently developed the e^n method. The values assigned were different, Smith assigned a value of 9, while Van Ingen noticed that was in fact a process to set the value of $n = 7.8$ at the begging and $n = 10$ at the end. By careful examination of the amplification of frequencies in the unstable area of the frequency diagrams that correspond to some given pressure distribution on an EC 1440 airfoil , where by varying the angle of attack on a moderate range and the operational conditions of the tunnel, that transition from laminar to turbulent flow was taking place when the N-factor reached some predefined value. This was achieved by following a constant dimensional frequency on the stability diagram that represents the response of the boundary layer. Clearly the waves were amplified in a different manner due to the fact that they follow different paths in the stability diagrams. In his PhD dissertation Van Ingen [46] extract the information from the stability diagrams of Prestch and converted into a digital formal suited for fast calculations. The first Database ever made can be attributed to Van Ingen or Smith & Gamberoni. They found the procedure to interpolate among different stability diagrams that correspond to different pressure gradients along the surface of an airfoil.

3.2 Formulation of linear Stability equations of external paralel flows

The stability theory is mainly concerned with individual sine waves propagating in the boundary layer parallel to the surface. These waves are commonly referred as Tollmien-Schlichting waves, or (TS) waves. The amplitude of these waves, which vary through the boundary layer and dies off exponentially in the free stream, are small enough so that linear stability theory may be used. The formulation of the stability equations is based on the parallel flow assumption, requiring that the mean flow velocity components are function of the normal coordinate only, and the derivatives with respect to the other directions are not taken into consideration.

$$\frac{\partial \mathbf{V}}{\partial t} + \mathbf{V}\nabla\mathbf{V} = -\frac{\nabla P}{\rho} + \nu\Delta\mathbf{V} \tag{3.1}$$

$$\Delta\mathbf{V} = 0 \tag{3.2}$$

The standard procedure to derive stability equations is to introduce disturbances or small deviations from the equilibrium position in the velocity components and pressure (U', V', W'), P' of (NS) (3.1) and (3.2), and subtracting the base flow from the perturbed equations. In the derivation, it is assumed that both the undisturbed and the disturbed flow satisfy the (NS)

equations. The purpose of the present study is to compute how the flow response to the external disturbances. If the boundary layer is consider as a complicated oscillator, the response to external forcing is to be investigated.

Assuming small disturbance to behave like sinusoidal traveling plane waves.

$$U' = U(z)e^{i(\alpha x+\beta y-\omega t)} \tag{3.3}$$
$$V' = V(z)e^{i(\alpha x+\beta y-\omega t)} \tag{3.4}$$
$$W' = W(z)e^{i(\alpha x+\beta y-\omega t)} \tag{3.5}$$
$$P' = P(z)e^{i(\alpha x+\beta y-\omega t)} \tag{3.6}$$

The complex amplitude function in equations (3.3)-(3.6) depends only on z. In the expression α represents the wave number in the x or streamwise direction, β accounts for the wave vector in the y or spanwise direction and ω is the frequency. Introducing this representations in the linearized NS or in a similar manner taking the Fourier transform in the horizontal directions the following set of equations is obtained.

$$i(\alpha U + \beta V - \omega)U' + DUW' = -i\alpha P' + \frac{1}{R}[D^2 - (\alpha^2 + \beta^2)]U' \tag{3.7}$$
$$i(\alpha U + \beta V - \omega)W' = -DP' + \frac{1}{R}[D^2 - (\alpha^2 + \beta^2)]W' \tag{3.8}$$
$$i(\alpha U + \beta V - \omega)V' + DVW' = -i\beta P' + \frac{1}{R}[D^2 - (\alpha^2 + \beta^2)]V' \tag{3.9}$$
$$i\alpha U' + i\beta V' + DW' = 0 \tag{3.10}$$

The previous equations constitute a linear system of equations for the variables U',V',W',P',DU',DV', and can be manipulated further for the determination of the eigenvalues. Multiplying equation (3.7) by α and (3.9) by β the result is equation (3.11). In a similar way (for convenience) the equation (3.13) is obtained by eliminating the pressure from (3.7) and (3.9) leading to four variables $\alpha U' + \beta V'$,W',$\alpha V' - \beta U'$ and P'. It is clear that equation (3.11) is the momentum equation in the direction parallel to the wave vector $k = \sqrt{\alpha^2 + \beta^2}$, and the vorticity equation (3.13) is the momentum equation in the direction normal to k, in the x,y plane.

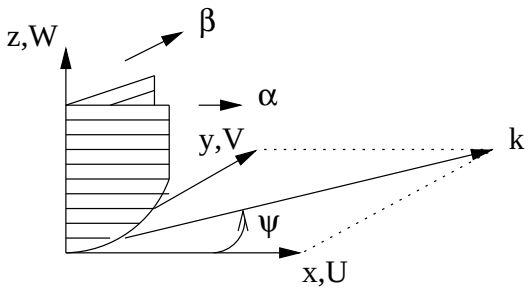

Figure 3.1: Reference system for stability computations on cartesian coordinates

$$i(\alpha U + \beta V - \omega)(\alpha U' + \beta V') + (\alpha DU + \beta DV)W' = \\ -i(\alpha^2 + \beta^2)P' + \frac{1}{R}[D^2 - (\alpha^2 + \beta^2)](\alpha U' + \beta V') \tag{3.11}$$

$$i(\alpha U + \beta V - \omega)W' = -DP' + \frac{1}{R}[D^2 - (\alpha^2 + \beta^2)]W' \tag{3.12}$$

$$i(\alpha U + \beta V - \omega)(\alpha V' - \beta U') + (\alpha DV - \beta DU)W' = \\ \frac{1}{R}[D^2 - (\alpha^2 + \beta^2)](\alpha V' - \beta U') \tag{3.13}$$

$$i(\alpha U' + \beta V') + DW' = 0 \tag{3.14}$$

The numerical solution of the system of equations requires that the equations are written as an equivalent first order system. Defining the new variables (3.15)-(3.20):

$$Z_1 = \alpha U' + \beta V' \tag{3.15}$$

$$Z_2 = \alpha DU' + \beta DV' \tag{3.16}$$

$$Z_3 = W' \tag{3.17}$$

$$Z_4 = P' \tag{3.18}$$

$$Z_5 = \alpha V' - \beta U' \tag{3.19}$$

$$Z_6 = \alpha DV' - \beta DU' \tag{3.20}$$

and manipulating the previous equations and complex variables C_1 to C_9, the equivalent linear system is obtained (3.21)-(3.26)

$$
\begin{aligned}
DZ_1 &= Z_2 && (3.21)\\
DZ_2 &= C_1Z_1 + C_2Z_3 + C_4Z_4 && (3.22)\\
DZ_3 &= -C_5Z_1 && (3.23)\\
DZ_4 &= -C_6Z_2 - C_7Z_3 && (3.24)\\
DZ_5 &= Z_6 && (3.25)\\
DZ_6 &= C_8Z_3 + C_9Z_5 && (3.26)
\end{aligned}
$$

Equation (3.23) is simply the continuity equation, equation (3.24) is the velocity for the fluctuating normal velocity W' that came from (3.12), equations (3.22) and (3.25) have been previously defined with (3.11) and (3.13), the rest of the equations are definitions as can be seen on the group of variables on (3.15)-(3.20).

3.3 Orr-Sommerfeld equation

The Orr-Sommerfeld equation is a special case of the system (3.21-3.26), and can be obtained from expressions (3.7), (3.8) and (3.11), assuming that the disturbance is aligned with the x direction. For this purpose β is set to zero. By setting this value, the effect of the velocity component in the y direction is canceled. To express the resulting system as a single equation, the stream function is expanded into Fourier modes $\psi = \phi(z)exp[i(\alpha x - \omega t)]$. $U' = D\phi$ and $W' = -i\alpha\phi$. Introducing the relations into equations (3.7) and (3.8), (the continuity equation is automaticaly satisfied), eliminating the pressure and differentiating by the normal coordinate the solution is the following 4th order ODE. Detailed explanation on the equation can be found in Aref [4] and Mack [65].

$$[D^2 - (\alpha^2)]^2\phi' = i\alpha R\left[(\alpha U - \omega)[D^2 - (\alpha^2)] - (\alpha D^2 U)\right]\phi' \qquad (3.27)$$

In order to obtain a numerical solution it is required that the the equation is expressed as an equivalent first order system and is already written as equations (3.21)-(3.24). The solution of the O-S equation is the basis for most of the work that have been done in incompressible stability theory.

$$
\begin{aligned}
C_1 &= (\alpha^2+\beta^2)+iRe(\alpha U+\beta V-\omega) && (3.28)\\
C_2 &= R(\alpha DU+\beta DV) && (3.29)\\
C_4 &= iR(\alpha^2+\beta^2) && (3.30)\\
C_5 &= i && (3.31)\\
C_6 &= i/R && (3.32)\\
C_7 &= i(\alpha U+\beta V-\omega)+(\alpha^2+\beta^2)/Re) && (3.33)\\
C_8 &= R(\alpha DV-\beta DU) && (3.34)\\
C_9 &= \alpha^2+\beta^2+iRe(\alpha f'+\beta g'-\omega) && (3.35)
\end{aligned}
$$

The boundary conditions for the equivalent system are written in a way that the fluctuation in velocities U',V' and W' are damped at the wall or surface and tend to zero as the normal coordinate z tend to higher values where the viscosity of the flow has no effect on the amplification of the disturbances. It is important to notice that the fluctuation of the pressure P' is not damped on the bounding surface of the flow.

$$
\begin{aligned}
Z_1(0)=0, Z_3(0)=0, Z_5(0)=0 && (3.36)\\
Z_1(z)\to 0, Z_3(z)\to 0, Z_5(z)\to 0..as..z\to\infty && (3.37)
\end{aligned}
$$

The linear system can be written as $Z'=AZ$, where $Z=(Z_1,Z_2,Z_3,Z_4,Z_5,Z_6)^T$, the coefficients of the matrix A came from the derivation of the equations.

$$
A=\begin{pmatrix}
0 & 1 & 0 & 0 & 0 & 0\\
C_1 & 0 & C_2 & C_4 & 0 & 0\\
-C_5 & 0 & 0 & 0 & 0 & 0\\
0 & -C_6 & -C_7 & 0 & 0 & 0\\
0 & 0 & 0 & 0 & 0 & 1\\
0 & 0 & C_8 & 0 & C_9 & 0
\end{pmatrix} \qquad (3.38)
$$

3.4 Numerical solution

From the available methods used to solve the stability equations the finite difference (FD) offers the advantage of being not expensive in terms of computing time for relatively small size systems, similar to the one required for linear stability calculations. The Keller Box scheme is a well known and stable method, which has the advantage that it can be adapted to include more detail about the flow, like for example heat transfer effect, compressibility or separation. A full description and comparison of the available methods are given by Mack [65].

3.4.1 Keller Box Scheme

The Keller box scheme requires that the system of equations are written as an equivalent first order system. From the resulting first order equations on a non-uniform mesh, simple centered-difference derivatives and average at midpoint are used. To be able to make use of the Newton method, a block-tridiagonal factorization scheme is required. It can be shown that the systems of equations (3.21)-(3.26) has a tridiagonal structure and can be expressed in matrix-vector form as:

$$A\vec{\vec{\delta}} = \vec{\vec{r}} \tag{3.39}$$

Where:

$$A = \begin{pmatrix} A_0 & C_0 & & & & & \\ B_1 & A_1 & C_1 & & & & \\ & . & . & . & & & \\ & & . & . & . & & \\ & & B_j & A_j & C_j & & \\ & & & . & . & . & \\ & & & B_{J-1} & A_{J-1} & C_{J-1} & \\ & & & & B_J & A_J & \end{pmatrix}, \vec{\vec{\delta}} = \begin{pmatrix} \vec{\delta_0} \\ \vec{\delta_1} \\ . \\ . \\ \vec{\delta_j} \\ . \\ . \\ \vec{\delta_J} \end{pmatrix}, \vec{\vec{r}} = \begin{pmatrix} \vec{r_0} \\ \vec{r_1} \\ . \\ . \\ \vec{r_j} \\ . \\ . \\ \vec{r_J} \end{pmatrix}$$

$$\vec{\delta} = \begin{pmatrix} \delta Z_{1_j} \\ \delta Z_{2_j} \\ \delta Z_{3_j} \\ \delta Z_{4_j} \\ \delta Z_{5_j} \\ \delta Z_{6_j} \end{pmatrix}, \vec{r} = \begin{pmatrix} (r_1)_j \\ (r_2)_j \\ (r_3)_j \\ (r_4)_j \\ (r_5)_j \\ (r_6)_j \end{pmatrix}$$

The first rows of A_0 and C_0 matrices correspond to the wall boundary conditions, while the last rows of B_J and A_J matrices correspond to the edge boundary conditions. How the boundary conditions are distributed on the matrices depends on the particular problem. In the case of the linear stability equations, the first three rows correspond to the wall boundary condition, while the last three row to the edge side according to (3.36) and (3.37).

To be able to solve (3.39) the block elimination method is used, this requires a factorization of the form:

$$[B_j, A_j, C_j] = LU \tag{3.40}$$

$$L = [\Gamma_j, \Psi, 0] \tag{3.41}$$

$$U = [0, \Delta_j, \Gamma_j] \tag{3.42}$$

where L refers to the block-lower triangular matrix and U for the block-upper matrix. The factorization is not uniquely determined by the previous relations, therefore, is required to define the following expressions:

$$\Psi_j = I \tag{3.43}$$
$$\Gamma_j = C_j \tag{3.44}$$

Where I is the identity matrix and is equal to the size ot the linear system, for this particular formulation is 6x6. By inspection of the equations (3.40) - (3.42) the following recursion formulas are obtained:

$$\Delta_0 = A_0 \tag{3.45}$$
$$\Gamma_j \Delta_{j-1} = B_j \quad j = 1, 2, ..., J \tag{3.46}$$
$$\Delta_j = A_j - \Gamma_j C_j \quad j = 1, 2, ..., J \tag{3.47}$$

Where:

$$\Gamma_j = \begin{pmatrix} \gamma_{11_j} & \gamma_{12_j} & \gamma_{13_j} & \gamma_{14_j} & \gamma_{15_j} & \gamma_{16_j} \\ \gamma_{21_j} & \gamma_{22_j} & \gamma_{23_j} & \gamma_{24_j} & \gamma_{25_j} & \gamma_{26_j} \\ \gamma_{31_j} & \gamma_{32_j} & \gamma_{33_j} & \gamma_{34_j} & \gamma_{35_j} & \gamma_{36_j} \\ 0 & 0 & 0 & 0 & 0 & 0 \\ 0 & 0 & 0 & 0 & 0 & 0 \\ 0 & 0 & 0 & 0 & 0 & 0 \end{pmatrix} \tag{3.48}$$

$$\Delta_j = \begin{pmatrix} \alpha_{11_j} & \alpha_{12_j} & \alpha_{13_j} & \alpha_{14_j} & \alpha_{15_j} & \alpha_{16_j} \\ \alpha_{21_j} & \alpha_{22_j} & \alpha_{23_j} & \alpha_{24_j} & \alpha_{25_j} & \alpha_{26_j} \\ \alpha_{31_j} & \alpha_{32_j} & \alpha_{33_j} & \alpha_{34_j} & \alpha_{35_j} & \alpha_{36_j} \\ -1 & C_{3_j} & 0 & 0 & 0 & 0 \\ 0 & -C_{6_j} & -C_{7_j} & -1 & 0 & 0 \\ 0 & 0 & C_{8_j} & 0 & C_{9_j} & -1 \end{pmatrix} \tag{3.49}$$

Δ_j given on the range $0 \leq j \leq J-1$

Keller [51] shows that the Γ_j matrix has the same structure as the B_j matrix. In a similar manner the last three rows of Δ_j matrix are the same as the last three rows of A_j matrix according to equation (3.47). The elements of the Δ_j matrix are calculated from equation (3.47), using the definitions of A_j,Δ_j and C_{j-1}. To obtain the elements of the Γ_j matrix we make use of (3.46) with (3.49) and B_j. To fill up the Γ_j and Δ_j matrices the elements α_{ik} are obtained, first, by involving the wall boundary conditions (3.45), and

next, the elements γ_{ik}, then for the next mesh point $j = 1$ and subsequently. One observation is that to calculate the elements α_{ik} and γ_{ik}, it is needed to expand the linear systems of equations and manipulate the equation in such a way that the parameters are factorized. In other words, it is needed to solve an equivalent linear system for each one of the boundary conditions, a similar procedure will be required for the other diagonal matrix.
For the block-lower triangular matrix L from equation (3.41) is possible to write the following equation:

$$\begin{pmatrix} I & & & & & \\ \Gamma_1 & I & & & & \\ & \cdot & \cdot & & & \\ & & \cdot & \cdot & & \\ & & \Gamma_j & I & & \\ & & & \cdot & \cdot & \\ & & & \Gamma_{J-1} & I & \\ & & & & \Gamma_J & I \end{pmatrix} \begin{pmatrix} W_0 \\ W_1 \\ \cdot \\ \cdot \\ W_j \\ \cdot \\ W_{J-1} \\ W_J \end{pmatrix} = \begin{pmatrix} r_0 \\ r_1 \\ \cdot \\ \cdot \\ r_j \\ \cdot \\ r_{J-1} \\ r_J \end{pmatrix}$$

By inspection of the previous system we have:

$$W_0 = r_0 \tag{3.50}$$
$$W_j = r_j - \Gamma_j W_{j-1} \tag{3.51}$$

and the components of the vector W_j

$$W_j = \begin{pmatrix} W_{1_j} \\ W_{2_j} \\ W_{3_j} \\ W_{4_j} \\ W_{5_j} \\ W_{6_j} \end{pmatrix} \tag{3.52}$$

If follow from (3.50) that:

$$(W_1)_0 = (r_1)_0 \quad (W_2)_0 = (r_2)_0 \quad (W_3)_0 = (r_3)_0$$
$$(W_4)_0 = (r_4)_0 \quad (W_5)_0 = (r_5)_0 \quad (W_6)_0 = (r_6)_0$$

For the case of the block-upper matrix U defined on equation (3.42), the following system is written:

$$\begin{pmatrix} \Delta_0 & C_0 & & & & \\ & \Delta_1 & C_1 & & & \\ & \cdot & \cdot & \cdot & & \\ & & \cdot & \cdot & \cdot & \\ & & & \Delta_j & C_j & \\ & & & \cdot & \cdot & \cdot \\ & & & & \Delta_{J-1} & C_{J-1} \\ & & & & & \Delta_J \end{pmatrix} \begin{pmatrix} \delta_0 \\ \delta_1 \\ \cdot \\ \cdot \\ \delta_j \\ \cdot \\ \delta_{J-1} \\ \delta_J \end{pmatrix} = \begin{pmatrix} W_0 \\ W_1 \\ \cdot \\ \cdot \\ W_j \\ \cdot \\ W_{J-1} \\ W_J \end{pmatrix}$$

By inspection the previous system the next equations are found:

$$\Delta_J \delta_J = W_J \tag{3.53}$$

$$\Delta_j \delta_j = W_j - C_j \delta j + 1 \quad j = J-1, J-2, ..., 0 \tag{3.54}$$

The elements of the unknown vectors, δ_j are calculated from (3.53) and (3.54) introducing the definitions of Δ_j, W_j, C_j.

Two main loops are required in the block elimination method: in the forward loop the information from the wall boundary condition is propagating through the non-uniform mesh until it hits the edge limit where the top boundary conditions are applied. This is made by first calculating the right hand side vectors $\vec{r}$ from (3.39). The matrix elements A_j,B_j,C_j are found from the complex variables (3.28)-(3.35). Using the recursion formulas from (3.45)-(3.47) and (3.50)-(3.51) the matrices Γ_j,Δ_j and vectors W_j are fill up. The backward swept is found when the solution travels back from the top boundary conditions through the non-uniform mesh, this formally follows the calculation of the elements of the vectors $\vec{r}$ from the recursion formulas (3.53) and (3.54).

3.4.2 Discretization of the 6x6 system of equations

To formulate the numerical scheme of the 6x6 system, using equations (3.21-3.26), we write the finite difference approximations at the midpoints of the cell in the normal direction, using central-difference derivatives on a non uniform mesh.

$$\frac{Z_{1(j)} - Z_{1(j-1)}}{h_{(j-1)}/2} = (Z_{2(j)} + Z_{2(j-1)}) \quad (3.55)$$

$$\frac{Z_{2(j)} - Z_{2(j-1)}}{h_{(j-1)}/2} = C_{1(j)}(Z_{1(j)} + Z_{1(j-1)}) + C_{2(j)}(Z_{3(j)} + Z_{3(j-1)}) + C_{4(j)}(Z_{4(j)} + Z_{4(j-1)}) \quad (3.56)$$

$$\frac{Z_{3(j)} - Z_{3(j-1)}}{h_{(j-1)}/2} = -C_{5(j)} \quad (3.57)$$

$$\frac{Z_{4(j)} - Z_{4(j-1)}}{h_{(j-1)}/2} = -C_{6(j)}(Z_{2(j)} + Z_{2(j-1)}) - C_{7(j)}(Z_{3(j)} + Z_{3(j-1)}) \quad (3.58)$$

$$\frac{Z_{5(j)} - Z_{5(j-1)}}{h_{(j-1)}/2} = (Z_{6(j)} + Z_{6(j-1)}) \quad (3.59)$$

$$\frac{Z_{6(j)} - Z_{6(j-1)}}{h_{(j-1)}/2} = C_{8(j)}(Z_{3(j)} + Z_{3(j-1)}) + C_{9(j)}(Z_{5(j)} + Z_{5(j-1)}) \quad (3.60)$$

The system of equations can be written as an equivalent three diagonal matrix as follows:

$$A_j = \begin{pmatrix} -C_1 & 1 & -C_{2j} & -C_{4j} & 0 & 0 \\ C_{5j} & 0 & 1 & 0 & 0 & 0 \\ 0 & 0 & 0 & 0 & 1 & -C_{3j} \\ 1 & C_{3j+1} & 0 & 0 & 0 & 0 \\ 0 & -C_{6j+1} & -C_{7j+1} & 1 & 0 & 0 \\ 0 & 0 & C_{8j+1} & 0 & C_{9j+1} & 1 \end{pmatrix}$$

$$B_j = \begin{pmatrix} -C_{1j} & -1 & -C_{2j} & -C_{4j} & 0 & 0 \\ C_{5j} & 0 & -1 & 0 & 0 & 0 \\ 0 & 0 & 0 & 0 & -1 & -C_{3j} \\ 0 & 0 & 0 & 0 & 0 & 0 \\ 0 & 0 & 0 & 0 & 0 & 0 \\ 0 & 0 & 0 & 0 & 0 & 0 \end{pmatrix}$$

$$C_j = \begin{pmatrix} 0 & 0 & 0 & 0 & 0 & 0 \\ 0 & 0 & 0 & 0 & 0 & 0 \\ 0 & 0 & 0 & 0 & 0 & 0 \\ -1 & C_{3j+1} & 0 & 0 & 0 & 0 \\ 0 & -C_{6j+1} & -C_{7j+1} & -1 & 0 & 0 \\ 0 & 0 & C_{8j+1} & 0 & C_{9j+1} & -1 \end{pmatrix}$$

With Boundary conditions at the wall:

$$A_0 = \begin{pmatrix} 0 & 1 & 0 & 0 & 0 & 0 \\ 0 & 0 & 1 & 0 & 0 & 0 \\ 0 & 0 & 0 & 0 & 1 & 0 \\ 1 & C_{3_1} & 0 & 0 & 0 & 0 \\ 0 & -C_{6_1} & -C_{7_1} & 1 & 0 & 0 \\ 0 & 0 & C_{8_1} & 0 & C_{9_1} & 0 \end{pmatrix} \tag{3.61}$$

at the edge:

$$A_J = \begin{pmatrix} -C_{1_J} & 1 & -C_{2_J} & -C_{4_J} & 0 & 0 \\ C_{5_J} & 0 & 1 & 0 & 0 & 0 \\ 0 & 0 & 0 & 0 & 1 & -C_{3_J} \\ 1 & 0 & 0 & 0 & 0 & 0 \\ 0 & 0 & 1 & 0 & 0 & 0 \\ 0 & 0 & 0 & 0 & 1 & 0 \end{pmatrix} \tag{3.62}$$

3.4.3 Eigenvalue problem and Newton Method

The solution of the system of equations (3.21)-(3.26) constitute an eigenvalue problem leading to the dispersion relation between the wave numbers α,β, the frequency ω and the Reynolds number R. Due to the nature of the boundary conditions (3.36) and (3.37) , the trivial solution exists for all eigenvalues, therefore, it is required to break this homogeneous condition. This is done by replacing one of the boundary conditions, and later by the use of the Newton method, adjust it to determine the solution of the dispersion relation, in a way that the original boundary condition is safisfied. The solution of the characteristic equation (3.63) may be obtained by temporal or spatial theories. In the first case the dimensionless frequency ω is complex, and the wave vectors are real, the amplitude of the disturbance varies on time. On the spatial approach, the wave numbers α and β are complex and the frequency ω real in a way that the amplitude of the disturbance varies with distance. In the case that the disturbance varies with time and distance, the wave numbers and the frequency are complex.

The Newton method is used to adjust increments on the chosen eigenvalues from the characteristic equation:

$$f(\alpha_r, \alpha_i, \beta_r, \beta_i, \omega_r, \omega_i, R) = 0 \tag{3.63}$$

If the initial estimate is with in the convergence radious the method will provide quadratic convergence towards the desired solution. In the case of 2D flow the characteristic equation is simplified as:

$$f(\alpha_r, \alpha_i, \omega_r, \omega_i, R) = 0 \tag{3.64}$$

The technique to navigate or move on the multidimensional space or planes is to fix some of the eigenvalues while calculating increments in the desired planes. In the case of spatial theory the frequency ω is real, that is $\omega_i = 0$, and the wave vector α is complex. For example, to obtain the neutral response or neutral curve $\alpha_i = 0$, the Reynolds number R is modified manually according to the defined mesh density. Expanding equation (3.64) around α_r^ν and ω_r^ν by Taylor series, and retaining only linear terms the following linear system is obtained:

$$f_r^\nu + \left(\frac{\partial f_r}{\partial \alpha_r}\right)^\nu \delta\alpha_r^\nu + \left(\frac{\partial f_r}{\partial \omega_r}\right)^\nu \delta\omega_r^\nu = 0 \tag{3.65}$$

$$f_i^\nu + \left(\frac{\partial f_i}{\partial \alpha_r}\right)^\nu \delta\alpha_r^\nu + \left(\frac{\partial f_i}{\partial \omega_r}\right)^\nu \delta\omega_r^\nu = 0 \tag{3.66}$$

Solving for $\delta\alpha_r^\nu$ and $\delta\omega_r^\nu$:

$$\delta\alpha_r^\nu = \frac{1}{\Delta_0}\left[f_i^\nu \left(\frac{\partial f_r}{\partial \omega_r}\right)^\nu - f_r^\nu \left(\frac{\partial f_i}{\partial \omega_r}\right)^\nu\right] \tag{3.67}$$

$$\delta\omega_r^\nu = \frac{1}{\Delta_0}\left[f_r^\nu \left(\frac{\partial f_i}{\partial \alpha_r}\right)^\nu - f_i^\nu \left(\frac{\partial f_r}{\partial \alpha_r}\right)^\nu\right] \tag{3.68}$$

where :

$$\Delta_0 = \left(\frac{\partial f_r}{\partial \alpha_r}\right)^\nu \left(\frac{\partial f_i}{\partial \omega_r}\right)^\nu - \left(\frac{\partial f_i}{\partial \alpha_r}\right)^\nu \left(\frac{\partial f_r}{\partial \omega_r}\right)^\nu \tag{3.69}$$

To obtain the derivatives of f_r and f_i with respect to α_r and ω_r we make use of equation (3.39). Due to the fact that the vector $\vec{r}$ is independent of α_r and ω_r the following set of equations is obtained:

$$A\left(\frac{\partial \vec{\vec{\delta}}}{\partial \alpha_r}\right)^\nu = -\left(\frac{\partial A}{\partial \alpha_r}\right)^\nu \vec{\vec{\delta}}^\nu = \vec{\vec{r}} \tag{3.70}$$

$$A\left(\frac{\partial \vec{\vec{\delta}}}{\partial \omega_r}\right)^\nu = -\left(\frac{\partial A}{\partial \omega_r}\right)^\nu \vec{\vec{\delta}}^\nu = \vec{\vec{r}} \tag{3.71}$$

The vectors on the right-hand side of equations (3.70) and (3.71) are obtained from equations (3.72) - (3.77) by differenciating whit respect to the selected eigenvalues.

$$\begin{aligned} Z_{2(j)} - Z_{2(j-1)} - C_{1(j)}(Z_{1(j)} + Z_{1(j-1)}) & \\ -C_{2(j)}(Z_{3(j)} + Z_{3(j-1)}) = r_{1(j)} & \quad (3.72)\\ Z_{3(j)} - Z_{3(j-1)} + C_{5(j)}(Z_{1(j)} + Z_{1(j-1)}) = r_{2(j)} & \quad (3.73)\\ Z_{5(j)} - Z_{5(j-1)} - C_{3(j)}(Z_{6(j)} + Z_{6(j-1)}) = r_{3(j)} & \quad (3.74)\\ -[Z_{1(j+1)} - Z_{1(j)} - C_{3(j+1)}(Z_{2(j+1)} + Z_{2(j)})] = r_{4(j)} & \quad (3.75)\\ -[Z_{4(j+1)} - Z_{4(j)} + C_{6(j+1)}(Z_{2(j+1)} + Z_{2(j)}) & \\ +C_{7(j+1)}(Z_{3(j+1)} + Z_{3(j)})] = r_{5(j)} & \quad (3.76)\\ -[Z_{6(j+1)} - Z_{6(j)} - C_{8(j+1)}(Z_{3(j+1)} + Z_{3(j)}) & \\ -C_{9(j+1)}(Z_{5(j+1)} + Z_{5(j)})] = r_{6(j)} & \quad (3.77) \end{aligned}$$

From the initial estimate of the eigenvalues (α_r, ω_r) at a given position R and level α_i the linear system of equation (3.39) is solved whit the block elimination method, once this is done the solution is collected. Then the linear system is solved again but with new right hand side values according to equations (3.70) and subsequently whit (3.71). If the increments in $\delta\alpha_r^\nu$ and $\delta\omega_r^\nu$ are below some defined tolerance, it is not needed to adjust the initial condition, and the solution will move to the next station or R value. If this is not the case increments are added to the initial solution as follows:

$$\alpha_r^{\nu+1} = \alpha_r^\nu + \delta\alpha_r^\nu \quad (3.78)$$
$$\omega_r^{\nu+1} = \omega_r^\nu + \delta\omega_r^\nu \quad (3.79)$$

and the procedure is repetead until the tolerance criteria is satisfied.

The technique to calculate the amplification on the unstable are is similar to the one presented, however in this case equation (3.64) is expanded about α_r^ν and α_i^ν as a result:

$$f_r^\nu + \left(\frac{\partial f_r}{\partial \alpha_r}\right)^\nu \delta\alpha_r^\nu + \left(\frac{\partial f_r}{\partial \alpha_i}\right)^\nu \delta\alpha_i^\nu = 0 \quad (3.80)$$
$$f_i^\nu + \left(\frac{\partial f_i}{\partial \alpha_r}\right)^\nu \delta\alpha_r^\nu + \left(\frac{\partial f_i}{\partial \alpha_i}\right)^\nu \delta\alpha_i^\nu = 0 \quad (3.81)$$

solving for $\delta\alpha_r^\nu$ and $\delta\alpha_i^\nu$:

$$\delta\alpha_r^\nu = \frac{1}{\Delta_0}\left[f_i^\nu\left(\frac{\partial f_r}{\partial \alpha_i}\right)^\nu - f_r^\nu\left(\frac{\partial f_i}{\partial \alpha_i}\right)^\nu\right] \tag{3.82}$$

$$\delta\alpha_i^\nu = \frac{1}{\Delta_0}\left[f_r^\nu\left(\frac{\partial f_i}{\partial \alpha_r}\right)^\nu - f_i^\nu\left(\frac{\partial f_r}{\partial \alpha_r}\right)^\nu\right] \tag{3.83}$$

where :

$$\Delta_0 = \left(\frac{\partial f_r}{\partial \alpha_r}\right)\left(\frac{\partial f_i}{\partial \alpha_i}\right)^\nu - \left(\frac{\partial f_i}{\partial \alpha_r}\right)^\nu\left(\frac{\partial f_r}{\partial \alpha_i}\right)^\nu \tag{3.84}$$

The transition computations require that the neutral curve is calculated first, then is needed to follow a set of dimensional frequencies. Increments are calculated as follows:

$$\alpha_r^{\nu+1} = \alpha_r^\nu + \delta\alpha_r^\nu \tag{3.85}$$

$$\alpha_i^{\nu+1} = \alpha_i^\nu + \delta\alpha_i^\nu \tag{3.86}$$

Due to the sharp change close to the tip of the neutral curves, it is required to reformulate the equations, by expanding equation (3.64) around $\delta\omega_r^\nu$ and δR^ν.

The previous method is taken esentially from Cebeci [22], however, has been adapted to include the effect of rotation. The way to deal whit boundary conditions is different. We are solving a 6x6 system, the reason for this is that the formulation with rotational effects is also a 6x6 system, with more difficult boundary conditions.

3.4.4 Improved boundary condition

In the freestream the system of equations (3.21)-(3.26) have independent solutions of the form

$$Z_i^j = A_i^j e^{\lambda_j z} \tag{3.87}$$

To obtain a proper boundary condition the linear system (3.21)-(3.26) is evaluated at the edge of the boundary layer where clearly the shear stress on r and θ directions vanish, that is $f''(\eta_{inf}) = 0$ and $g''(\eta_{inf}) = 0$, that is $C_2 = 0$ and $C_8 = 0$ Due to the fact that an analytic solution is available of the eigenvalues and eigenvectors, for this system. The characteristic values are found to be:

$$\lambda_{1,2} = \pm \left(\alpha^2 + \beta^2\right)^{1/2} \tag{3.88}$$

$$\lambda_{3,4} = \pm \left[\alpha^2 + \beta^2 + iR\left(\alpha U + \beta V - \omega\right)\right]^{1/2} \tag{3.89}$$

$$\lambda_{5,6} = \lambda_{3,4} \tag{3.90}$$

The components of the characteristic vector for the inviscid part are written as:

$$A_1^1 = -i\left(\alpha^2 + \beta^2\right)^{1/2} \tag{3.91}$$

$$A_2^1 = i\left(\alpha^2 + \beta^2\right) \tag{3.92}$$

$$A_3^1 = 1 \tag{3.93}$$

$$A_4^1 = \frac{i\left(\alpha U + \beta V - \omega\right)}{\left(\alpha^2 + \beta^2\right)^{1/2}} \tag{3.94}$$

$$A_5^1 = 0 \tag{3.95}$$

$$A_6^1 = 0 \tag{3.96}$$

In a similar manner for the viscous part:

$$A_1^3 = 1 \tag{3.97}$$

$$A_2^3 = \left[\alpha^2 + \beta^2 + iR\left(\alpha U + \beta V - \omega\right)\right]^{1/2} \tag{3.98}$$

$$A_3^3 = \frac{1}{\left[\alpha^2 + \beta^2 - iR\left(\alpha U + \beta V - \omega\right)\right]^{1/2}} \tag{3.99}$$

$$A_4^3 = 0 \tag{3.100}$$

$$A_5^3 = 0 \tag{3.101}$$

$$A_6^3 = 0 \tag{3.102}$$

The characteristic equation is expanded in Taylor series at the edge of the boundary layer. For a fixed Reynolds number, and α_i, increments in α_r and ω are calculated. The left hand side of the equation is calculated from equations (3.106), (3.107), (3.108). The original boundary conditions are $Z_1(0) = 0$,$Z_3(0) = 0$,$Z_5(0) = 0$ at the wall, as the edge is approached, that is as $\eta \to \infty$ $Z_1(\eta) = 0$,$Z_3(\eta) = 0$,$Z_5(\eta)$. To break the homogeneous condition (the trivial solution), some of the variables that does not form part of the boundary condition can be selected to be modified, and later with the Newton method adjusted until the convergence criteria is satisfied. For this particular case we select the variable $Z_2(\eta_e)$ due to the fact that wall shear stress should be damped out as the edge of the boundary layer is approached. In a similar way the fluctuations of the derivative of the velocities profiles should also be damped.

$$f_e(\alpha, \omega, R) = f_c(\alpha, \omega, R) \tag{3.103}$$

For the real part:

$$f_{er} + \frac{\partial f_{er}}{\partial \alpha_r}\delta\alpha_r + \frac{\partial f_{er}}{\partial \omega}\delta\omega = f_{cr} + \frac{\partial f_{cr}}{\partial \alpha_r}\delta\alpha_r + \frac{\partial f_{cr}}{\partial \omega}\delta\omega \tag{3.104}$$

For the imaginary part:

$$f_{ei} + \frac{\partial f_{ei}}{\partial \alpha_r}\delta\alpha_r + \frac{\partial f_{ei}}{\partial \omega}\delta\omega = f_{ci} + \frac{\partial f_{ci}}{\partial \alpha_r}\delta\alpha_r + \frac{\partial f_{ci}}{\partial \omega}\delta\omega \tag{3.105}$$

Equation (3.106) is the solution of the variable Z_2 at the edge of the boundary layer, where the first terms represent the inviscid contribution and the right the viscous part. The partial derivatives with respect to the eigenvalues are calculated as follows:

$$f_c = A_2^1 e^{\lambda_1 \eta_e} + A_2^3 e^{\lambda_3 \eta_e} \tag{3.106}$$

$$\frac{\partial f_c}{\partial \alpha} = e^{\lambda_1 \eta_e}\left(\frac{\partial A_2^1}{\partial \alpha} + \eta_e \frac{\partial \lambda_1}{\partial \alpha}\right) + e^{\lambda_3 \eta_e}\left(\frac{\partial A_2^3}{\partial \alpha} + \eta_e \frac{\partial \lambda_3}{\partial \alpha}\right) \tag{3.107}$$

$$\frac{\partial f_c}{\partial \omega} = e^{\lambda_1 \eta_e}\left(\frac{\partial A_2^1}{\partial \omega} + \eta_e \frac{\partial \lambda_1}{\partial \omega}\right) + e^{\lambda_1 \eta_e}\left(\frac{\partial A_2^1}{\partial \omega} + \eta_e \frac{\partial \lambda_1}{\partial \omega}\right) \tag{3.108}$$

3.5 Stability diagrams

The eigenvalues from the solution of the equation $f(\alpha, \omega, R) = 0$ are represented in the planes (α, R) and (ω, R) that describe the three states of the disturbances damped, neutral or amplified. The neutral curve, separates the damped region from the amplified region along the curve $\alpha_i = 0$ for the spatial approach and $\omega_i = 0$ for the temporal approach. In the internal part of the curve the disturbances will be amplified, that is when $\alpha_i < 0$. For a relatively small Reynolds number below the critical value all disturbances are damped out, and no amplification takes place, $\alpha_i > 0$. As this parameter is increased the flow becomes more susceptible to external disturbances that arise with different wave lengths and speeds. The point where the first disturbance becomes amplified is called the critical Reynolds number R_{cr}. At this value, the lower and upper branch of the neutral curve intersect with coordinates $(\alpha_{r_{cr}}, \omega_{r_{cr}})$. In the unstable area the flow will respond in a different manner in varying frequencies and wave lengths according to the dimensionless pressure gradient (m).

3.5.1 Characteristics of the stability curves

The maximum frequency ω is found by following the upper branch of the neutral curve, and the position of this frequency can be identified by the peak. At this Reynolds number the biggest range of unstable frequencies occurs. The maximum amplification value of $\alpha_{i_{top}}$ defines the Reynolds number at which concentric curves are formed. The stability diagrams are presented as a set of different level curves at different constant values of αi. The position of this point differs from the position of the maximum frequency. The range of unstable frequencies at this position is also important for establishing the Database.

3.6 Solution of the stability equations for different pressure gradients

The cases presented in this section are the stability of the Hiemenz flow Figure (3.2). This case is found at the stagnation point on an airfoil. The stability of the Blasius velocity profile is shown in figure (3.3) and the solution of the velocity profile before separation is shown in figure (3.4). The technique to determine the solution at different pressure gradients is gradually varying the pressure gradient. At high Reynolds number the solution for different pressure gradients tends to be similar.

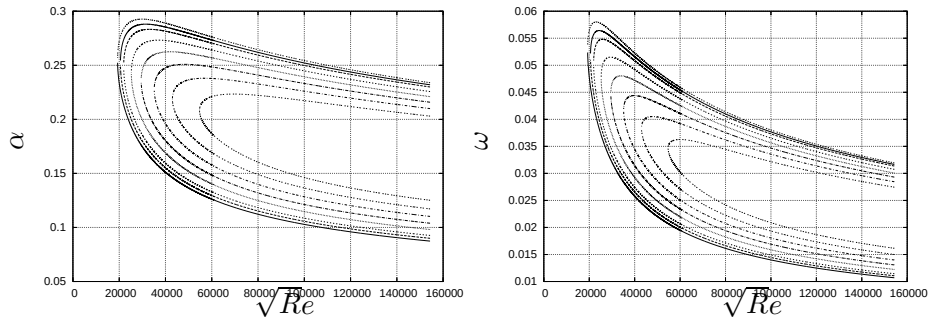

Figure 3.2: Stability curve at m= 1 a) α vs $\sqrt{Re}$ b) ω vs $\sqrt{Re}$

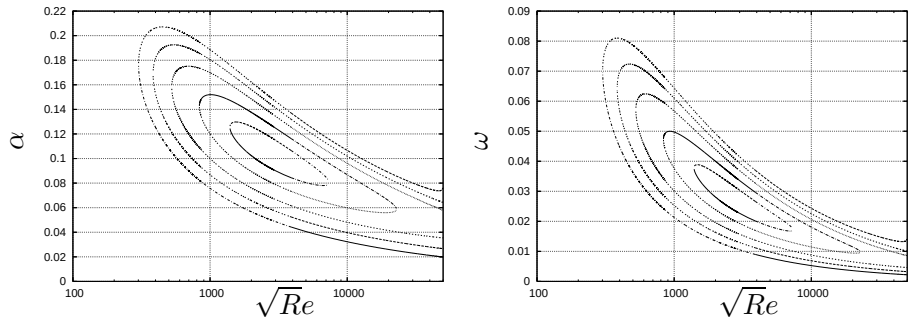

Figure 3.3: Stability curve at m=0 a) α vs $\sqrt{Re}$ b) ω vs $\sqrt{Re}$

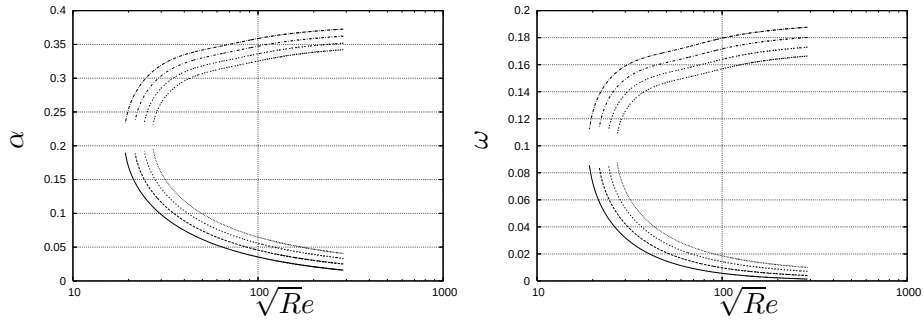

Figure 3.4: Stability Curve at m=-0.0904 a) α vs $\sqrt{Re}$ b) ω vs $\sqrt{Re}$

The first relatively accurate stability diagrams were obtained by Prestch [84], and the most accurate result were presented in the stability curves of Wazzan et al. [112], for both spatial and temporal stability approach.

3.7 Analysis of the Stability parameters

Figure (3.5) shows the position of the coordinates $(\alpha_{cr}, \omega_{cr})$ as the pressure gradient m decreases. The effect of decrease m on the R_{cr} can be seen in Figure (3.6). The maximum frequency that occurs in the plane is presented in Figure (3.7)

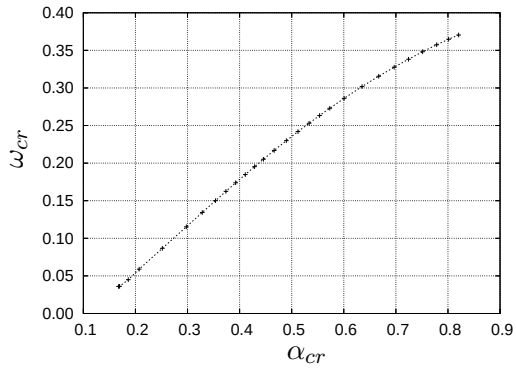

Figure 3.5: Critical coordinates of the Neutral curves for all pressure gradients m

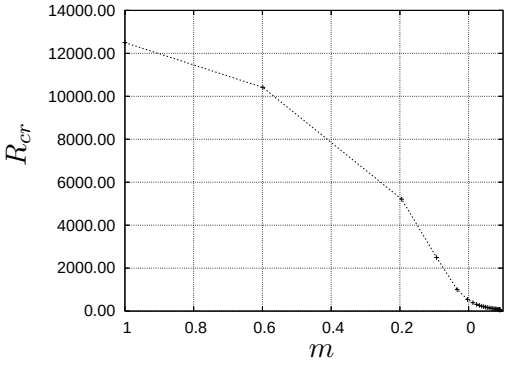

Figure 3.6: Critical Reynolds number versus m

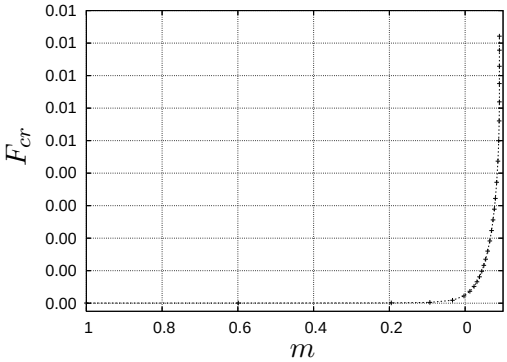

Figure 3.7: Maximum frequency versus m

As the pressure gradients m decreases the flow becomes unstable. The Reynolds number decreases, and the range of unstable frequencies to which the flow is sensible increases. The velocity profiles with positive pressure gradient do not have an inflection point.

In the case of decelerating flow at some position of the boundary layer the flow experiences an inflection point. The position on the inflection point can gives the usual information on the stability of the flow. We may observe that in the boundary layer with favorable pressure gradients, where the viscous instability is the only source, low frequencies are most amplified. On the contrary, in the boundary layer with adverse pressure gradients, the inflectional instability is dominant and high frequency waves are the most amplified.

3.8 Database formulation

The database approach is based on solving the stability equations for different pressure gradients, both favorable and adverse. The neutral curve is divided into four parts, the tip, the region close to the tip, and two more zones where gradually the point spacing along the neutral curve is forced to be coarser according to the critical Reynolds number. In practice the high pressure gradients have no use in the database. For that reason it is not needed to calculate the stability of all pressure gradients. Also the relevant information is the one close to the tip od the neutral curve and the rest of the stability curve has no use for relatively low Reynolds numbers. In the case of a wind turbine blade the maximum Reynolds number based on the chord can be set to $Re_c = 8.5x10^6$. Some extra range is used close to the limit value, in a way that is possible to trace the growth rate of the disturbances originated at that limit. Following a constant dimensional frequency line, at different Reynolds number stations the stability curve for a given pressure gradient. The data are manipulated and finally mapped and stored. Since the condition to cross the unstable area is valid for any given dimensional frequency, the database can be used for any specified Re_c. The idea of the Database approach have been taken essentially from Stock and Degenhart [106]. The extension of including rotational effects is not simple: one of the reasons is that the number of parameters that describe a family of velocity profiles increases. In the 2D case it is only needed to specify for instance the dimensionless parameter m, or the Shape factor that can be more suited for (NS) coupling Pedersen [81]. Additional features can be added, for example, suction, blowing, heat transfer or compressibility. However this effects need to be included in the mean flow calculation and also is pertinent in the stability equations. To establish the Database it is important to follow the physics, so that the database method should also need to be consistent with the propagation laws on 3D flows.

3.9 Range of parameters for the Database

Transition location depends on the pressure distribution of a given geometry, and at the same time depends on the orientation with respect to the mean flow. The important point is to find the position on the geometry where the first disturbance becomes amplified. Then we have to integrate from that point the amplification rate of α_i passing through all the pressure gradients that describe some particular operational condition on a given airfoil.

The Database demands a certain number of points along the neutral curves. Due to the sharp changes close to the tip of the curve, more points are needed in this region. At higher Reynolds number the space between the points can be larger. The advantage of using the spatial approach is that once a point is found on the neutral curve it is easier to build up the curve by taking the solution at the previous station as an initial guess for the next station. Therefore it is very important to find the maximum frequency for a given curve, even if it is not precisely the neutral one. On the unstable area the curves will behave in a similar way. The peak on the stability diagram coincides with the maximum frequency. At this position it is very important to have a fine mesh due to sharp changes.

The classical results of the stability curves are shown in the figures for Reynolds number based on $\sqrt{R}$ up to $10xe5$. In practice the database is made by fixing the maximum Reynolds number that can be found on a wind turbine blade. This value is set to be $8.5x10^6$, with an additional range to follow the growth of the disturbance. The velocity profiles figure (2.9) are very stable and transition will not occur at the stations or positions on a blade that has this pressure gradient. Transition occurs at relatively low pressure gradients, where the Reynolds number is relatively lower. In practice to obtain the Database it is needed to cover just a part of the stability curve.

3.10 Principle of the e^n method

The stability curves show the response of the boundary layer for waves with different wavelengths and frequencies, however, they can not predict onset of transition. To illustrate the principle of the method a disturbance with frequency ω and wave length λ_x can be set on the vertical axes in the planes (α, R),(ω, R) for a chosen pressure gradient m. To follow this particular disturbance, we observe the amplification α_i as the Reynolds number increases or as the disturbance propagates downstream. The first amplification occurs when the flow passes the neutral curve at x_o following a constant value of ω and α already set on the axes. Inside the unstable region the flow will be amplified until it reaches the maximum amplification α_i and will decrease again, depending on the frequency. The flow can become stable again when

the Reynolds number increases at x. If the observation is extended to the range of unstable frequencies in the stability diagrams, a similar behavior is observed, such that all disturbances will be amplified in a different way following different amplification paths. To quantify the rate of amplification of each wave we integrate the amplification α_i in the unstable region according to the expression:

$$ln\left(\frac{A}{A_0}\right) = \int_{x_0}^{x} -\alpha_i dx \tag{3.109}$$

Ao is the initial amplitude that depends on the environment, that can depend on the turbulence intensity of the wind tunnel.

It is worth mentioning that the pressure gradient m will change along the airfoil. The stability will be made for a combination of the previous stability diagrams.

The solution from the eigenvalue problem for $(\alpha, \beta, \omega, R) = 0$ is obtained in dimensionless form according to the reference length and velocity used for the definition of Reynolds number. However for a given case it is needed to follow a constant dimensional frequency ω^*, in a way that the spatial evolution of the growth of amplitude can be traced. Therefore it is required to cross the unstable area. The dimensional quantity can be found from the following:

$$\omega^* = \frac{\omega U^*_{ref}}{L^*}$$

The spatial n-factor is this quantity maximized over all frequencies.

$$n = M_{ax} f[ln(A/A_o)] = ln[(A/A_0)_{max}]$$

Clearly, the waves begin to grow as they enter in the unstable region, where it crosses the lower branch of the neutral-stability curve, and begin to decay as it crosses the upper branch. The low frequencies begin to grow farther downstream than the high frequencies, and they achieve larger amplitudes. The envelope is the curve tangential to the maximum amplification ratio of the considered frequencies in a defined Reynolds number range.

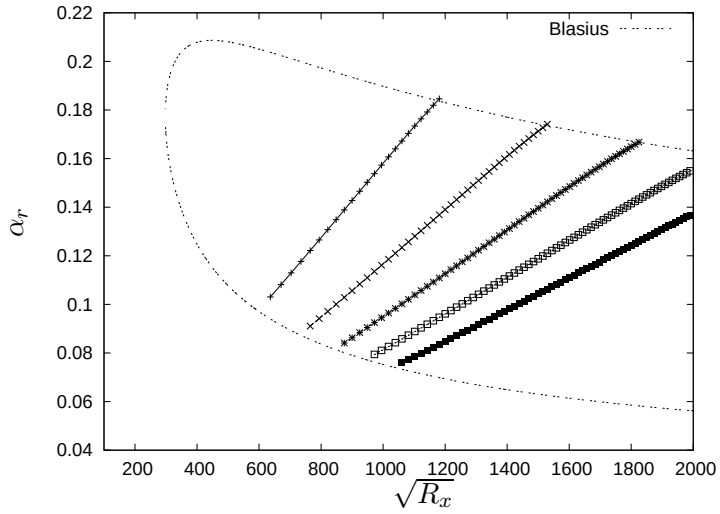

Figure 3.8: Neutral curve for the Blasius velocity profile in the plane $\sqrt{R_x}, \alpha$

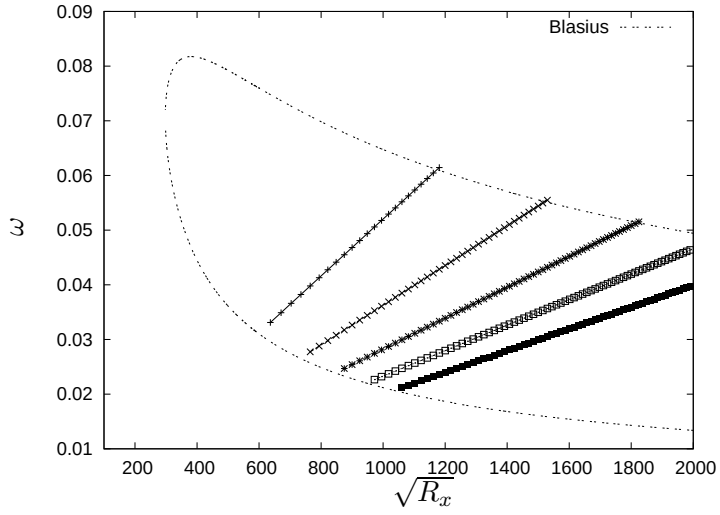

Figure 3.9: Neutral curve for the Blasius velocity profile in the plane $\sqrt{R_x}, \omega$

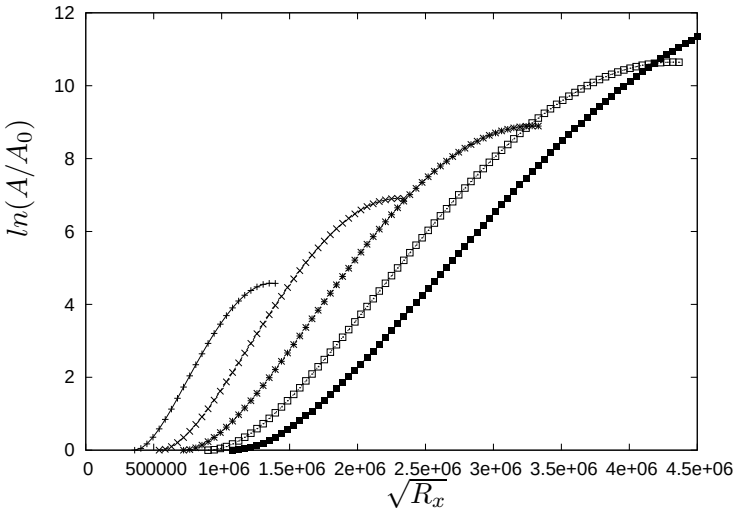

Figure 3.10: Calculation of the amplification for different dimensional frequencies. Blasius velocity profile

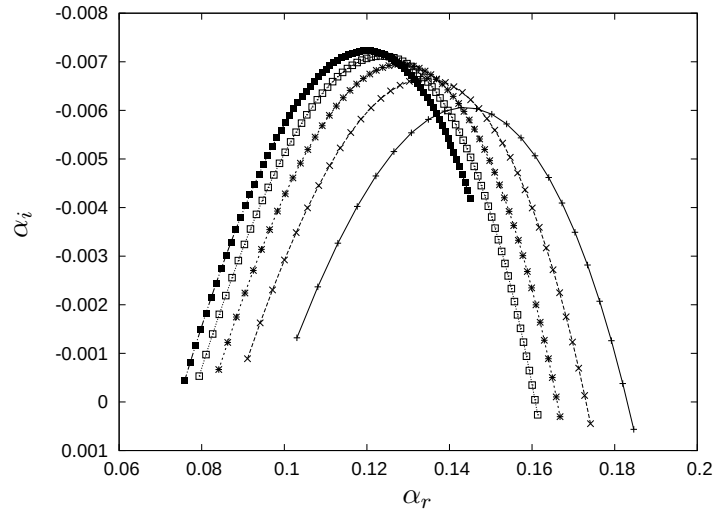

Figure 3.11: Amplification of frequencies inside the unstable region in the plane (α_r, α_i)

The envelope of all the curves represented by different frequencies that eventually turn the flow into turbulent. The method does not describe the mechanism of transition, it simply gives a practical indication of the transition location. The method developed by Van Ingen [46] and Smith [98] has been used for many years due to its simplicity. If the method is

extended for adverse pressure gradients and in the separation region needs special care, as will be discussed in the next Chapter. Naturally the solution demands to have the velocity profiles on the separation bubble. To illustrate the previous method consider a flat plate. Smith assigned a value $n = 9.0$ corresponding to a $Re_{tr} = 2.83310^6$, while Van Ingen $n = 7.8$ at the beginning and $n = 10$ at the end of the transition process. The figures (3.8),(3.11) and (3.9) shows the amplitude development of different physical frequencies in different planes that represent the solution of the eigenvalue problem, recalling the chacteristic equation $f(\alpha_r, \alpha_i, \omega, R) = 0$. At each Rex station associated with one frequency, the maximum amplification ratio is determined, the envelope or tangent curve to the frequency curves on figure (3.10) represents the n factor.

3.11 Limitation of the e^n method

Through the years, experiments have shown that n is not really a universal constant, but depends, for instance, on the free-stream turbulence level of the tunnel. Linear instabilities such as Tollmien-Schlichting waves grow in relatively slow viscous time scale, whereas secondary and subsequent instabilities grow in a much faster convective time scale. Hence a relatively large region of linear growth is followed by a short region of nonlinear growth quickly leading to transition. This seems to be the main reason why the e^n method, which is based on linear stability theory, can be adequate to predict transition onset. Disadvantages of the method are that it does not account for nonlinear effects; it neglects the non-parallel effects, and its extension to 3D boundary layer and instability requires a choice of proper integration strategy in the wave plane. Receptivity is also only indirectly included by properly tuning the n value. Despite of the limitations of the e^n method, the approach is still very popular in airfoil design. This can be attributed to the complexity of the full transition process, which makes it difficult to come with a better design method containing more physics see Henkes and Van Ingen [39]. The method needs to be calibrated with experimental data.

3.12 Summary

The stability of the (FS) family of velocity profiles on the attached flow region was present. Relation among the stability parameters and the boundary layer properties was established. The numerical Method was described whit all details. The procedure to construct the stability curves and the way to move on the multidimesional space of the eigenvalue solution was established. In a similar manner the principles of the e^n method and their restriction was presented.

Chapter 4

Stability with rotational effects

The present Chapter deals whit the formulation of the stability equation on a rotating reference frame, the numerical solution is extended for the effect of rotation. The use of the e^n method for 3D flows will be discussed, in particular the envelope method and beta method. The rotating flat plate is presented, and some selected velocity profiles from the Database already introcuded in Chapter 2. The way to deal with the boundary condition and the solution of the stability equation on a rotating reference frame.

4.1 Closest cases to study transition

The rotating disk case in Schlichting [90] has been used extensively to study the propagation of disturbances in a rotating reference frame. An important convenience for experimental work is that it does not have a pressure-gradient parameter or variable sweep angle, see Lingwood [61]. From a numerical point of view an exact solution of the Navier-Stokes equations for the base flow exists and the shape of the velocity profiles is independent of the radius. The sweep wing of an airfoil has the effect of a variable pressure gradient, and in contrast to the rotating disk it produces lift to maintain the plane. The primary source of energy comes from the turbine, at the operating altitude of the plane where the atmosphere is very stable, the turbulence intensity is very low, even below of what is normally found in a wind tunnel, however is not rotating. The prolate spheroid has been used also to study the transition location at different angles of attacks, due that experimental data are available, it has clearly a 3D flow with cross flow, however it does not include the effect of rotation, see Kreplin et al. [52]. The flow on a wind turbine blade is a combination of the previous cases, but differs in the sense that energy is extracted from the flow to drive the main shaft.

4.2 Derivation of the Stability equations on a rotating reference frame

The common procedure to derive stability equations is introducing disturbances or small deviations from the equilibrium position into equations (2.2)-(2.5). Once the mean flow is subtracted the remaining set of equations in dimensionless form becomes:

$$\begin{aligned} \frac{\partial V_r'}{\partial t} + V_r\frac{\partial V_r'}{\partial r} + \frac{V_\theta}{r}\frac{\partial V_r'}{\partial \theta} + V_z\frac{\partial V_r'}{\partial z} & \qquad (4.1)\\ +V_r'\frac{\partial V_r}{\partial r} + \frac{V_\theta'}{r}\frac{\partial V_r}{\partial \theta} + V_z'\frac{\partial V_r}{\partial z} - 2\frac{V_\theta'}{r}(V_\theta - Ro) &= \\ -\frac{\partial P'}{\partial r} + \frac{1}{Re}\left[\Delta V_r' - \frac{1}{r^2}\left(V_r' + 2\frac{\partial V_\theta'}{\partial \theta}\right)\right] & \end{aligned}$$

$$\begin{aligned} \frac{\partial V_\theta'}{\partial t} + V_r\frac{\partial V_\theta'}{\partial r} + \frac{V_\theta}{r}\frac{\partial V_\theta'}{\partial \theta} + V_z\frac{\partial V_\theta'}{\partial z} & \qquad (4.2)\\ +V_r'\frac{\partial V_\theta}{\partial r} + \frac{V_\theta'}{r}\frac{\partial V_\theta}{\partial \theta} + V_z'\frac{\partial V_\theta}{\partial z} + \frac{1}{r}\left[V_rV_\theta' + 2V_r'(V_\theta - Ro)\right] &= \\ -\frac{1}{r}\frac{\partial P'}{\partial \theta} + \frac{1}{Re}\left[\Delta V_\theta' - \frac{1}{r^2}\left(V_\theta' - 2\frac{\partial V_r'}{\partial \theta}\right)\right] & \end{aligned}$$

$$\begin{aligned} \frac{\partial V_z'}{\partial t} + V_r\frac{\partial V_z'}{\partial r} + \frac{V_\theta}{r}\frac{\partial V_z'}{\partial \theta} + V_z\frac{\partial V_z'}{\partial z} & \\ +V_r'\frac{\partial V_z}{\partial r} + \frac{V_\theta'}{r}\frac{\partial V_z}{\partial \theta} + V_z'\frac{\partial V_z}{\partial z} &= \qquad (4.3)\\ -\frac{\partial P'}{\partial z} + \frac{\Delta V_z'}{Re} & \end{aligned}$$

$$\frac{\partial V_r'}{\partial r} + \frac{V_r'}{r} + \frac{1}{r}\frac{\partial V_\theta'}{\partial \theta} + \frac{\partial V_z'}{\partial z} = 0 \qquad (4.4)$$

Equations (4.1)-(4.4) represent the linearized (NS) equations with respect to the perturbations. In the case of a wind turbine blade the derivatives with respect to the coordinate θ will be kept, while, the normal velocity V_z is assumed to be small and will therefore be neglected from the equations.

4.3 Dimensionless form of the stability equations

Equations (4.1)-(4.4) have been aldeady made dimensionless taking as reference length the Blasius transformation parameters from equations (2.11) and (2.12), the reference velocity is taken as the relative velocity of a blade section V_{rel}^* as shown on equations (4.5)-(4.7). The dimensionless velocities V_r and V_θ in equations(4.1)-(4.4) are in fact g' and f' respectively from equations (2.9) and (2.10).

$$L^*_{ref} = \sqrt{\frac{x^*\nu^*}{U_{xf}V^*_{rel}}} \tag{4.5}$$

$$U^*_{ref} = V^*_{rel} \tag{4.6}$$

$$\xi = \frac{x^*}{c^*} \tag{4.7}$$

The Reynolds number definition can be obtained from the following expression:

$$Re = \frac{L^*_{ref}U^*_{ref}}{\nu*} \tag{4.8}$$

Using this references and manipulating the Coriolis terms, the rotation number Ro, the local solidity c^*/r^* (note that $c^*/r^* = 1/r$) appears in the equations (4.1) and (4.4). These parameters have been previously defined in section 2.3.1.

4.4 Fourier transformation of the stability equations

The small disturbance is assumed to behave like a sinusoidal traveling plane wave. More complicated waves can be represented by the use of Fourier series.

$$V'_r = U(z)e^{i(\alpha r+\beta\theta-\omega t)} \tag{4.9}$$

$$V'_\theta = V(z)e^{i(\alpha r+\beta\theta-\omega t)} \tag{4.10}$$

$$V'_z = W(z)e^{i(\alpha r+\beta\theta-\omega t)} \tag{4.11}$$

$$P' = P(z)e^{i(\alpha r+\beta\theta-\omega t)} \tag{4.12}$$

The terms ($'$) represents the fluctuating velocity components or pressure. The complex amplitude functions in equations (4.9)-(4.12) depend only on the normal coordinate z. In the expressions α represents the wave number in the radial direction, while β, accounts for the wave number in the tangential direction and Ω^* is the circular frequency. Introducing this representations in the linearized (NS) equations (4.1)-(4.4) or in a similar manner taking the Fourier transform in the horizontal directions, the following set of equations is obtained. On the transformation it is assumed that the mean flow velocity components are function of the normal coordinate z and radius, $f = f(r, z)$, the derivatives with respect to θ are neglected. It is also assumed that $V_z = 0$, which differ from the classical parallel flow approximation. However, this

make it possible to obtain a solution at a given airfoil section, or in formal terminology, at some given value of c^*/r^* and still obtain some information of the radial changes of the flow, somehow similar to the approach used on the quasi 3D formulation. To include changes in the radial direction, the solution and formulation of the stability equations becomes more complicated.

Introducing equations (4.9)-(4.12) into (4.1)-(4.4) we obtain :

$$\begin{aligned} V_r'\left(i\alpha V_r + i\bar{\beta}V_\theta - i\omega + \frac{\partial V_r}{\partial r}\right) & \\ +V_z'\frac{\partial V_r}{\partial z} - 2\frac{V_\theta'}{r}\left(V_\theta - Ro\right) &= -i\alpha P' \\ \frac{1}{Re}\left[D^2 - (\alpha^2+\bar{\beta}^2) + \frac{i\alpha}{r}\right]V_r' & \end{aligned} \tag{4.13}$$

$$\begin{aligned} V_\theta'\left(i\alpha V_r + i\bar{\beta}V_\theta - i\omega\right) + V_r'\frac{\partial V_\theta}{\partial r} & \\ V_z'\frac{\partial V_\theta}{\partial z} + \frac{1}{r}\left[V_r V_\theta' + 2V_r'(V_\theta - Ro)\right] &= -i\bar{\beta}P' \\ \frac{1}{Re}\left[D^2 - (\alpha^2+\bar{\beta}^2) + \frac{i\alpha}{r}\right]V_\theta' & \end{aligned} \tag{4.14}$$

$$\begin{aligned} V_z'\left(i\alpha V_r + i\bar{\beta}V_\theta - i\omega\right) &= -DP' \\ \frac{1}{Re}\left[D^2 - (\alpha^2+\bar{\beta}^2) + \frac{i\alpha}{r}\right]V_z' & \end{aligned}$$

$$DVz' + \alpha V r' + \frac{V_r'}{r} + \frac{1}{r}\beta V_\theta' = 0 \tag{4.15}$$

where $\bar{\beta} = \frac{\beta}{r} = \beta\frac{c^*}{r^*}$

4.5 Reference System for stability calculations

The alignment of the local reference system will change according to the potential flow angle ψ_p as can be seen on Figure (4.1). Under some conditions the incoming flow designated by V_{rel}^* can change orientation and deviate from the undisturbed direction, originating a velocity component in the radial direction $V_{r\infty}^*$, commonly refered to as crossflow. Following the flow, at some position downstream the flow will gradually recover the undisturbed direction, the magnitude of the crossflow will decrease progressively and the local reference system will tend to coincide with the fixed reference frame. The wave will make an angle ψ with respect to the x' axis, the vector K represent the resultant of $k = \sqrt{\alpha_r^2 + \beta_r^2}$, where α_r represents the wave number along x' and β_r along r'. It is assumed that the blade has not a sweep angle with respect to the incoming flow (similar to the airplane wing). To predict the transition location it is needed to refer to a particular path or

trajectory, therefore the integration path for transition prediction is defined along the undisturbed free stream. In a similar manner other integration paths or trajectories can be defined, for example, it is also possible to follow an external stream line.
It is very important to distinguish between the potential flow edge angle ψ_p, and the angle made by the velocity components at the edge of the boundary layer β_e. The development of the boundary layer will not necessary follow the streamline direction. It will be inclined to follow some part as seen on the skin friction path. If some changes happen on the potential flow direction, it will take some time for the boundary layer to react and adapt to the new condition. From the reference system, the angle Ψ_p will be adjusted according to the flow, and will change orientation as the flow moves downstream.

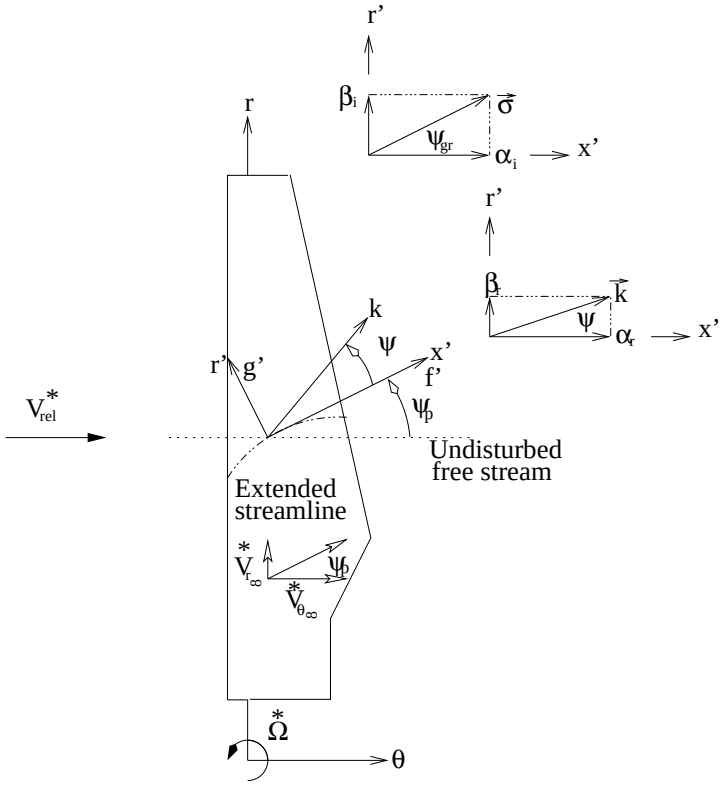

Figure 4.1: Wind Turbine reference system for transition prediction

4.6 Numerical solution of the stability equations

To be able to solve the equations, they are written as an equivalent first order system as described on the keller box scheme. Different formulations

can be used, however the elements on the final matrix must have more or less the same order of magnitude, as discussed by Hansen et al. [43]. We seek the most convenient and advantage way to manipulate the terms. It is pertinent to say that the complication of the solution on the Keller Box scheme and the boundary conditions depend on the selection of the variables. By defining the following equations and following a similar procedure as the one described on section 3.4.1.

$$Z_1 = (\alpha - i/r)V_r' + \bar{\beta}V_\theta' \tag{4.16}$$
$$Z_2 = (\alpha - i/r)DV_r' + \bar{\beta}DV_\theta' \tag{4.17}$$
$$Z_3 = V_z' \tag{4.18}$$
$$Z_4 = P' \tag{4.19}$$
$$Z_5 = (\alpha - i/r)V_\theta' - \bar{\beta}V_\theta' \tag{4.20}$$
$$Z_6 = (\alpha - i/r)DV_\theta' - \bar{\beta}DV_\theta' \tag{4.21}$$

The equivalent first order system can be written as:

$$b = \left[i\left(\alpha g' + \bar{\beta}f' - \omega\right) + \frac{1}{Re}\left(\alpha^2 + \bar{\beta}^2 - \frac{i\alpha}{r}\right)\right]$$
$$DZ_1 = Z_2 \tag{4.22}$$
$$DZ_2 = Z_1\left(b + \frac{\partial V_r}{\partial r}\right) + Z_3 Re\left((\alpha - (i/r))g'' + \bar{\beta}f''\right)$$
$$+Z_4 i\left(\alpha^2 + \bar{\beta}^2 + \alpha/r\right) - Z_5\frac{2Re}{r}(f' - Ro) \tag{4.23}$$
$$DZ_3 = -iZ_1 \tag{4.24}$$
$$DZ_4 = -iZ_2/Re - Z_3 b \tag{4.25}$$
$$DZ_5 = Z_6 \tag{4.26}$$
$$DZ_6 = Z_1\frac{2Re}{r}(f' - Ro) + Z_3 Re\left(\alpha g'' - (\beta - i/r)/Ref''\right)$$
$$+Z_4\alpha + Z_5\left(b + \frac{\partial V_\theta}{\partial r}\right) \tag{4.27}$$

whit boundary conditions:

$$Z_1(0) = 0, Z_3(0) = 0, Z_5(0) = 0 \tag{4.28}$$
$$Z_1(z) \to 0, Z_3(z) \to 0, Z_5(z) \to 0..as..z \to \infty \tag{4.29}$$

The radial derivatives of the mean flow can be included on the stability analysis, can form part of the Database, due to the fact that can be written in terms of the parameters used on the rotating configuration. The way to

derive the following equations it is basically combine the dimensionless parameters used on the boundary layer formulation on section 2.3, with the dimensionless form of the stability equations section 4.3, with carefull,patience and wise manipulations the following set is obtained:

$$\frac{\partial V_\theta}{\partial r} = f' Ro^2 \frac{1}{r} - \eta f'' \frac{1}{2r}\left(1 - Ro^2\right)$$
$$\frac{\partial V_r}{\partial r} = g' Ro^2 \frac{1}{r} - \eta g'' \frac{1}{2r}\left(1 - Ro^2\right)$$

The magnitude of this terms is changing along the boundary layer, that is on the variable η, is not surprising that as the paremeter c^*/r^* or $1/r$ tends to zero the effect of this radial terms decreases. The following constants (4.30)-(4.40) are obtained from the equations (4.22)-(4.27).

$$C_1 = b + \frac{\partial V_r}{\partial r} \tag{4.30}$$
$$C_4 = Re((\alpha - (i/r))g'' + \bar{\beta} f'') \tag{4.31}$$
$$C_5 = i(\alpha^2 + \bar{\beta}^2 + \alpha/r) \tag{4.32}$$
$$C_6 = -\frac{2Re}{r}\left(f' - Ro\right) \tag{4.33}$$
$$C_7 = -i \tag{4.34}$$
$$C_9 = -i/Re \tag{4.35}$$
$$C_{10} = -b \tag{4.36}$$
$$C_{11} = 2Re\left(\frac{f' - Ro}{r}\right) \tag{4.37}$$
$$C_{12} = Re(\alpha g'' - ((\beta - i/r)/Re) f'') \tag{4.38}$$
$$C_x = \alpha \tag{4.39}$$
$$C_{13} = Reb + \frac{\partial V_\theta}{\partial r} \tag{4.40}$$

By the use of the constants (4.30) and (4.40) the system can be written as $Z' = AZ$, $Z = (Z_1, Z_2, Z_3, Z_4, Z_5, Z_6)^T$

where the matrix A is given as:

$$\mathbf{A} = \begin{pmatrix} 0 & 1 & 0 & 0 & 0 & 0 \\ C_1 & 0 & C_4 & C_5 & C_6 & 0 \\ C_7 & 0 & 0 & 0 & 0 & 0 \\ 0 & C_9 & C_{10} & 0 & 0 & 0 \\ 0 & 0 & 0 & 0 & 0 & 1 \\ C_{11} & 0 & C_{12} & C_x & C_{13} & 0 \end{pmatrix}$$

To obtain the propagation angle ψ the edge angle g'_e (2.26) can be used as initial guess.

4.6.1 Discretization of the Stability equations whit rotational effects

To formulate the numerical scheme for the equations the equations (4.22)-(4.27), whit variables defined (4.30)-(4.40) we write the finite difference approximations at the midpoints of the cell in the normal direction, using central-difference derivatives on non uniform mesh as follows:

$$\frac{Z_{1(j)} - Z_{1(j-1)}}{h_{(j-1)}/2} = (Z_{2(j)} + Z_{2(j-1)}) \quad (4.41)$$

$$\begin{aligned}\frac{Z_{2(j)} - Z_{2(j-1)}}{h_{(j-1)}/2} &= C_{1(j)}(Z_{1(j)} + Z_{1(j-1)}) + C_{2(j)}(Z_{2(j)} + Z_{2(j-1)}) \\ &\quad + C_{4(j)}(Z_{3(j)} + Z_{3(j-1)}) \\ &\quad + C_{5(j)}(Z_{4(j)} + Z_{4(j-1)}) + C_{6(j)}(Z_{5(j)} + Z_{5(j-1)}) \quad (4.42)\end{aligned}$$

$$\frac{Z_{3(j)} - Z_{3(j-1)}}{h_{(j-1)}/2} = -C_{7(j)}Z_{1(j)} - Z_{1(j-1)} \quad (4.43)$$

$$\begin{aligned}\frac{Z_{4(j)} - Z_{4(j-1)}}{h_{(j-1)}/2} &= -C_{8(j)}(Z_{1(j)} + Z_{1(j-1)}) - C_{9(j)}(Z_{2(j)} + Z_{2(j-1)}) \\ &\quad - C_{10(j)}(Z_{3(j)} + Z_{3(j-1)}) \quad (4.44)\end{aligned}$$

$$\frac{Z_{5(j)} - Z_{5(j-1)}}{h_{(j-1)}/2} = (Z_{6(j)} + Z_{6(j-1)}) \quad (4.45)$$

$$\begin{aligned}\frac{Z_{6(j)} - Z_{6(j-1)}}{h_{(j-1)}/2} &= C_{11(j)}(Z_{1(j)} + Z_{1(j-1)}) \\ &\quad + C_{12(j)}(Z_{3(j)} + Z_{3(j-1)}) \\ &\quad + C_{x(j)}(Z_{4(j)} + Z_{5(j-1)}) + C_{13(j)}(Z_{5(j)} + Z_{5(j-1)}) \quad (4.46)\end{aligned}$$

The system of equations can be written as an equivalent three diagonal matrix as follows:

$$A_j = \begin{pmatrix} -C_1 & 1 & -C_{4j} & -C_{5j} & -C_{6j} & 0 \\ C_{7j} & 0 & 1 & 0 & 0 & 0 \\ 0 & 0 & 0 & 0 & 1 & -C_{3j} \\ 1 & C_{3j+1} & 0 & 0 & 0 & 0 \\ C_{8j+1} & -C_{9j+1} & -C_{10j+1} & 1 & 0 & 0 \\ C_{11j+1} & 0 & C_{12j+1} & C_{xj+1} & C_{13j+1} & 1 \end{pmatrix}$$

$$B_j = \begin{pmatrix} -C_{1j} & -1 & -C_{4j} & -C_{5j} & -C_{6j} & 0 \\ C_{7j} & 0 & -1 & 0 & 0 & 0 \\ 0 & 0 & 0 & 0 & -1 & -C_{3j} \\ 0 & 0 & 0 & 0 & 0 & 0 \\ 0 & 0 & 0 & 0 & 0 & 0 \\ 0 & 0 & 0 & 0 & 0 & 0 \end{pmatrix}$$

$$C_j = \begin{pmatrix} 0 & 0 & 0 & 0 & 0 & 0 \\ 0 & 0 & 0 & 0 & 0 & 0 \\ 0 & 0 & 0 & 0 & 0 & 0 \\ -1 & C_{3j+1} & 0 & 0 & 0 & 0 \\ C_{8j+1} & -C_{9j+1} & -C_{10j+1} & -1 & 0 & 0 \\ C_{11j+1} & 0 & C_{12j+1} & C_{xj+1} & C_{13j+1} & -1 \end{pmatrix}$$

With Boundary conditions at the wall:

$$A_0 = \begin{pmatrix} 0 & 1 & 0 & 0 & 0 & 0 \\ 0 & 0 & 1 & 0 & 0 & 0 \\ 0 & 0 & 0 & 0 & 1 & 0 \\ 1 & C_{3_1} & 0 & 0 & 0 & 0 \\ C_{8_1} & -C_{9_1} & -C_{10_1} & 1 & 0 & 0 \\ C_{11_1} & 0 & C_{12_1} & C_{x_1} & C_{13_1} & 0 \end{pmatrix} \tag{4.47}$$

at the edge:

$$A_J = \begin{pmatrix} -C_{1_J} & 1 & -C_{4_J} & -C_{5_J} & -C_{6_J} & 0 \\ C_{7_J} & 0 & 1 & 0 & 0 & 0 \\ 0 & 0 & 0 & 0 & 1 & -C_{3_J} \\ 1 & 0 & 0 & 0 & 0 & 0 \\ 0 & 0 & 1 & 0 & 0 & 0 \\ 0 & 0 & 0 & 0 & 1 & 0 \end{pmatrix} \tag{4.48}$$

matrix Δ_j whit rotational effects:

$$\Delta_j = \begin{pmatrix} \alpha_{11_j} & \alpha_{12_j} & \alpha_{13_j} & \alpha_{14_j} & \alpha_{15_j} & \alpha_{16_j} \\ \alpha_{21_j} & \alpha_{22_j} & \alpha_{23_j} & \alpha_{24_j} & \alpha_{25_j} & \alpha_{26_j} \\ \alpha_{31_j} & \alpha_{32_j} & \alpha_{33_j} & \alpha_{34_j} & \alpha_{35_j} & \alpha_{36_j} \\ -1 & C_{3_j} & 0 & 0 & 0 & 0 \\ C_{8_j} & -C_{9_j} & -C_{10_j} & -1 & 0 & 0 \\ C_{11_j} & 0 & C_{12_j} & C_{x_j} & C_{13_j} & -1 \end{pmatrix} \tag{4.49}$$

And the right hand side vectors:

$$Z_{1(j)} - Z_{1(j-1)} - C_{3(j)}(Z_{2(j)} + Z_{2(j-1)}) = r_{1j} \quad (4.50)$$

$$Z_{2(j)} - Z_{2(j-1)} - C_{1(j)}(Z_{1(j)} + Z_{1(j-1)}) - C_{2(j)}(Z_{2(j)} + Z_{2(j-1)}) - C_{4(j)}(Z_{3(j)} + Z_{3(j-1)})$$

$$-C_{5(j)}(Z_{4(j)} + Z_{4(j-1)}) - C_{6(j)}(Z_{5(j)} + Z_{5(j-1)}) = r_{2j} \quad (4.51)$$

$$Z_{3(j)} - Z_{3(j-1)} + C_{7(j)}(Z_{1(j)} - Z_{1(j-1)}) = r_{3j} \quad (4.52)$$

$$-[Z_{4(j+1)} - Z_{4(j)} - C_{8(j+1)}(Z_{1(j+1)} + Z_{1(j)}) + C_{9(j+1)}(Z_{2(j+1)} + Z_{2(j)}) + C_{10(j+1)}(Z_{3(j+1)} + Z_{3(j)})] = r_{4j} \quad (4.53)$$

$$-[Z_{5(j+1)} - Z_{5(j)} - C_{3(j+1)}(Z_{6(j+1)} + Z_{6(j)})] = r_{5j} \quad (4.54)$$

$$-[Z_{6(j+1)} - Z_{6(j)} - C_{11(j+1)}(Z_{1(j+1)} + Z_{1(j)}) - C_{12(j+1)}(Z_{3(j+1)} + Z_{3(j)}) - C_{x(j+1)}(Z_{4(j+1)} + Z_{5(j)}) - C_{13(j+1)}(Z_{5(j+1)} + Z_{5(j)})] = r_{6j} \quad (4.55)$$

4.6.2 Boundary condition

To obtain the boundary condition, the linear system (4.22)-(4.27) is evaluated at the edge of the boundary layer where the shear stresses on r and θ directions vanish, implying that $f''(\eta_\infty) = 0$ and $g''(\eta_\infty) = 0$, that is $C_4 = 0$ and $C_{12} = 0$. The velocity profiles take the following values $f'(\eta_\infty) = 1$ and $g'(\eta_\infty) = g'_e$.

The previous matrix A can be simplified if the rotation number is set to 1, (implies that $g'_e = 0$) where analytic expressions for the characteristic values and vectors (eigenvalues and eigenvectors) can be found. This coincides with the formulation of the boundary conditions for a rotating disk, Lingwood [60], of course, just regarding two elements A_{61} and A_{25}. The reason behind is that in contrast with a wind turbine blade, the rotating disk does not have the effect of changing the incoming flow angle with the radial position.

In the freestream the system of equations (4.22)-(4.27) have independent solutions of the form

$$Z_i^j = A_i^j e^{\lambda_j z} \quad (4.56)$$

The characteristic values λ_j are obtained by solving the eigenvalue problem for the matrix A. From the solution, the characteristic values occur in pairs. To be able satisfy the boundary condition as $Z \to \infty$ the only admissible values of λ_j are negative to ensure that disturbances damp out as the edge is approached. To obtain the components A_i^j of the characteristic vector, equation (4.56) is substituted in the set of equations (4.22)-(4.27).

In the case that the rotation number is different from one, it is not possible to find an analytic solution for the characteristic values and vectors. This fact requires a numerical procedure. The technique is essentially solving for the characteristic values first, once the polynomial of order 6 is found, it can be further expressed as an equivalent polynomial of order 3. For this cubic equation it is possible to use standard formulas, like for example the Cardano method.

4.6.3 Initial condition

The rotational effects modify the shape of the velocity profile as mentioned on section (2.7). The initial solution is different from the stability of the 2D Database, according to the parameters that describe the flow on a rotating configuration. The technique is to increase gradually the radial pressure gradient n to obtain the desired solution.

4.7 Instability modes

The laminar boundary layer on the wind turbine blade has four fundamental instability modes: attachment line, streamwise, crossflow and the centrifugal (due to the concave region at the leading edge). In addition the effect of rotation of the blade acts to stabilize the flow. Note that in the zone from the stagnation line to the rotor plane, the effect of rotation is creating an instability. This modes or mechanisms may exist independently or in combinations. In practice the most important effects are caused by the (TS) and (CF) instabilities.

It is difficult to model all the instability modes at the same time, or even look at the interaction of some of them. The tangential component is sensible to the geometry of the blade and the free stream turbulence in the incoming flow. In positions with favorable pressure gradient this component is very stable as seen in the stability diagram in figure (3.2). In the zones where the flow is de-accelerated, the velocity is susceptible to be amplified at relatively small Reynolds numbers see figure (3.4) and Section (3.7). The radial component in contrast is highly unstable in the zones where the flow is accelerated, specially around the attachment line and the leading edge of the blade. For some operational conditions, the main flow is directed almost in the radial direction, following the development downstream. At some position, the flow will recover gradually in the tangential direction and the magnitude of the cross flow will decrease. In the case of an airplane wing this type of instability can be attributed to the sweep angle. For a wind turbine blade the sweep angle is constant, but the incoming angle of the flow changes with respect to the radial position. This feature can induce the cross flow instability for some operational conditions, especially at low tip speed ratio or low rotation numbers, as was observed on a full NS solution

on the EllipSys3D code Sørensen [108] for varying wind speeds for example the computations on the NREL rotor at different wind speeds. If transition does not occurs in the area close to the leading edge and the flow evolves towards the separation zone, the effect of the cross flow will be different. It will increase the wall shear stress of the tangential component making the tangential component more stable. One particular feature of the cross flow it is that is sensible to the roughness and imperfections of the surface.
Gray, W.E. discovered the cross flow instability by noting that transition occurs much before on swept wings than on unswept wings. By using evaporation methods, he found regularly spaced vortices whose axes lie in the streamwise direction. In subsequent investigation the existence of such vortices was confirmed by Gregory and Walker [37]. Gray in his visualization experiments showed that transition occurs at much lower Reynolds number on swept wings that unswept wings, and that, before transition the surface of the wing is covered with stationary striped pattern lying in the streamwise direction, which was explained as a series of stationary vortices in the boundary layer. The classical paper of Gregory, Stuart & Walker [36] showed the same behavior in the rotating disk boundary layer. Since then work of a rotating disk have been used extensively as a model for boundary layer on a swept wing.

4.7.1 Attachment line

An important consideration is that along the attachment line there is not a crossflow component and a self similar solution exist only if the flow is laminar. This particular line (the line refers to a simple geometry, similar to symmetrical bodies of a constant chord and an infinite span, the classical example is the swept cylinder) or path on a wind turbine blade can be viewed as a limiting streamline that divides the flow to follow either the suction or pressure side of the blade. One important characteristic is that the boundary layer properties are constant along this path. To study or model how the flow recovers from the radial flow and gradually turn into the tangential direction, it is then also needed to include the effect of rotation and memory of the flow, the Falkner-Skan-Cooke (FSC) velocity profiles are not completely accurate.

In order to study the influence of the three dimensionality of the mean flow on boundary layer stability, it is necessary to develop a family of boundary-layers where the magnitude of the crossflow can be varied in a systematic manner. One of the parameters is the usual dimensionless pressure gradient in the tangential direction m, and another one is the ratio between the spanwise and chordwise velocity Mack [65].
A similar approach is required where it is possible to vary in a systematic manner the propagation angle ψ in the zone that includes the attachment

line and the area between the rotor plane. This demands that the equations are formulated along the attachment line, Arnal [9] explained in detail the formulation of the attachment line equations for a sweep wing.

4.8 Group Velocity

The group velocity it is the velocity by which the energy of a wave travels in some direction, and is identical to the rate of energy transport for harmonic wave fields. The direction of the velocity vector at any point in space defines the direction of flow of the energy (rays).

$$\vec{V_g} = \left(\frac{\partial \omega}{\partial \alpha}, \frac{\partial \omega}{\partial \beta} \right)$$

If we talk about an ideal process of energy transfer the propagation direction is the group velocity. This is an ideal case, in practice, some irreversibilities will ocur on the process, the question is how the direction is changing according to the propagation and amplitude of the disturbance.

Wazzan [113] mentioned that in the unstable case, energy is transferred from the mean flow to the disturbance, whereas in the damped case energy is transferred in the opposite direction.

Cebeci and Stewartson [15] commented that the group velocity of a wave packet in a dispersive medium gives the speed of propagation through space. There is however little published literature for dissipative media. This property is unusual in dissipative systems, but is well known in the theory of general dispersive systems, a good example being provided by Rossby waves. It has been realized in recent years that the application of the usual normal-mode approach to anything but a two-dimensional wave in a two dimensional boundary layer requires the specification of a direction of wave growth in order to arrive at a spatial amplification rate, and hence at a wave amplitude. For conservative wave motion in a slowly varying dispersive medium, amplitude propagation is in the direction of the group velocity. For non-conservative dispersive wave motion, the group velocity vector is complex.

4.9 Extension of the e^n method to 3D flows

Transition location for a given geometry and operational conditions depends on the direction, magnitude and growth rate of the disturbances that propagate through the boundary layer. For 3D flows the solution of the eigenvalue problem involves two wave numbers α and β. (The interaction of these parameters inside the unstable area of the stability curves plays a crucial

role in the amplification of the waves). In the case of using spatial theory the wave numbers are real and the circular frequency is complex. The angle ψ made by α and Ω^* is a real variable, and the characteristic equation can be written as $f(\alpha_r, \beta_r, \omega_r, \omega_i, Re)$=0. For the spatial theory, the solution of the eigenvalue problem involves an extra parameter due to the fact that the wave numbers are complex and the circular frequency is real $f(\alpha_r, \beta_r, \alpha_i, \beta_i, \omega_r, Re)$=0. The main problem to calculate the transition location is the determination of the propagation direction of the disturbance, in a way that the integration of the amplification factor can be accurately made. Before establishing the transition criteria in a similar manner like the e^n method it is mandatory to estimate the propagation direction of the disturbances in the boundary layer. Two important issues need to be clarified: the first one is that disturbances do not propagate arbitrary in the boundary layer, they must obey some principles or laws; the other restriction is that it is not possible to transfer all the energy from the mean flow to the disturbance, some irreversibility will be present in the unstable zone. The medium where the disturbance develops play an important role in the propagation, and can be either dispersive, dissipative or both. According to Mack [66] the boundary layer can be viewed as a nonuniform, anisotropic medium for the propagation of laminar instability waves. Through the boundary layer is present shear flow and the wave motion is dispersive and nonconservative, with both damping and amplification.

With respect to the first issue, the principle of causality stipulates that there can not be any disturbance of the flow before excitation, it defines the paths of the necessary integration contours (as a results of this principle physical solutions are obtained). The other issue is connected with the response of the flow to impulse excitation: it can be stable, convectively unstable or absolutely unstable. The distinguishing feature of the absolutely-unstable case is that the response spreads into regions on both sides of the source, so that disturbances grow in time at fixed radial positions. In contrast, the convectively-unstable case shows a disturbance propagating away from the source as it grows, leaving the source area undisturbed. Absolute instability can be identified by singularities in the dispersion relationship that occurs when waves that propagate energy in opposite directions coalesce. Reverse mean flow is often thought to be related to absolute instability, because it provides a mechanism for upstream effects. For that reason special care is needed on the separation bubble or for instance with a flap control mechanism. Detailed formulation of the present approach can be found from Lingwood [59].

Prior to transition the transfer of energy from the main flow to the disturbance is subject to irreversibilities, and not all the energy can be transfer to the disturbance. In that sense the e^n method can be viewed as an ideal process and is based on the assumption that the flow is convectively unstable. Lingwood [62] discussed in detail a formal study of the e^n method

and the inequality of the transition prediction techniques in 3D flow.

4.9.1 Envelope method

In this class of method the amplification rate is maximized at each streamwise position with respect to the propagation direction, and it does not distinguish between the streamwise and crossflow instability. It is common to obtain relatively high values of the N factors in comparison with the other strategies, due to the fact that it represents the effect of the two instability mechanisms. This method was effectively used by Cebeci and Stewartson [15] and it is based on the saddle point and the notion of the group velocity. The difference with respect to the other approaches is that the relationship between the wave numbers α and β is not assumed, β_i is computed instead. (For each frequency the wave angle is optimized to obtain the maximum growth rate at each downstream position, which are then integrated between the chosen start and end points, and then integrated growth rates are then maximized over all Ω^*). The method is capable of tracking the growth of a physical wave. However, it is valid only for parallel or slightly nonparallel flows, see Nayfeh [78]. On the methodology of the calculation of the n factor, a special neutral curve for the 3D problem is obtained where the transition calculation begins. Cebeci and Stewartson have given the name of "Zarf" . Along this absolute neutral curve no transfer of energy is given to the boundary layer or to the disturbance. On this curve $\alpha_i = 0$, $\beta_i = 0$, and $\partial\alpha/\partial\beta$ a real value. The curve can not be extended to Reynolds number lower that the critical value.

Cebeci and Stewartson [17] observed that the Zarf for the Blasius velocity profile on the upper branch coincides exactly with the neutral curves of the 2D case, however the lower branch is extended (the inviscid part). It is not surprising that the envelope curve is bigger than the corresponding 2D case.

4.9.2 Envelope of Envelopes method - Beta method

In this strategy the streamwise and crossflow disturbances are implicitly separated and the propagation angle is kept constant during the integration. To obtain the growth rates, waves with constant dimensional frequency ω^* and dimensional wave vector in the radial direction β^* are traced. The N factor represent the envelope of several envelopes.

With the fixed beta method of Arnal et al. [5], we uncouple the two mechanisms, but still we have the effect of the cross flow in the tangential direction. Since we do not know the amplification, an optimization strategy is needed. Therefore it is required to calculate the envelope of all the envelopes for given values of beta. If we allow $\beta_i \neq 0$ then we have the effect of the amplification or damping of the cross flow.

4.9.3 Comparison of the integration strategies for the e^n method

According to the selected method or strategy the n factor values will give a different answer. What makes complicated to establish a unique criteria is the presence of the two main transition mechanism, the (TS) and (CF) instability. The (CF) dominates at low Reynolds numbers while the (TS) usually is stronger in zones of adverse pressure gradients. In the case of the flow past an airfoil this process takes place some distance behind the suction peak. The maximization procedure is complicated because of the interaction of the two instability mechanisms. It is difficult to choose an integration path and catch the changes of the two modes. The envelope method represents the contribution of the two mechanism that explain the high N value. The beta method obtain usually lower values, and in some conditions pathological cases are found (n factor lower than 7). The two N factors method, as the numbers indicates it account for 2 factors, one for the (TS) and another for the (CF). The (TS) is well known, and requires some numerical artifacts but indicates the complexity of the problem. So transition will take place at some combination of the two values. Some comparisons among the different strategies have been carried out by Schrauf et al. [95] By comparing with experiments, it was found that, the frequency responsible for the transition is the same in the envelope and beta method and form part of the envelope in the traditional e^n method in 2D case.

The envelope of envelopes strategy, or beta method, describe a physical reality due to the fact that waves maintain constant dimensional frequency in steady flows. It is also assumed to be true that the imaginary part of the spanwise wave vector is zero $\beta_i = 0$ that in a sense is not completely correct. However, this simplifies the solution and make it possible to follow the frequency in a similar approach like the corresponding 2D case.

The conclusion from Mack [63] seems to be the correct: Even with linearization, no definitive theory is as yet available for calculating wave amplitudes in a physical correct manner. The work done in this report is to study the effect of rotation on the stability of the boundary layer without providing the precise location of the transition, however the tendency on the transition location can be seen by simple integration strategies. It is clear that verification and calibration with experimental data will have to compliment the numerical simulations.

4.9.4 Selection of the transition prediction strategy

The fixed beta method will be used to calculate increments on the amplification of the wave number α_i. To cross the unstable region, for a given dimensional frequency or in an equivalent manner at some defined Reynolds number, it is required first to obtain the lower branch of the neutral curve.

To be able to do so we keep constant β_r as we move downstream. For a given β_r a unique neutral curve will be found. The effect of increasing β_r is that the neutral curve will tend to a lower area, the unstable area is decreased and the critical Reynolds number will tend to higher values.

If $\beta_r = 0$ is set in the stability equations, the problem does not reduce to the neutral curve of Blasius, because that in the boundary layer equations we still have the parameters c^*/r^* and x^*/c^* and Ro. It is even surprising that if we set $c^*/r^* = 0$, $x^*/c^* = 0$ and $Ro = 0$ in the stability equations, the solution of Blasius will not be recovered, due to the fact that the memory of the flow has an effect on the stability of the boundary layer, the Database of velocity profiles is used as an input to the stability code. In principle, if we use a 2D potential flow calculation, it is possible to assume that the maximum amplification will occur in that direction, and it is not further needed to give a broad range for the β_r. This is not contradictory having a relatively big cross flow in the boundary layer and the disturbance aligned with the potential flow direction (undisturbed free stream). In this approximation is implicit and error, due to the fact that the disturbance can propagate at small angles from the potential flow direction, but for preliminary results can be used as a first estimate. If this modification is implemented in the EllipSys3D code, it will already improve the prediction of the laminar turbulent transition, according to the approach of Dagenhart [26].

4.10 Stability of the Rotating flate plate

The study of the rotating flat plate case is in particular attractive due to the fact that it is considered as a generalization of the solution of the stability problem of the Blasius flow (Flat plate) in a rotating reference frame. The information provided by this case will be useful to extend for different families of velocity profiles, with both favorable and adverse pressure gradients. The main idea of the present analysis is to estimate the effect of the parameters that govern the solution of the mean flow with (RE) and the effect on the solution of the characteristic equation:

$$f_e(\alpha_r, \alpha_i, \beta_r, \beta_i, \omega_r, \omega_i, Re, Ro, c^*/r^*, m, n) = 0 \tag{4.57}$$

To begin the discussion let's consider the case with no amplification of disturbances in the tangential and radial directions, $\alpha_i = 0$ and $\beta_i = 0$. The attention is centered on the neutral response. In the case of a temporal approach this is simply achived by setting $\omega_i = 0$. The remaining part is to find a way to connect α_r with ω_r and β_r with Ω^*. Setting $\beta_i = 0$ and $\omega_i = 0$, represent the neutral response, the eigenvalue problem reduces to $f(\alpha_r, \beta_r, \omega_r, Re) = 0$. Therefore one more parameter must be specified. One possible way is to fix the dimensionless frequency ω_r and calculate

the increments in $(\delta\alpha_r, \delta\beta_r)$, or fixing β_r and calculate the increments in $(\delta\alpha_r, \delta\omega_r)$, as usual for 2D solution, but with a given β_r. To that end, let as assume that the disturbance is aligned with the potential flow direction, therefore $\beta_r = 0$.

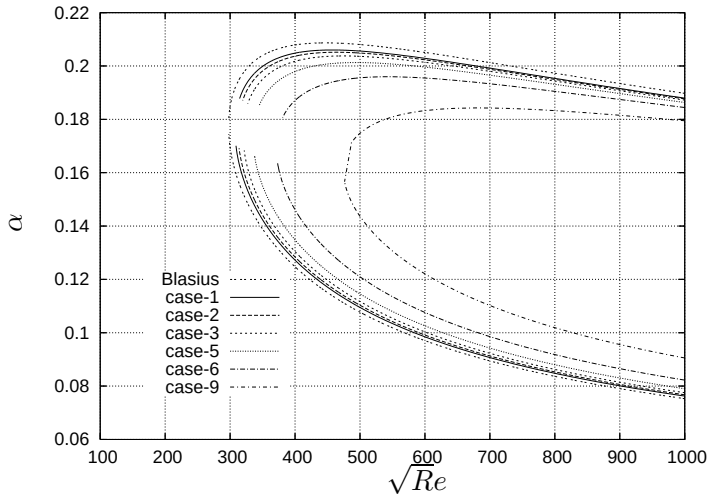

Figure 4.2: Neutral stability curves for the rotating flat plate case, in the plane $(\sqrt{Re_x}, \alpha)$ for the cases 1-3, 5-6 and 9

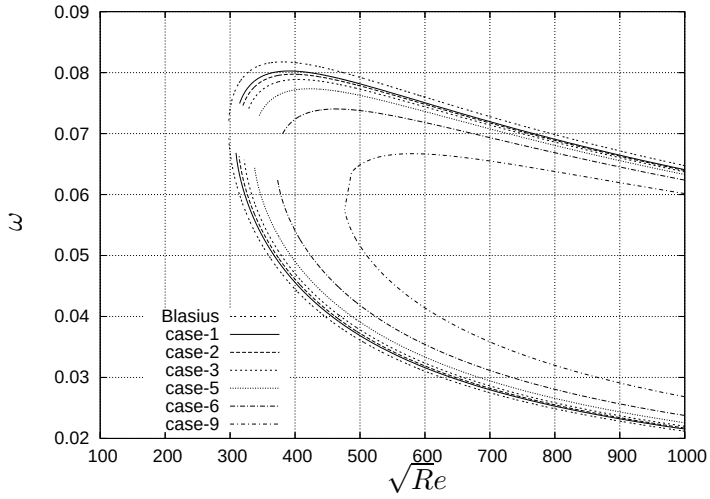

Figure 4.3: Neutral stability curves for the rotating flat plate case, in the plane $(\sqrt{Re_x}, \omega)$ for the cases 1-3, 5-6 and 9

The neutral stability curves are shown in figures (4.2) and (4.3). From

the plots in the planes $(\alpha, \sqrt{Re})$, $(\omega, \sqrt{Re})$, as the radial pressure gradient n increases the critical Reynolds number increases and the unstable area where $\alpha_i < 0$ decreases, the maximum dimensionless frequency decreases, as well as the coordinates (α_r, ω_r) of the tip of the neutral curve. As can be seen on the next table:

Table 4.1: Critical coordinates for a rotating flat plate

$Case$	Re_{cr}	α_r	ω_r
1	309.03	0.178945	0.070882
2	313.85	0.178129	0.070376
3	321.71	0.177088	0.069694
5	337.64	0.175747	0.068674
6	373.16	0.172097	0.066181
9	476.18	0.163935	0.060502

Looking at the Figures (3.8),(3.9) and (3.11) provides a good understanding of the stabilization effect of the rotation, can be seen that the unstable area decreases, when the n factor is calculated is clear that the growth of dimensional frequencies will be somehow below the expected for the Blasius (VP) as shown on Figure (3.10), this naturally is traduced in a lower n factor. Similar simulations can be obtain for the destabilizating case by inverting the direction of the Coriolis force for the calculation of (VP) for the rotating flat plate (RFP). The radial velocity profiles corresponding to the cases 1-9 from tables (2.2),(2.3) are ploted in figure (4.4), the position of the inflection point of the crossflow is set by the balance between the Coriolis and centrifugal forces. The magnitude will scale according to the radial pressure gradient n. The cases 4,7,8 does not appear due to the fact that they have identical properties in comparison with the cases 2,3 and 6 respectively.

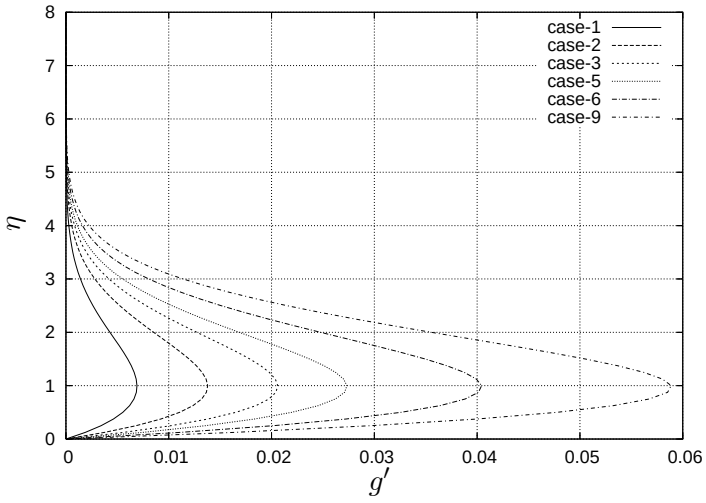

Figure 4.4: Radial velocity profiles rotating flat plate - cases 1-9

During the stability calculation the velocity profile corresponding to the given case was kept constant. In practice the pressure gradient will change according to the tangential position. The purpose is to show the method of developing a Database than can be used to include (RE). This results indicate the effect of rotation on the boundary layer, even when the propagation angle $\psi = 0$, a different solution from the Blasius stability curve is obtained.

4.10.1 Comparison with Simulations and Experiments

In the calculation of the mean flow b Chawla [23], the rotation number does not appear explicitly in the boundary layer equations. Instead the Blasius velocity profile was kept constant for all Reynolds number to obtain neutral stability curves. In contrast to the rotating blade, from the solution of the set of equations (on the laminar part) it is possible to observe an increase in the wall shear stress as the flow moves downstream, see section(2.7). The transition prediction was not considered, only the neutral response of the boundary layer. The obscure and mysterious unstable area was not studied at that time.
From Potter and Chawla [82] the following conclusions were obtained: for a constant β, increasing Ω^* (according to their reference system) has a destabilizing effect, whereas decreasing Ω^* has a stabilizing influence on the boundary layer. For a constant Ω^* increasing β has a destabilizing effect for positive values of Ω^* and a stabilizing effect for negative values of Ω^*.

From the experimental work done on a rotating wind tunnel Koyama et al. [53] it is found that the skin friction coefficients are modified by the effect of the rotation. According to their reference system, negative values of the

rotation number tend to increase the wall friction. The opposite behavior occurs for positive values. As the channel is rotated about an axis normal to the plane of the flow, the side rotating into the flow is destabilized whereas the flow on the side moving away from the flow is stabilized.

The Coriolis force acts as a favorable pressure gradient (stable side) on the upper part of the channel while on the lower side it tends to destabilize the flow by decreasing the pressure gradient (Unstable side). The advantage of the rotating channel is that secondary flow or crossflow is not present, as in the case on a rotating blade. However, it can be useful to estimate the effect of rotation on the Blasius velocity profile.

Flow visualization studies were made by Masuda and Matsubara [69] with the same experimental setup as Koyama. The conclusion from the flow visualization and computations is: For a negative rotation Figure (4.6) the Blasius flow experience transition by a spot formation similar to the non-rotating case Figure (4.5). The stabilizing effect of the Coriolis force tends to eradicate the origin of the spot formation by inhibiting the penetration of the free stream disturbance into the boundary layer, resulting in a decrease of the number and size of the spot with increasing the rotation number. The transition with positive a rotation Figure (4.7) is characterized by longitudinal streaks, their twisting up and breakdown to turbulence. The streak spacing decreases with increasing the rotation number and decreasing the Reynolds number. On this side the Coriolis force tends to intensify the longitudinal vortices already existed in the boundary layer by inducing the counter rotating vortices of the same direction as the original ones. For this reason, the transition of the high pressure side is governed by the enhanced streamwise vortices and their breakdown.

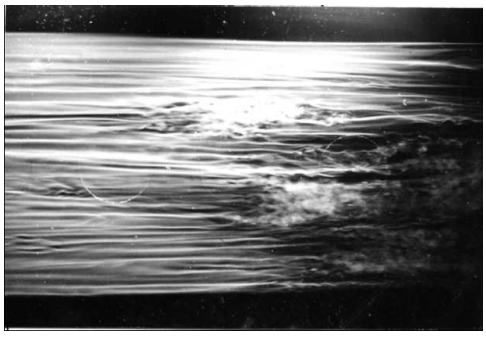

Figure 4.5: Natural Laminar-Turbulent transition visualization on a rotating channel -stationary case $U_w = 7m/s$ $\Omega = 0rad/s$ from [69] reproduced with permission

Figure 4.6: Natural Laminar-Turbulent transition visualization on a rotating channel $U_w = 6m/s\ \Omega = -5.0rad/s$ from [69] reproduced with permission

Figure 4.7: Natural Laminar-Turbulent transition visualization on a rotating channel $U_w = 7m/s\ \Omega = 5.9rad/s$ from [69] reproduced with permission

4.11 Effect of the Rotation number on the position of the critical point

To begin this analysis, from the Database of velocity profiles we select 6, cases corresponding to different rotation numbers in the range [0.5-1]. For the pressure gradient m=0, keeping constant the radial pressure gradient $n = 0.0750$, from the figure (4.8) is seen that as the parameter Ro decreases the critical Reynolds number increases. To explain this behavior we can make use of equation (2.15), for a given tip speed ratio λ. As the dimensionless radial position is increased, the rotation number increases, and the flow tends to the 2D solution where rotational effects are relatively small. However we have to consider that the edge value is different. The velocity profiles are plot in figure (4.9). Similar results have been obtained from Alfredsson and Persson [2] according to their respective dimensionless parameters.

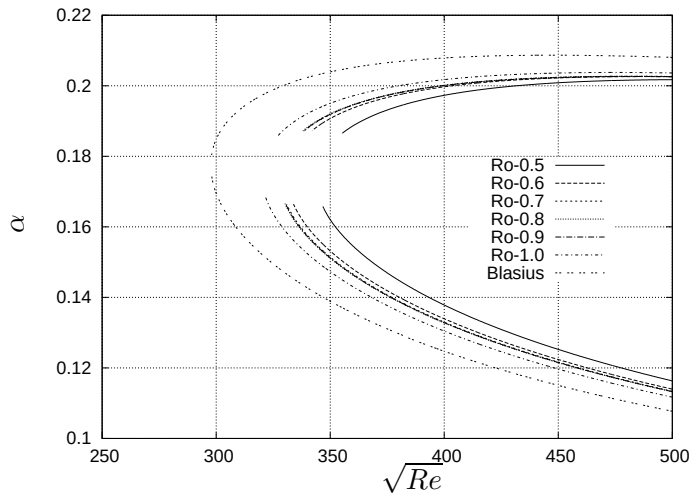

Figure 4.8: Neutral stability curves for different rotation numbers $Ro = 0.5 - 1.0$ in the plane $(\alpha, \sqrt{Re_x})$

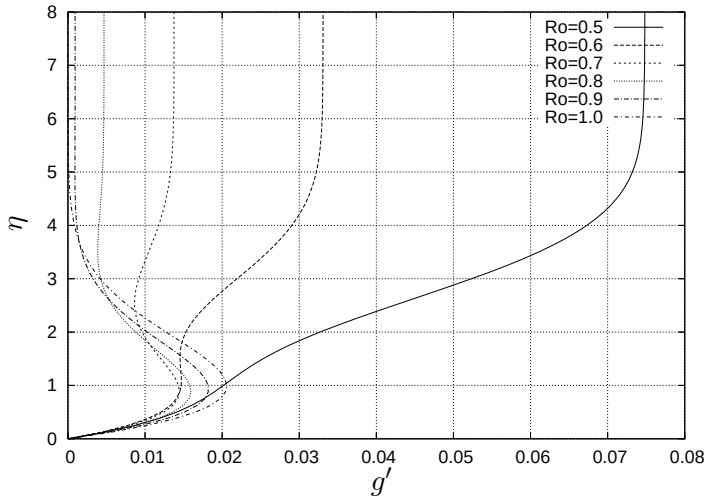

Figure 4.9: Radial velocity profiles for different values of Rotation number and constant radial pressure gradient n

The following table [4.11] summaries the properties of the chosen cases

Table 4.2: Boundary Layer properties for different Rotation numbers

Ro	$H_{\theta\theta}$	$H_{r\theta}$	$f''(0)$	$g''(0)$	ge'
0.50	2.563	1.103	0.33805	4.30268e-02	7.39173e-02
0.60	2.580	1.133	0.33584	3.94644e-02	3.28276e-02
0.70	2.584	1.236	0.33516	4.07379e-02	1.40562e-02
0.80	2.584	1.524	0.33499	4.36756e-02	5.15787e-03
0.90	2.584	1.990	0.33495	4.67147e-02	1.12335e-03
1.00	2.584	2.184	0.33496	4.97031e-02	7.58376e-04

4.12 Stability diagrams for adverse and favorable pressure gradient

The velocity profile close to the separation point was selected to observe the response to the rotational effect. From the considered cases, the response is similar like in the rotating flat plate cases. However, the (RE) is stronger as seen on the value of the critical Reynolds number and the corresponding neutral stability curves (4.10). As expected from the boundary layer analysis the (RE) on (VP) with a favorable pressure gradient are negligible, the results shown that the position of the critical Reynolds number is almost the same like the corresponding 2D solution. However the critical Reynolds number is slightly lower, as can be seen on figure (4.11), for this case it is found that rotational effects are destabilizating the flow, since m=1 is already the most stable pressure gradient at stagnation point.y

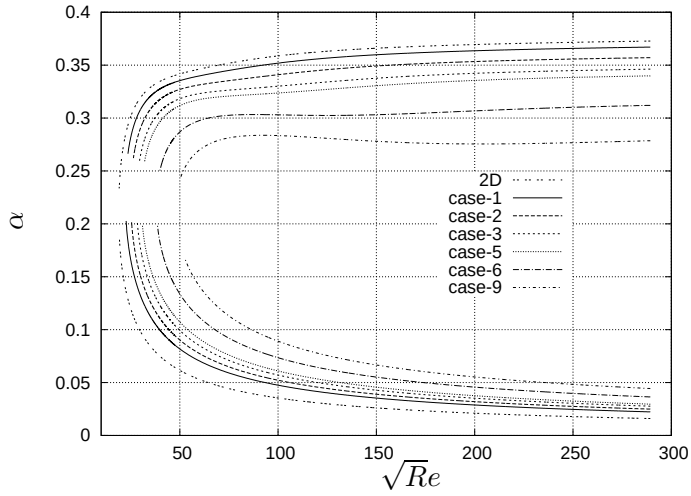

Figure 4.10: Neutral stability curves for the separation profile in the plane $(\sqrt{Re_x}, \alpha)$ with radial pressure gradients corresponding to cases 1-3, 5-6 and 9.

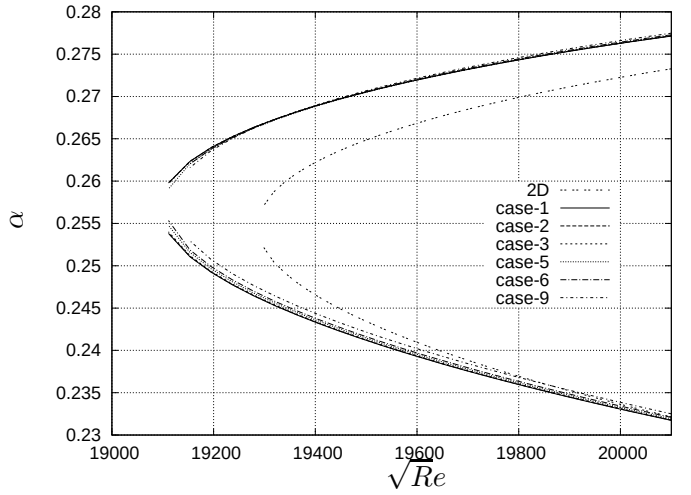

Figure 4.11: Neutral stability curves for the stagnation point, in the plane $\sqrt{Re_x}, \alpha$ with radial pressure gradients corresponding to cases 1-3, 5-6 and 9

4.13 Calculation of transtion on airfoils whit the effect of rotation

4.13.1 Potential flow approximation

The method to calculate the boundary layer is restricted to the approach used by Forgarty and Sears [32]. We are not considering the real 3D features of the flow and for transition prediction this is very important since the propagation direction plays a crucial role for the transition prediction. The important thing to notice is that the potential flow is only 2D, therefore $\psi_p = 0$, which may complicate a comparison, for instance with experiments. However, It is possible to study what is the response assuming some predefined variation of the potential flow angle ψ_p with the position on the blade x^*/c^*. In a real application this information for instance can be provided by a (NS) flow solver or a full 3D potential flow calculation.

4.13.2 Estimate of the potential flow direction

Prediction of the propagation direction on a rotating blade is in general a difficult task. More intricate than in other kinds of flow types, due to the complexity of the geometry, the inflow characteristics and the variation of the inflow angle according to the radial position. One possible approach to obtain an initial estimate is to look at the flow direction, at the edge of the boundary layer with an angle defined by equation 2.26. This condition is found by assuming that the shear stress distributions in both directions tend to zero as the edge of the boundary layer is approached and by the boundary conditions in the flow solver. The following expression can determine this angle, and involving the rotating parameters.

$$
\begin{aligned}
a &= n \\
b &= \frac{\xi}{\Delta\xi} + m \\
c &= \frac{\xi}{\Delta\xi} g'_e + sw \frac{c^*}{r^*} \xi \frac{2Ro}{U_{xf}} - \xi \frac{c^*}{r^*} - n \\
\beta_e &= \tan^{-1}\left(\frac{-b + \sqrt{b^2 - 4ac}}{2a} \right)
\end{aligned}
$$

Clearly the tangential pressure distribution m depends on a particular geometry and angle of attack, and to the 2D potential flow solution U_{xf}. The radial pressure gradient depends on the rotation number, local solidity and the dimensionless position on the blade ξ. The variable g'_e is taken from the solution of the previous mesh point. The sign function s_w was already described. If $\frac{c^*}{r^*} = 0$, $\beta = 0$. To illustrate the values of $m = 0$, $m = 1$

and $m = -0.0904$, Figures (4.12) - (4.14) show the propagation direction, assuming that the pressure gradient m is kept constant.

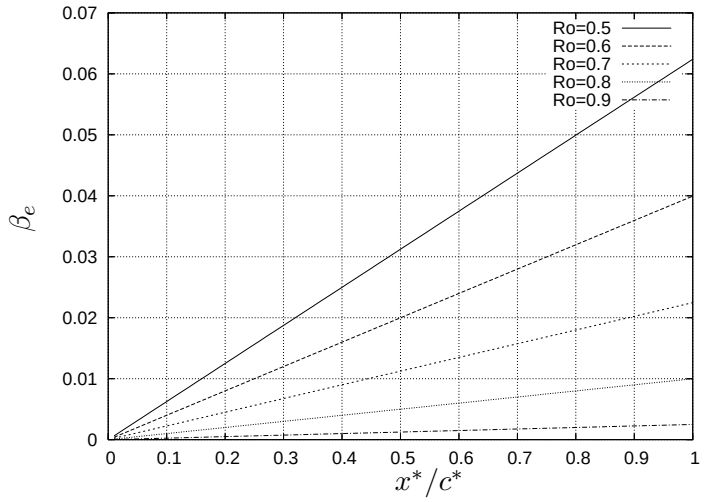

Figure 4.12: Variation of the edge angle for the case m=0 with parameters Ro=0.5-0.9 and $c^*/r^* = 0.25$

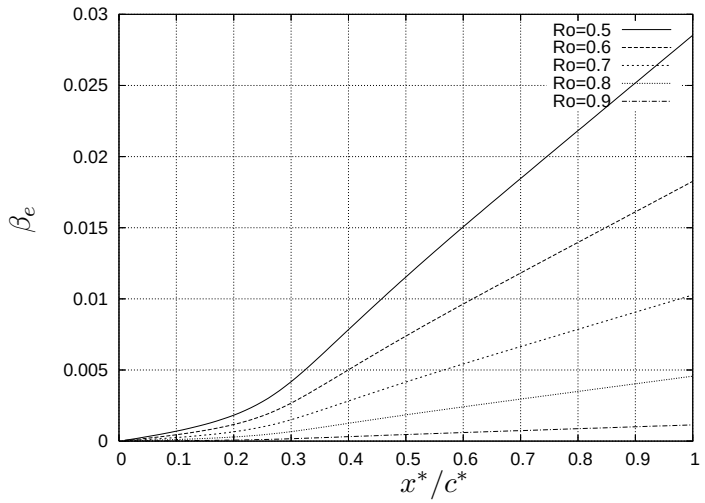

Figure 4.13: Variation of the edge angle for the case m=1.0 with parameters Ro=0.5-0.9 and $c^*/r^* = 0.25$

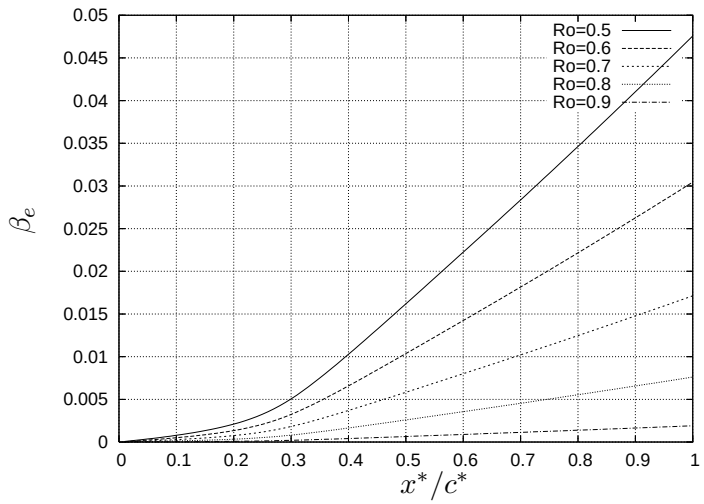

Figure 4.14: Variation of the edge angle for the case m=-0.0908 with parameters Ro=0.5-0.9 and $c^*/r^* = 0.25$

4.13.3 Critical Reynolds number for a given airfoil

To explain the response of the boundary layer at different Reynolds numbers and the effect of rotation in the stability diagrams, it is important to determine the shape of the neutral curve close to the R_{cr} value. The pressure gradients higher than the critical value m_{cr} for a given R_c will be stable, and therefore will not be able to amplify any frequency. The typical pressure distribution on an airfoil at one given position r^*/R^* will begin at the stagnation point where $m = 1$, and then, depending on the angle of attack, the pressure gradient will reach a maximum value close to the suction peak, and, as the flow moves downstream it will decrease until it reaches m=0. During this process the wall shear stress in the tangential direction $f''(0)$ will decrease and will continue to move to the negative pressure gradient zone. The value of $f''(0)$ where the first disturbances will be amplified is designated by f''_{cr}. The frequencies that promote transition will be located in a range from f''_{cr} to $f''(0) = 0.332$, the lower limit represents the skin friction coefficient on a flat plate. As R_c increases, the range will become wider, allowing more positive pressure gradients to be unstable. The tip of the neutral curve for the airfoil is clearly different, and is a function of the parameters that describe the rotating configuration, geometry, operational conditions as well as R_c. It was mentioned that the effect of Rotation number is to displace the tip of the neutral curve to a higher R_{cr}; the effect of the propagation angle ψ is to reduce the size of the unstable area, and increase R_{cr}, in a similar manner as the parameter c^*/r^*.

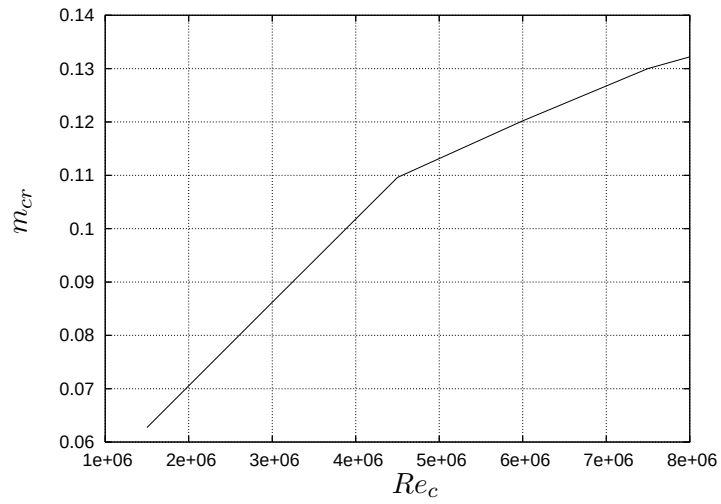

Figure 4.15: Variation of the critical tangential pressure gradient

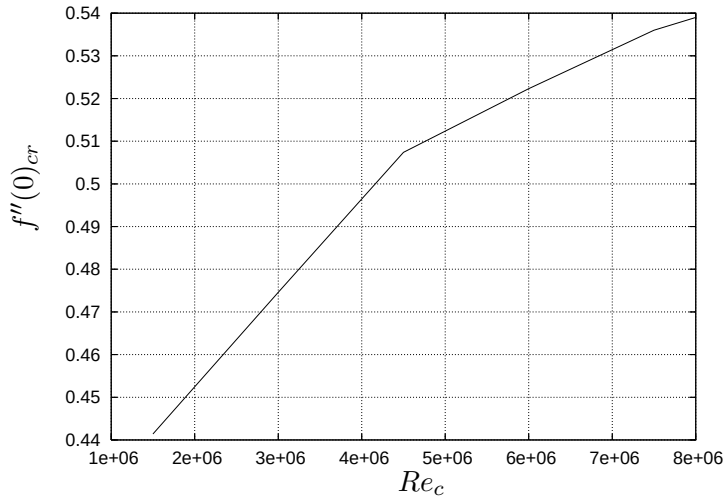

Figure 4.16: Variation of the critical wall shear stress - tangential direction

It is important to mention that the solution of the mean flow obtained with equations (2.13) and (2.14) is independent of the Reynolds number. However, for transition prediction it is required to specify this parameter. The maximum value of Reynolds number based on the chord that can be found on a wind turbine blade is close to $8X10^6$. The mean flow will be the same and will scale with Reynolds number. To have an overview of the tip shape of the neutral curve, the neutral curves for the m_{cr} values are shown in the following figure (4.17).

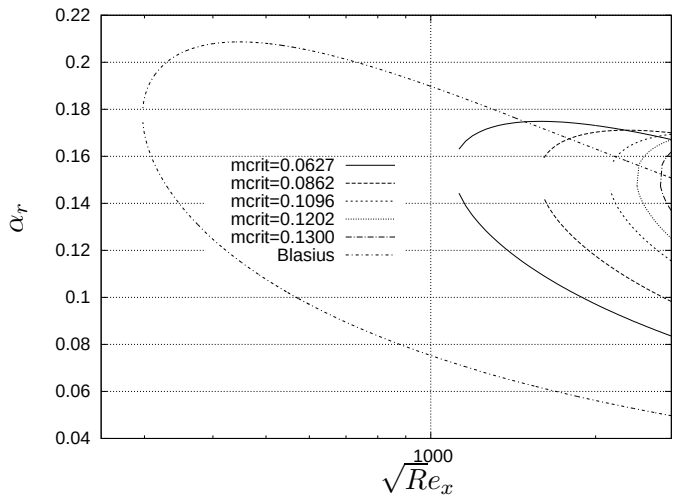

Figure 4.17: Neutral Stability curves for varying critical pressure gradient

Chapter 5

Transition prediction with rotation

5.1 Application cases

Very few transition experiments are available for an operating wind turbine blade. Some years a go, van Groenewoud et al. [38] presented the ECN-25 HAT machine, where the microphone arrangement was located at $r^*/R^* = 0.75$. Recently Madsen et al. [67] presented a series of experiments. For this configuration the microphones were located at $r^*/R^* = 0.925$. From the previous studies it is well known that rotational effects are stronger close to the inboard locations. The tendency is that, as the radius increases, the flow behaves similar to a 2D case. On the same blade pressure tabs were mounted at $r^*/R^* = 0.33, 0.93,$, and it is possible to estimate the transition location by carefully examing the results. However, is not possible to identify what is the critical frequency that promotes transition. Due to the difficulty to obtain experimental data at varying operational conditions and locations on the blade, it is proposed to extend the results at inboard locations. In a similar manner it is suggested to make a parametrical study of wind turbine profiles at different operational conditions. For comparison with experiments it is required to calculate the angle of attack. This is not a simple task. Recently some improvements have been made by Shen et al. [103], Hua et al. [45], which however demands access to experimental data. It is mandatory to know Reynolds number based on chord length, as well as the rotation number. Both parameters depend on the relative velocity, which is a function of the tangential and radial induction factors. In the absence of an improved (BEM) method, this parameters will be estimated with the classical (BEM) theory without rotational effects. In a similar manner the angle of attack needs to be estimated to obtain the pressure distribution that matches the true pressure distribution on the airfoil section. The true transition position will demand an iterative process where

the rotational effects are included. What is shown in the next section is a parametrical study to estimate the effect of the parameters that involve rotation. Finally, it provides the extension of the results to the inboard locations on the pressure and suction side of the blade for the NM80 rotor. The section 21 where the experiments were made, makes use of the angle of attack reported in the work of Madsen et al. [67]. The rest is calculated with the classical (BEM) method and the experimental curves in Abbott and Doenhoff [1] corresponding to the respective radial locations.

5.2 Parametrical Analysis

To be able to study the effect of rotation on a wind turbine blade, different airfoils were used. The DU-91-W2-250 can describe the inboard part of the blade, the NACA 63-415 can account for the middle part and the NACA-0015 for the tip region. The simulations were made at four different Reynolds numbers, ranging from 1.5 to 6.0 million, the local solidity was set to $c^*/r^* = 0.1, 0.2, 0.3$ on the suction and the pressure side. To simplify the solution, the rotation number was fixed to Ro=1. The technique used to evaluate the effect of the propagation direction of the disturbance angle ψ, according to figure 4.1, was essentially fixing the propagation direction and setting the imaginary part of the spanwise wave number $\tan(\psi_{gr})$ equal to zero. This procedure was repeated for different propagation angles, it turn out that for parametrical study is more convenient to define a range between [0-1] therefore, the dimensionless parameter γ is defined as $\gamma = tan(\psi)$. This technique resembles the well known beta method or (envelope of envelopes method) developed by Arnal. One drawback is that when the envelope of all the curves is calculated, it is possible to obtain a N factor lower than 9. In some typical cases close to 6, this is referred as a pathological case. The reader must be aware that the precise transition location will not be found, because it will requires a calibration or comparison with experimental data. At the moment they are not available, however, some results have been obtained on the blade section 21 on the NM80 rotor, although the present parametrical study at different conditions will help to understand the effect of rotation on the transition location. Assuming that transition will still occur when the N factor reaches the common value of 9, the following response is observed, this criteria will be the same for all the operational conditions and airfoils, (Simulations are not restricted to this specific value and can be modified).

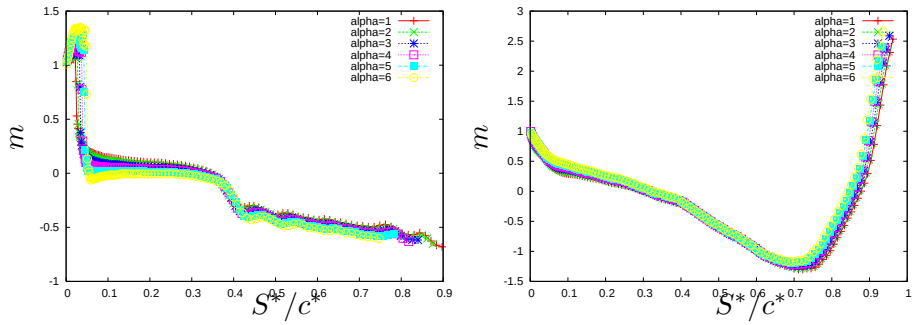

Figure 5.1: Dimensionless pressure distribution on a DU-91-W2-250 airfoil, left figure: suction side, right figure: pressure side

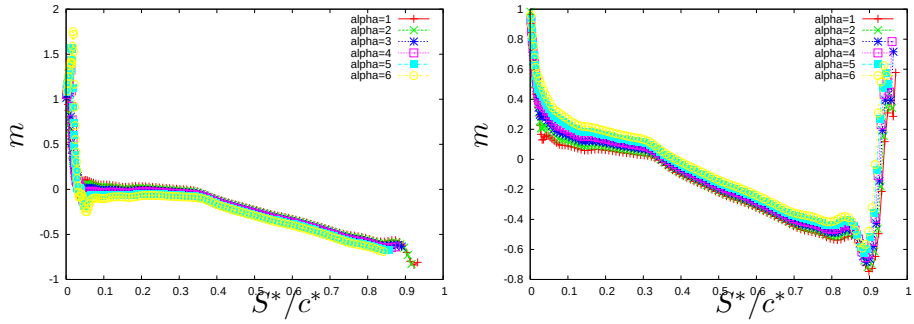

Figure 5.2: Dimensionless pressure distribution on a NACA-63-415 airfoil, left figure: suction side, right figure: pressure side

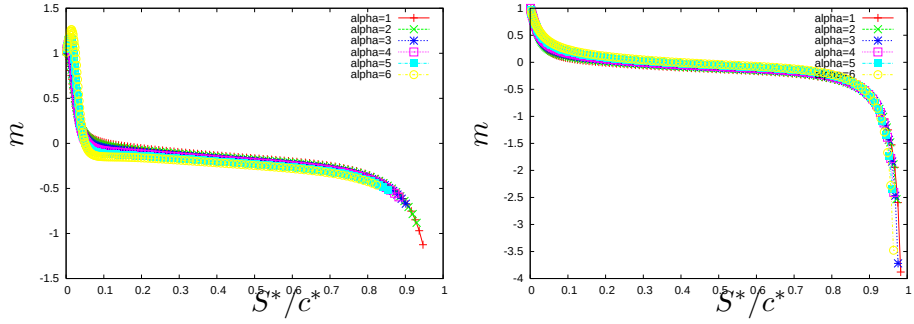

Figure 5.3: Dimensionless pressure distribution on NACA-0015 airfoil, left figure:suction, side right figure:pressure side

The first thing to look at is the pressure distribution at different angles of attack for the considered airfoils, on both the pressure and suction side.

The curves shown in figures (5.1),(5.2),(5.3) begin at the stagnation point of the blade, after which they passes the suction peak and gradually the pressure gradient will be reduced until the negative zone. Furthermore, the relation between the wall shear stress on the radial and tangential directions are shown in figures (5.4),(5.5),(5.6) where the value of the wall shear stress at the stagnation point is 1.23259, increasing by a small amount on the suction peak and then maintaining a constant value until the negative pressure gradient zone is reached. The response on the pressure side is different in the sense that, in comparison with the suction side, a relatively high amount of the surface is laminar, and the rotational effects have sufficient distance to develop on the blade. The same behavior is observed for $c/r = 0.2, 0.3$, and the curves will scale according to the magnitude of the radial pressure gradient.

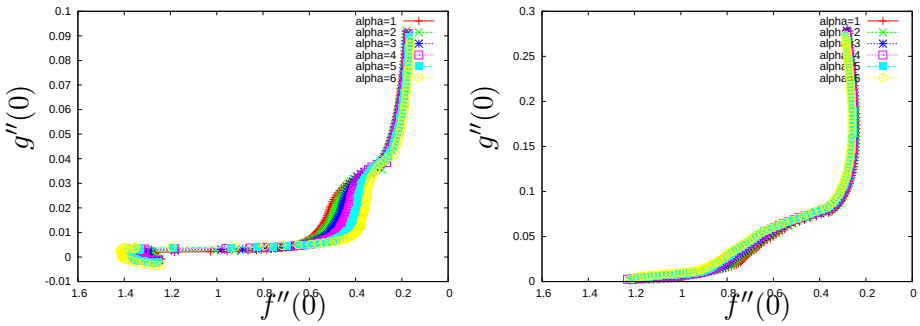

Figure 5.4: Wall shear stress ratio on a DU-91-W2-250 airfoil left figure: suction side , right figure: pressure side

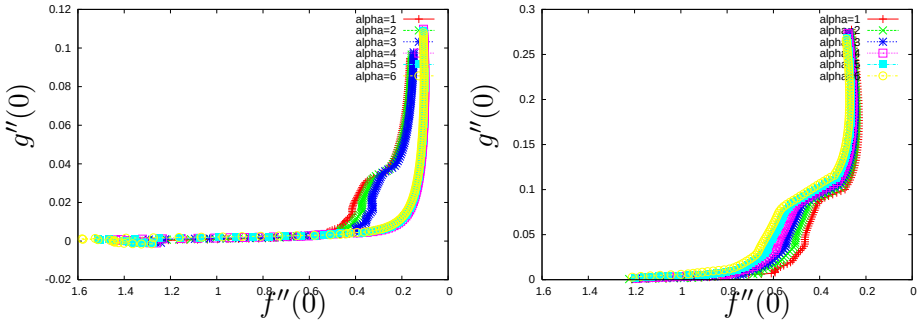

Figure 5.5: Wall shear stress ratio on a NACA-63-415 airfoil left figure: suction side, right figure:pressure side

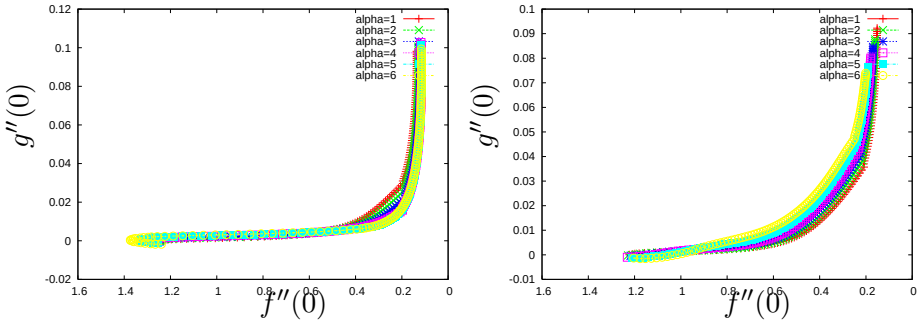

Figure 5.6: Wall shear stress ratio on a NACA-0015 airfoil left figure: suction side, right figure: pressure side

5.2.1 Effect of the angle of attack

The figures (5.7) (5.8) and (5.9) shows the effect of different parameters on the position of the transition location S^*_{tr}/c^* on the considered airfoils: on the horizontal axis is shown the variation of the angle of attack α_0 as a function of Re_c and c^*/r^*. This somehow make difficult to interpretate the figures because the effect of two parameters is presented. To start with the discussion it is assumed that the propagation angle is zero $\psi = 0$ for the suction and pressure side, (will be shown later that the propagation angle is another parameter that is needed to take into consideration). The continueous lines represent the 2D solution for Re_c 1.5 , 3.0 , 4.5 and 6.0 million, that is used a a reference to study the effect of the considered parameters. The points represents the combined effect of Re and c^*/r^* whit values 0.1, 0.2 and 0.3. One conclusion from the analysis it is that as the R_{ec} increases (on both the pressure and suction side), the effect of c^*/r^* decreases, the dispersion on the points at a given angle of attack tend to decrease. It is some how evident that if $c^*/r^* = 0$ all the point will be located on the corresponding 2D reference. It is interesting to notice that even when the propagation angle is zero by comparing the suction and pressure side is possible to observe the strong effect of rotation on the pressure side. This is due to the fact that rotational effects have sufficient time to develop on the surface. In contrast, on the suction side, the solution shown is very similar to the corresponding 2D case. As the angle of attack increases, the transition point is displaced towards the leading edge, where a relative small amount of the surface is laminar, however the location is given also in combination with the propagation angle ψ.

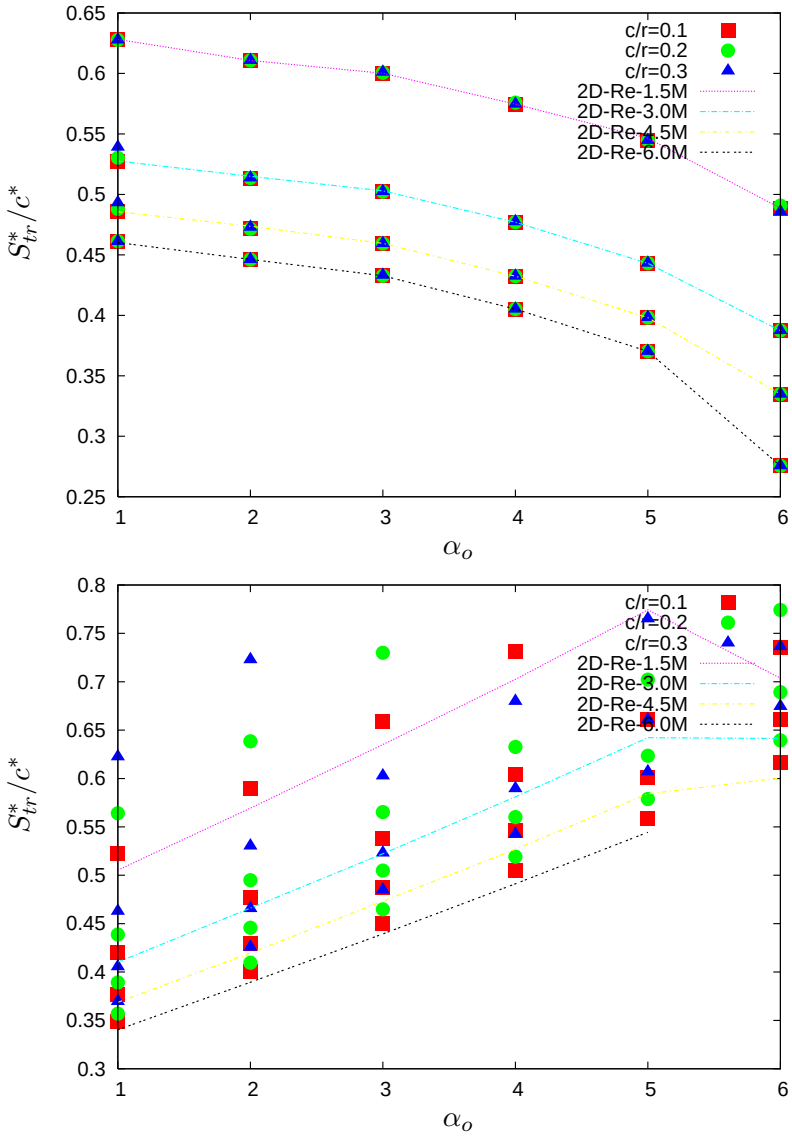

Figure 5.7: Transition location for $\gamma = 0$, upper figure: suction side, lower figure: pressure side, on a DU-91-W2-250 airfoil

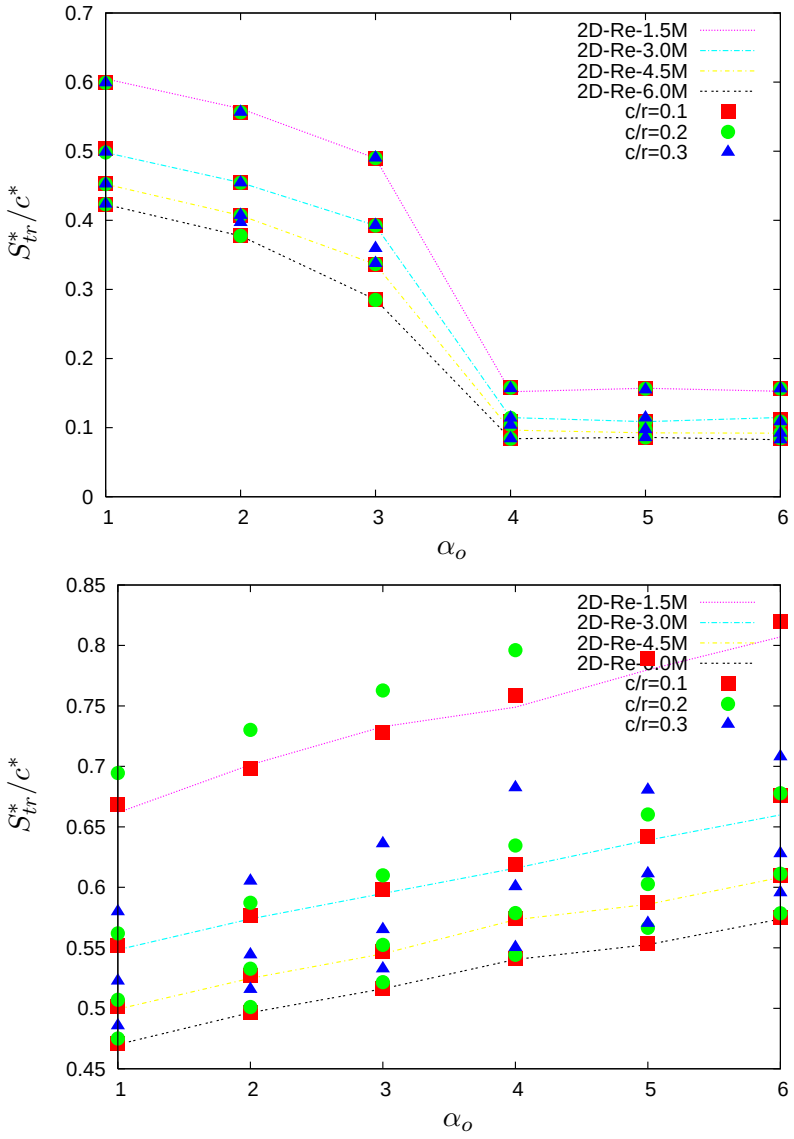

Figure 5.8: Transition location for $\gamma = 0$, upper figure: suction side, lower figure: pressure side, NACA-63-415 airfoil

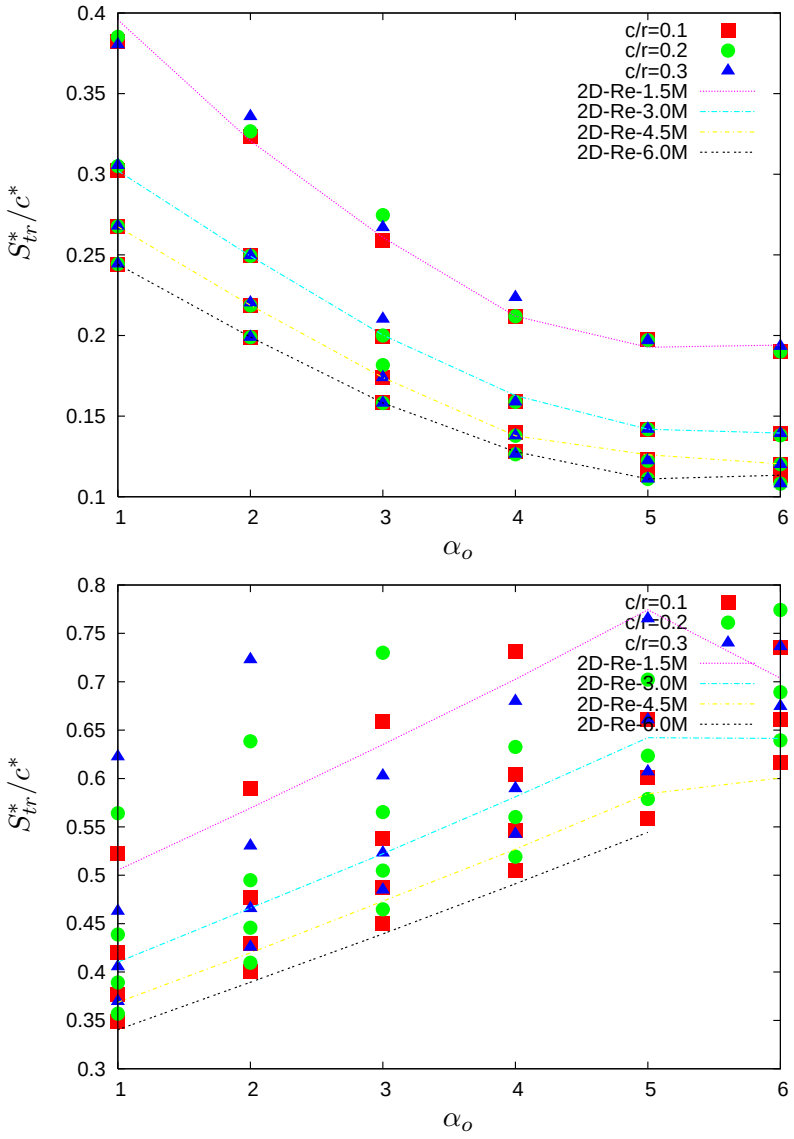

Figure 5.9: Transition location for $\gamma = 0$, upper figure: suction side, lower figure: pressure side, NACA-0015 airfoil

The figures (5.10)-(5.12) extend the results of the previous figures for a different propagation angle, in this case $\gamma = 0.2$. As this parameter increases the dispersion on the points becomes more evident in both surfaces of the airfoil. On the suction side at higher angles of attack the effect of ψ tends to decrease. For high Reynolds numbers the effect decreases. On the pressure side as α_0 increases the rotational effects also increase and the combined effect of ψ makes the deviation of the points more evident.

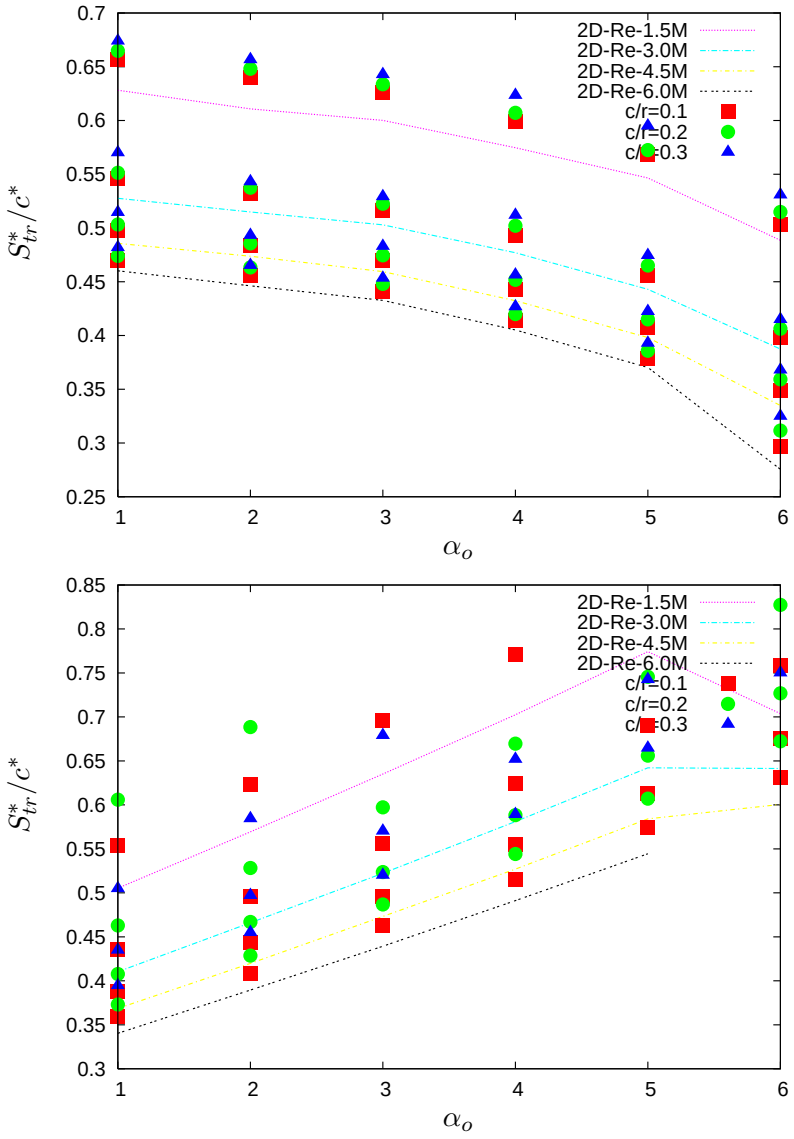

Figure 5.10: Transition location for $\gamma = 0.2$, upper figure: suction side, lower figure: pressure side, on a DU-91-W2-250 airfoil

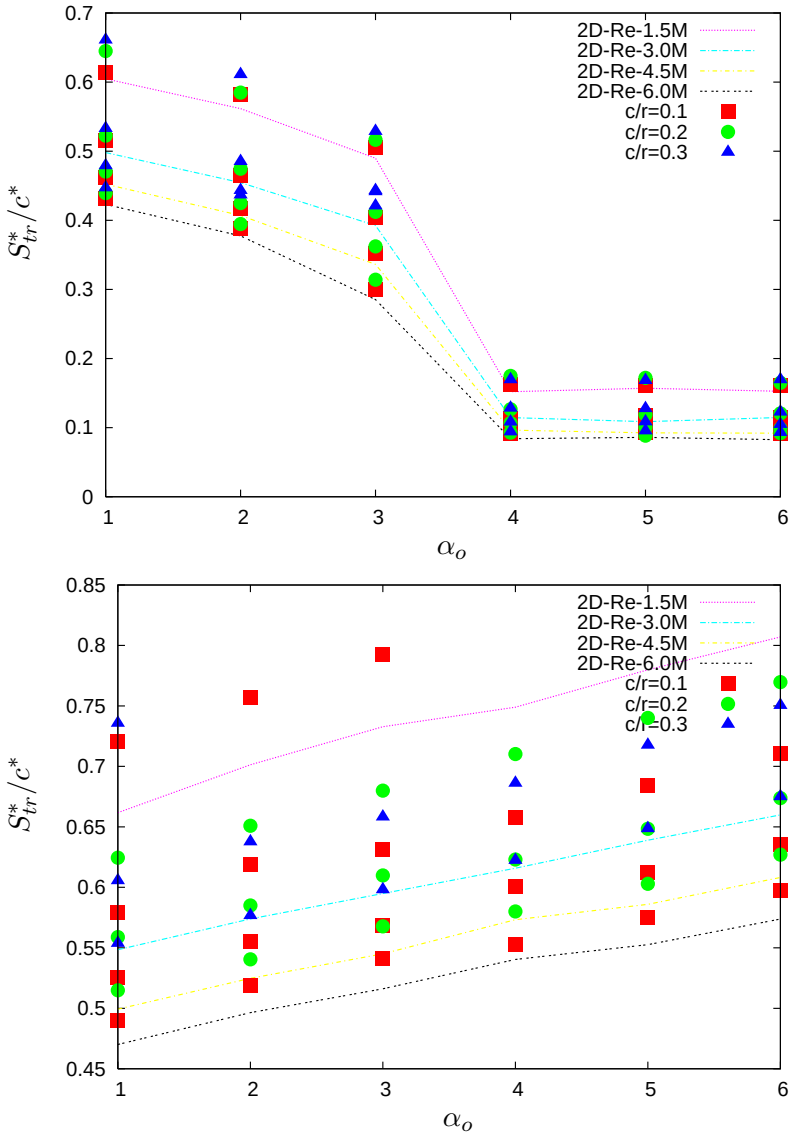

Figure 5.11: Transition location for $\gamma = 0.2$, upper figure: suction side, lower figure: pressure side, on a NACA-63-415 airfoil

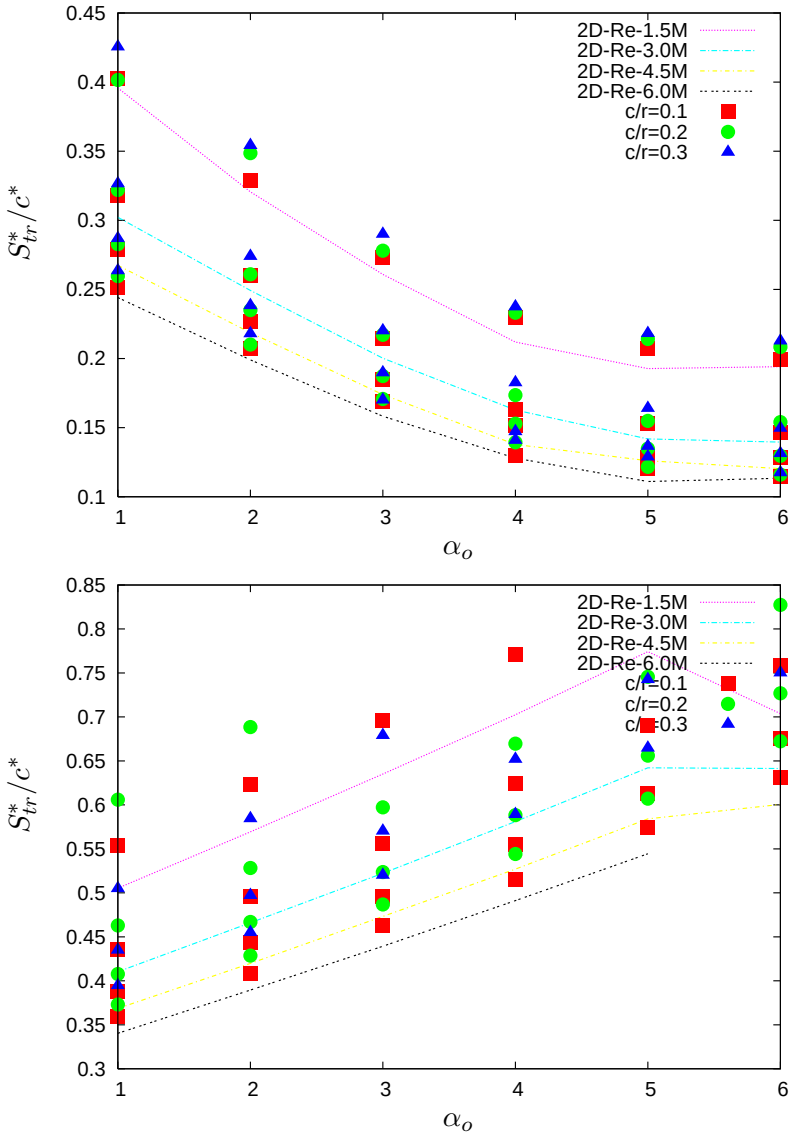

Figure 5.12: Transition location for $\gamma = 0.2$, upper figure: suction side, lower figure: pressure side, on a NACA-0015 airfoil

5.2.2 Effect of the propagation angle

To study the effect of the propagation angle, in the figures (5.13),(5.14) and (5.15) the horizontal axis is replaced by the propagation angle, for a constant angle of attack, $\alpha_0 = 1$. It is some how convenient to parametrize the solution, for that pourpose γ is defined as $\gamma = tan(\psi)$. Following a similar interpretation as the previous section the following conclusions are

obtained:

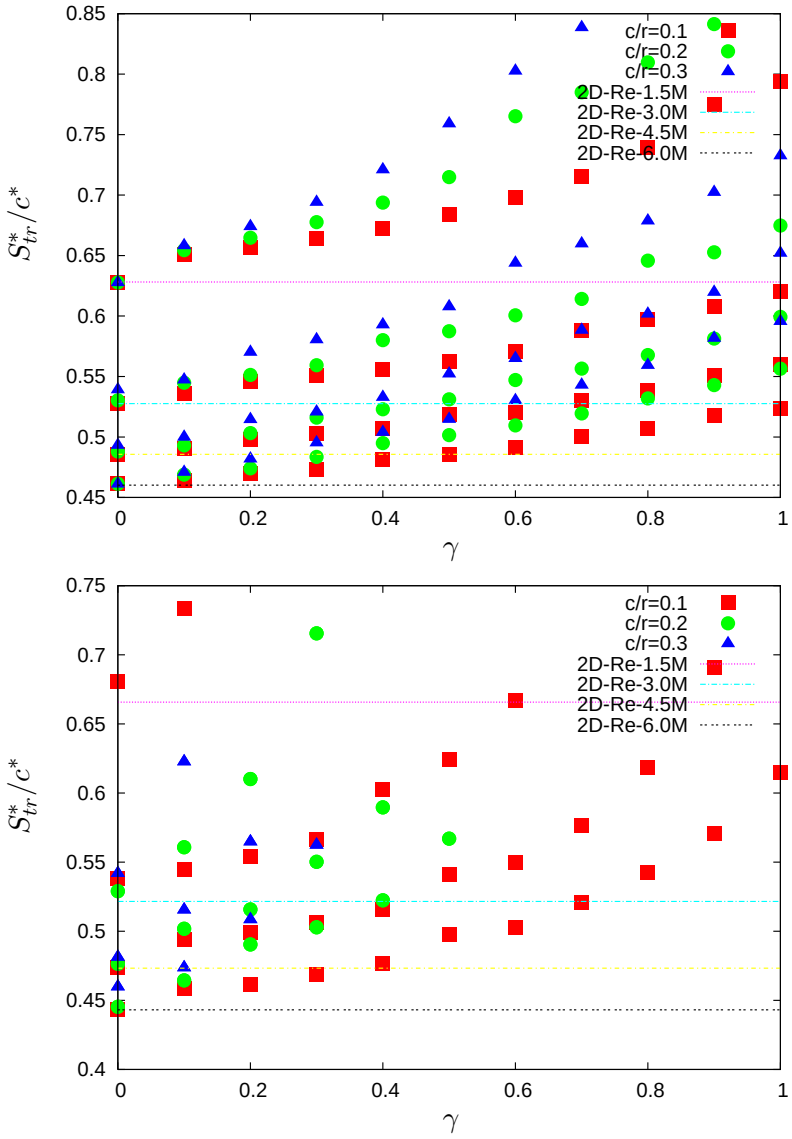

Figure 5.13: Transition location for $\alpha_0 = 1$, upper figure: suction side, $\alpha_0 = 2$ lower figure: pressure side, on a DU-91-W2-250 airfoil

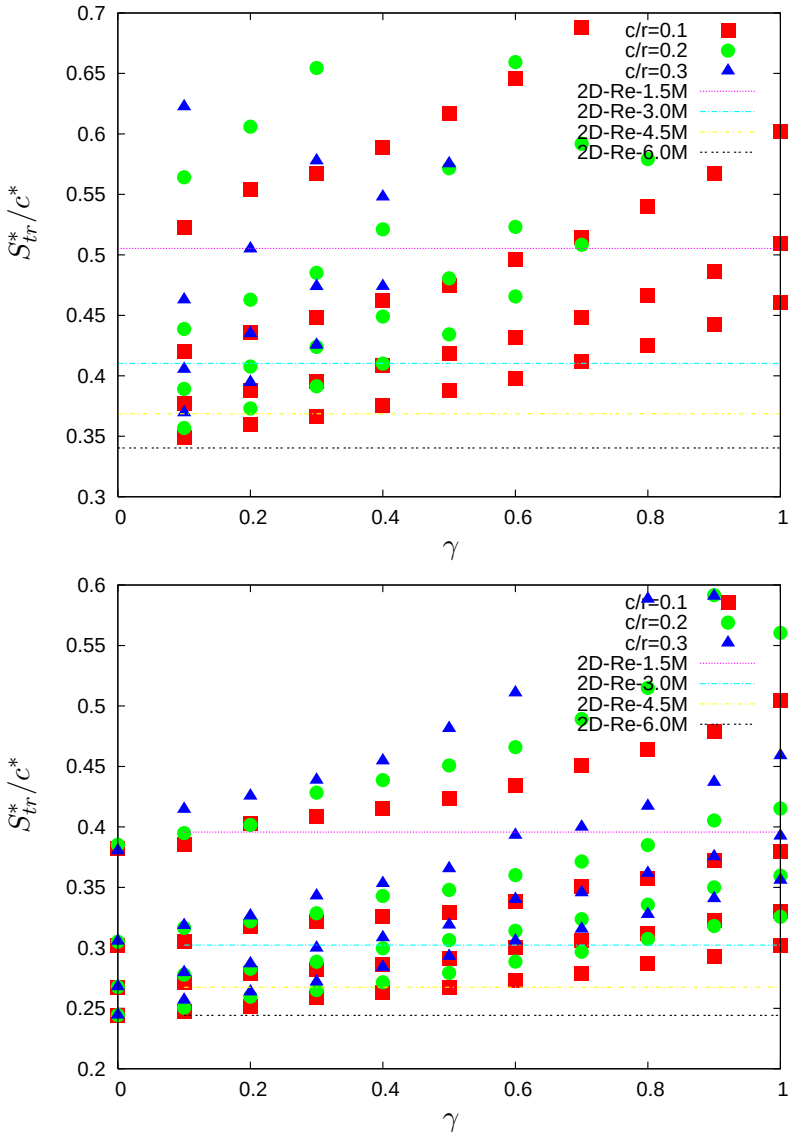

Figure 5.14: Transition location for $\alpha_0 = 1$, upper figure: suction side, lower figure: pressure side, on a NACA-63-415 airfoil

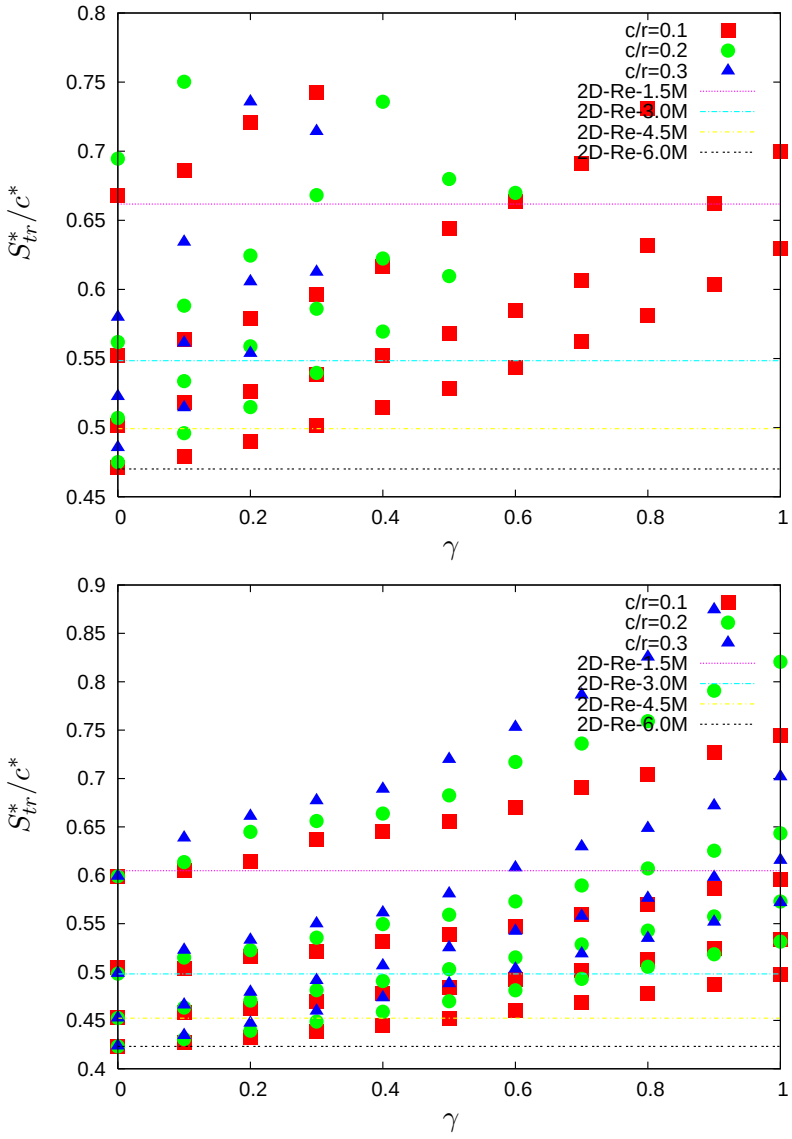

Figure 5.15: Transition location for $\alpha_0 = 1$, upper figure: suction side, lower figure: pressure side, on a NACA-0015 airfoil

As the Reynolds number increases the effect of c^*/r^* is smaller. The curves made at different propagation angles ψ tend to diminish. Looking also at $\gamma = 0$ is possible to see the combined effect of the Reynolds number and the local solidity c^*/r^*. As Re increases the dispersion on the points becomes narrow. In a similar way is possible to fix another γ value and draw a vertical line. Different airfoils respond in a different manner, which has to do with the pressure distribution in the tangential direction. All the

airfoils have the same radial pressure gradient. By careful examination of the pressure distribution, the difference in the response of the airfoil is in the way that the energy is extracted from the incoming wind. Here it is pertinent to mention that two process take place: the extraction of energy from the flow and the transition process. From the analysis of the individual response of the pressure gradient to rotation it was concluded that rotational effects play a major role from zero to the adverse pressure gradient zone. If the slope of the curve from the suction peak is higher, the boundary layer can not respond as expected. However, if the curve changes gradually, it has the time to develop the rotational effect, which explains the different behavior on the selected airfoils.

The effect of increasing the Reynolds number for a given airfoil and angle of attack is to displace the transition point towards the leading edge. In a similar manner, keeping constant Re and increasing α_0, the transition point moves towards the leading edge. The combined effect of the two parameters has a stronger influence. Rotational effects are only fell on the blade surface, and it takes some distance from the attachment line to the transition location to develop this body forces. In practice, only a small portion of the blade is laminar. In the negative pressure zone, rotational effects have a stronger influence on the stability of the boundary layer. However this is what normally occurs on the suction side of the blade. On the pressure side in contrast relatively high part is laminar due to the high favorable pressure gradient zone. This can change for example the characteristic of the laminar separation bubble close to the trailing edge. This is known to be connected with the noise trailing edge production on the blade Fischer et al. [31].

5.3 NM80 rotor analysis

By careful examination of the results presented by Madsen et al. [67], it is possible to see that the corresponding critical frequency is similar to that found with the 2D version of the stability code. This holds true for wind tunnel experiments, where, by means of a turbulence grid, the turbulence level was intensified up to 3%. Looking at the comparison made between the rotor and the wind tunnel experiments it is possible to see that the critical frequency for the wind tunnel with the turbulence grid is close to 6.2 kHz for the positions s/c^*=0.006, 0.023, 0.047 and 0.138, while the frequency found from the stability code at the specified operational conditions is 5.387KHz. This indicates that even when the turbulence level is higher the frequency that promotes transition is similar to the one found in the 2D code. This result is attractive, because it creates a possibility to calibrate the N factor according to turbulence level. The frequency peak at 2kHz was not found from the stability analysis on the clean airfoil. The frequency reported for the rotor is close to 8kHz, and was not found in the stability code with ro-

tational effects. The expected critical frequency is 5kHz. The difference can be attributed to the tip effect in the boundary layer, that on the suction side is acting as an adverse pressure gradient. Decreasing the critical Reynolds number for those particular operational conditions, allows higher frequencies to be amplified. However, this statement needs to be formally proved. The present model is restricted, since this effects are not taken into consideration when solving the boundary layer equations. However, it is possible to model the tip effect but it is out of the scope of this report and can provide in the future a tip effect study as suggested on Shen et al. [102]. An alternative explanation can be formulated by looking at the reference system of figure 2.1 and section 2.3.3. It was shown that the rotational effects have a negative influence from the local stagnation point (LSP) (at some defined radial position) to the rotor plane of the airfoil on region I. This can explain why the frequency peak is displaced to a higher value. It is evident that this effect can not be captured by the wind tunnel, and makes it complicated to compare results. Similar measurements where made with the ECN 25 HAT wind turbine. In this particular case, microphones arrangements were placed at a position of $r^*/R^* = 0.75$ that is more suitable for transition measurements. Due to the fact that it is away from the tip, it is clear that this experiment was not concerned with the noise modeling. The reader is refered to van Groenewoud et al. [38] for more details.

5.3.1 Extension of results to the inboard locations

The present results shows the transition location from blade section 8 to blade section 18 on the pressure and suction side at 10m/s. It also includes blade section 21 where the measurements were made. From the experiments carried out by Madsen et al. [67] the microphone arrangement was mounted on the outboard part of the blade where the flow behaves like a 2D flow but still with some rotational effects as seen on the local solidity c^*/r^* distribution. However it is of interest to observe the effect of rotation close to the inboard locations where (RE) are stronger.

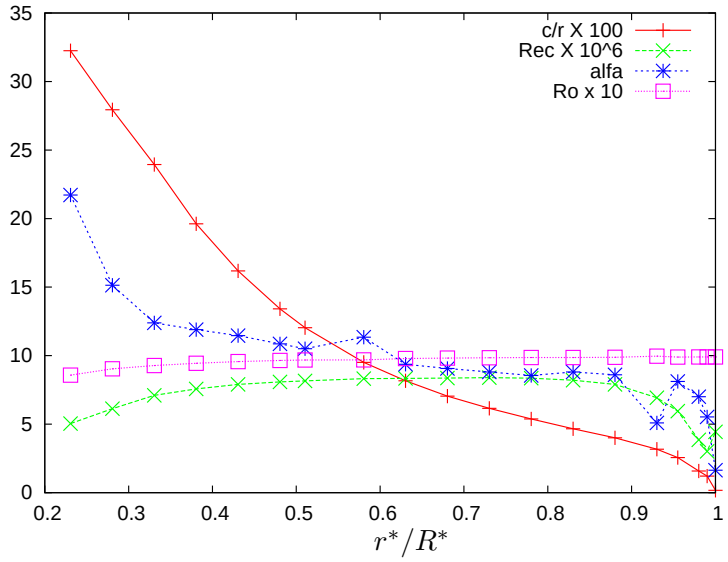

Figure 5.16: Parameters used on the solution of the stability problem on the NM80 rotor

Figure (5.16) show the input parameters for boundary layer and stability computations. It is seen that the angle of attack decreases from $r^*/R^* = 0.2$ to 1.0, the Reynolds number increases until the maximum value at $r^*/R^* = 0.73$ of about 8.4 million, then gradually decreases to 3 million at $r^*/R^* = 0.99$. On both surfaces the local solidity c^*/r^* decreases according to curve. The rotation number Ro is varying slightly from $r^*/R^* = 0.12$ where the value is $Ro = 0.92$ to $r^*/R^* = 0.98$ where $Ro = 0.99$

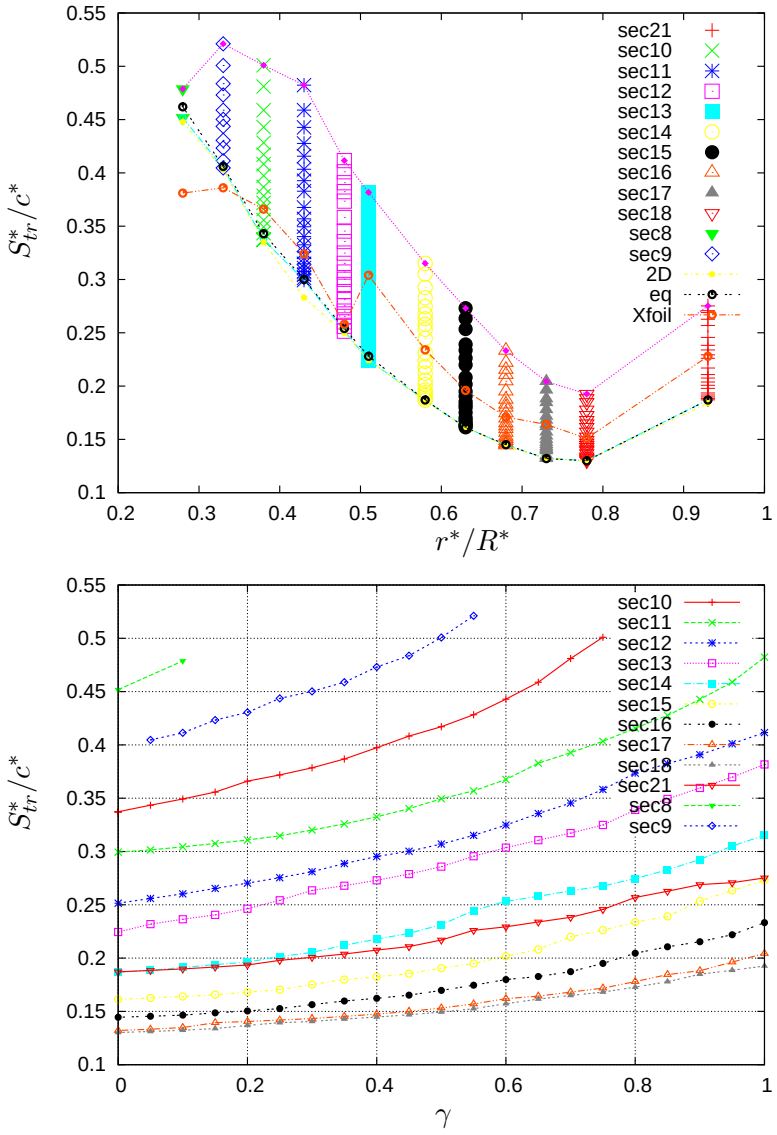

Figure 5.17: Transition computations on the NM80 rotor - suction side

From the stability results on the suction side shown in figure (5.17) it is seen that rotational effects play a minor role at $r^*/R^* = 0.75$. It is seen that the effect of the propagation angle γ decreases as the dimensionless radial position r^*/R^* increases. Close to the tip region the effect of rotation falls off. On figure (5.17) it is shown the effect of the propagation angle γ on the transition location, the position is not much changed for the blade sections close to the tip of the rotor, however is important to look at the Reynolds number and the angle of attack, in a similar fashion like in the parametrical

study.

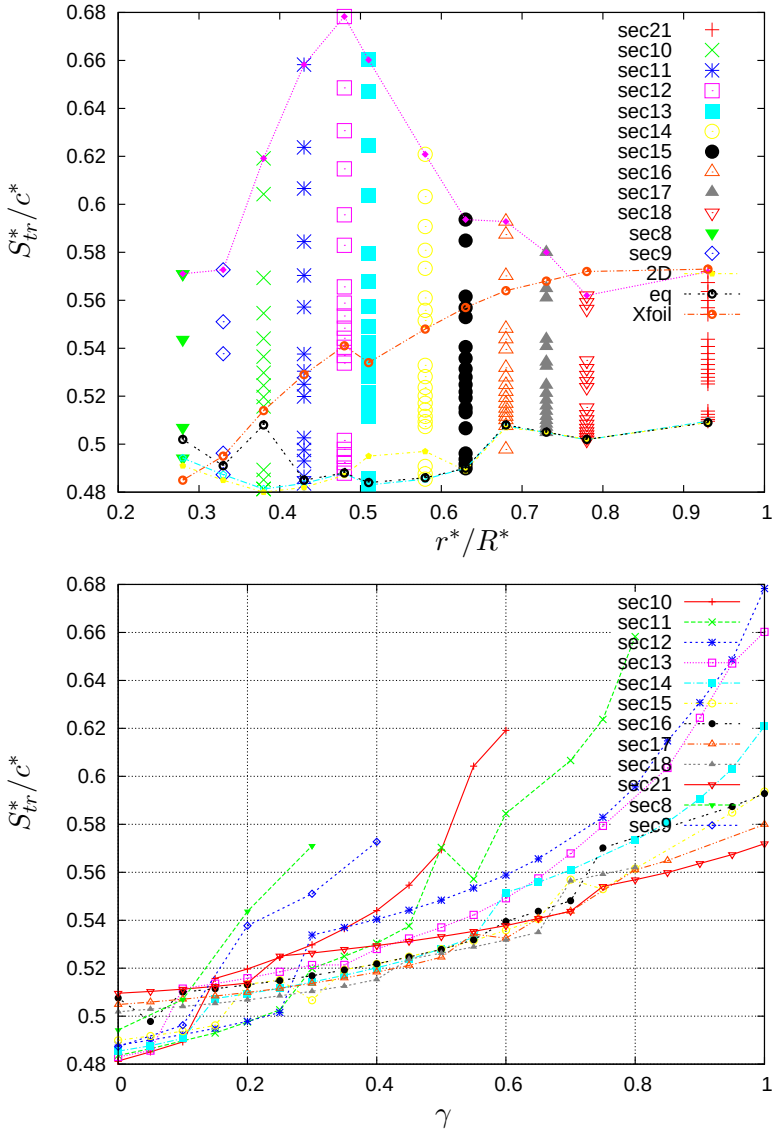

Figure 5.18: Transition computations on the NM80 rotor - pressure side

As was anticipated from the parametrical analysis rotational effect have strong stabilizating effect on the pressure side. Taking as a basis the parametrical study, the results from the full rotor can be interpreted as follows: Looking at figure 5.18 it is seen that rotational effects play a minor role at $r^*/R^* = 0.75$. (This was also observed on the suction side). The way to interpret the results is to calculate the lenght of the transition area for a

selected blade section. Between the upper and lower bands different cases corresponding to different values of ψ are represented by points. To explain the width of the transition zone is needed to see the distribution of c^*/r^* and α_0 along the blade, on the pressure side as c^*/r^* increase and α_0 increases the band area becomes wider. looking at figure (5.16) is clear that high angles of attack are found at the inboard sections of the rotor, in a similar manner the local solidity c^*/r^* has also relatively high values. On the suction side as α_0 inreases the band width becomes narrow, even whit the favorable effect of c^*/r^*, therefore the (RE) have not sufficient time to act on the flow and the growth of unstable frequencies is not to much affected. It is important to mention that the Reynolds number is not a very sensible parameter, of course has influence but not as c^*/r^* or α_0 . Re_c does not change the size of the unstable area in the stability diagram like the one shown, for instance on (3.8)-(3.11), simply change the range of frequencies. The rotation number Ro in a similar manner has not to much influence, it is well known that will stabilize the unstable region by reducing the size as Ro tends to 1 as can be seen on figure (4.8). As the value of ψ increases the transition location is displaced to a higher value by reducing the size of the unstable area.

The figure (5.20) show the critical frequencies that promotes to transition at different blade sections, on the suction and pressure side. To observe the critical frequencies along the radious of the blade for the suction and pressure side the following figure (5.19) is used:

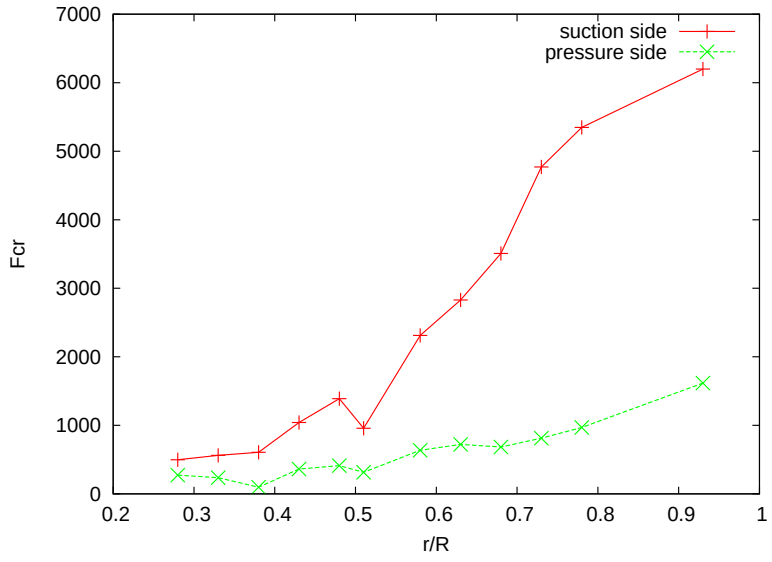

Figure 5.19: Critical frequencies on the NM80 rotor

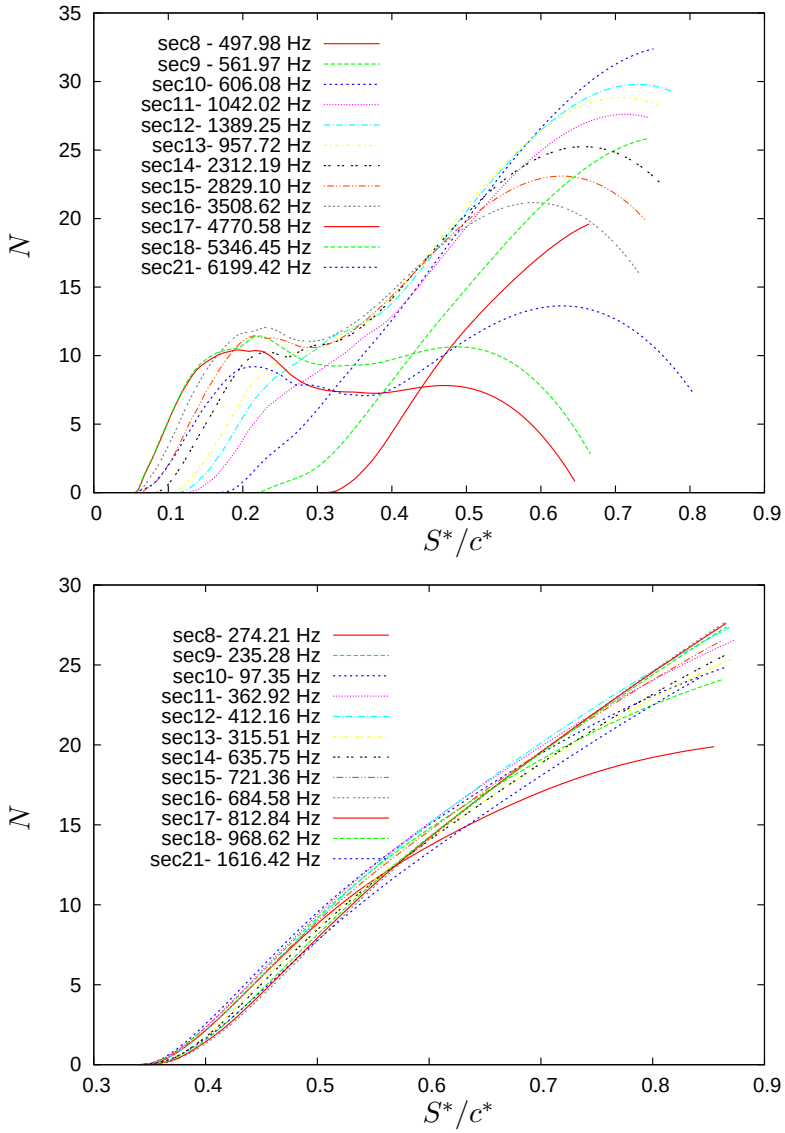

Figure 5.20: Critical frequency on the: a) Suction side , b) Pressure side on the NM80 rotor

Chapter 6

Conclusions

During the development of this project, rotational effects have been included on the calculation of the mean flow throught a similarity variable transformation technique. The boundary layer equations, and its solution have been adapted to a wind turbine blade. The range of parameters with rotational effects have been properly defined. By analysis of the solution for the defined parameters range, the velocity profiles inluding the crossflow have been mapped and store on a Database. The size have been reduced by carefull analysis of input and output parameters for the solution of system of (PDE). A relative old problem regarding to the boundary condition have been solved and adapted to a real wind turbine blade. The other important contribution is that rotational effects have been included directly in the stability equations, and was one of the key and relevant question that have been effectively answer during this project. Special care and effort were given to obtain an appropiate boundary condition to solve the eigenvalue problem, more specifically to performe linear stability computations with (RE). The way to obtain a solution was to basicly selecting very simple cases and the gradually increasing the level of complexity to include more characteristics of the flow and geometry. With that pourpose on mind, the rotating flat plate have provided light a good understanding on the effect of rotation into the stability of the boundary layer. According to the relative motion between the flow and the blade, rotational effects can stabilize or destabilize the flow. In the case of a wind turbine blade, the tendency is that rotational effects stabilize the flow, specially in the negative pressure gradient zones before separation occurs and on the pressure side of the rotor blade. In a similar manner, this special case has provided the extension for different pressure gradients that form part of the linear stability analysis used for transition prediction. Deep study of the available methods for the extension of the e^n method to 3D flow have been performed, from the available methods for transition prediction in 3D flows, the technique that can be coupled and incorporated in the existing 2D Database is the beta method. Due to

the fact that is consistent in the manner in which disturbance propagate in the boundary layer and also because provide an easy implementation. The numerical solution technique for the stability solution have provide a fast an effective tool. The parametrical study for different wind turbine airfoils has provided a very usefull evaluation of rotational effects (RE) of different stability and operational parameters, has also provide the basis to understand the behaviour of the full rotor geometry. From the simulations on the NM80 rotor and comparison with experiments, is clear that the e^n method can still be used for transition prediction for high turbulence intensity. Naturally it will demand to calibrate the n factor with experiments at varying operational conditions.

6.1 Comments and Future work

The Quasi-3D approximation have provided support to obtain the velocity profiles Database, however, to compare with experiments is required to have a full flow field. The method is usefull for flow calculations, however, it is limited for transition pourposes. Due to the fact that details of the flow are missing, specially for a precise modelling of the crossflow at the attachment line zone. The stability analysis performed on the attached flow region can be easily extended to the separation zone when the base flow computation came from the solution of the (NS) equations or an equivalent technique. From the comparison with experiments it is further suggested to make a tip study effect to be able to match with the experimental results presented in the report. If sufficient experimental data is available for the NM80 rotor or the ECN-25 HAT, will be important to make a similar stability analysis at different wind speed velocities. At relatively high angles of attack, on the pressure side, a great portion of the surface is laminar, and rotational effects (RE) are higher due to the fact that have a sufficient distance to develope. It is further needed to evaluate the effect on the separation bubble close to the trailing edge, that is known to be connected with the noise production. Depending on the type of flow solver, it will be relevant to include a systematic comparison of the available transition techniques and methods on wind turbines rotors. In special, further work can be directed to make use of the envelope method. Finally the Database for transition prediction needs to be implemented in the EllipSys3D code, in a similar manner like the corresponding 2D case, but with the effect of rotation.

Bibliography

[1] Abbott I.H. and Doenhoff A.E. von (2006): Theory of Wing Sections **Ed. Dover**

[2] Alfredsson P.H. and Persson H. (1989): Instabilities in channel flow with system rotation **J. Fluid Mech., vol. 202, pp. 543-557**

[3] Althaus D. (1972): Stuttgarter Profilkatalog **Institut fur Aerodynamik und Gasdynamik der Universitat Stuttgart**

[4] Aref H. , (2006): Stability criteria for parallel viscous flows. **Fundamental problems in fluid dynamics course- Technical University of Denmark**

[5] Arnal D., Casalis G., Jullen J.C. (1989): Experimental and Theoretical Analysis of Natural Transition on "Infinite" Swept Wing **Proceedings on the 3rd IUTAM Symposium on Laminar-Turbulent Transition Toulouse / France**

[6] Arnal D., (1993): Boundary layer Transition: Predictions based on linear theory **Special Course on Progress in Transition Modelling, AGARD-R-793**

[7] Arnal D. Casalis G. (2000): Laminar-Turbulent transition prediction in three-dimensional flows **Progress in Aerospace Sciences 36 173-191**

[8] Arnal D. (2008): Practical Transition prediciton methods: subsonic and transonic flows **Advances in Laminar-Turbulent transition modelling, RTO-AVT 151-VKI Series**

[9] Arnal D. (2008): Attachment line and surface imperfections problems **Advances in Laminar-Turbulent transition modelling, RTO-AVT 151-VKI Series**

[10] Bak C., Madsen H. Aa., Paulsen U.S., Fuglsang P., Romblad J., Oleson N.A., Enevoldsen P., Laursen J., Jensen L.. DAN-AERO MW (2010): Detailed aerodynamic measurements on a full scale MW wind turbine *EWEC 2010*

[11] Bak C., Gaunaa M., Paulsen U., Fuglsang P., Romblad J., Olsen N.A., Enevoldsen P., Laursen J., Jensen L.. DAN-AERO MW (2010): Comparison of airfoil characteristics for two airfoils tested in three different wind tunnels *The science of making torque from wind, Crete, Greece* **June 28-30, 59-79**

[12] Blaser D.A. and Velkoff H.R. (1973) : A preliminary Analytical and Experimental Investigation of Helicopter Rotor Boundary Laters **AIAA Journal Vol.11, No.12, December**

[13] Bæk P. (2008) : Experimental Detection of Laminar to Turbulent Boundary Layer Transition on Airfoils in an Idustrial Wind Tunnel Facility *MEK-FM-EP-2008-12*

[14] Cebeci T., Bradshaw P. (1977): Momentum Transfer in Boundary Layers **Ed. McGraw-Hill**

[15] Cebeci T., Stewartson K. (1980): On Stability and Transition in Three-Dimensional Flows *AIAA J.***18 (4)** 398-405.

[16] Cebeci T., Khattab A. K. and Stewartson K. (1981): Three-dimensional laminar boundary layers and the ok of accessibility **J. Fluid Mech., Vol.107, pp. 57-87**

[17] Cebeci T., Stewartson K. (1981): Asymptotic Properties of the Zarf *AIAA J.* **19 (6)** 806-807.

[18] Cebeci T. and Su W. (1988): Separation of three-dimensional laminar boundary layers on a prolate spheroid **J. Fluid. Mech, Vol. 191, pp. 47-77**

[19] Cebeci T, Chen H. H., Arnal D. and Huang T.T. (1991): Three-Dimensional Linear Stability Approach to Transition on Wings and Bodies of revolution at Incidence **AIAA Journal Vol. 29 No. 12, December**

[20] Cebeci T., Chen H.H. and Kaups K. (1992): Further consideration of the effect of curvature on the stability of Three-Dimensional flows **Computers Fluids Vol.21, No.4, pp.491-502**

[21] Cebeci T., Chen H.H. and Besnard E. (1995): The role of Zarf in Predicting Transition in Three-Dimensional Flows with the Saddle-Point Method **Proceedings of the Colloquium 'Transitional Boundary Layers in Aeronautics' 6-8 Dec Amsterdam**

[22] Cebeci T. (2004): Stability and Transition Theory and Application **Ed. Springer**

[23] Chawla M.D. (1969), The Stability of Boundary Layer Flow subject to rotation **Ph.D. Thesis, Michigan State University**

[24] Chaviaropoulos P.K. and Hansen M.O.L. (2000): Investigationg Three-Dimensional and Rotational Effects on Wind Turbine Blades by Means of a Quasi-3D Navier-Stokes Solver **Journal of Fluid Engineering Vol. 122 pp.330-336, June**

[25] Cooke J.C. and Hall M.G. (1962): Boundary layer in three dimensions **Prog. Aero. Sci Vol.2 pp 222-282**

[26] Dagenhart R.J. (1981) : Amplified Crossflow Disturbances in the Laminar Boundary Layer on Swept Wings With Suction **NASA TP 1902 c.1**

[27] Drela M. (1989): An Analysis and design systems for low Reynolds number airfoils **Conference on low Reynolds number airfoils aerodynamics. Uninersity of Notre Dame, June**

[28] Du Z. , Selig S.M. (2000): The effect of rotation on the boundary layer of a wind turbine blade **Renewable Energy 20 167-181**

[29] Dumitrescu H. and Cardos V. (2004): Rotational Effects on the Boundary-Layer Flow in Wind Turbines **AIAA Vol.42 No.2 pp.408-411**

[30] Dumitrescu H. and Cardos V. (2007): Modelling of inboard stall delay due to rotation **Journal of Physics: Conference series 75 (2007)-012022**

[31] Fischer A., Bertagnolio F., Bak C., Madsen H.A., (2010): Surface Pressure Measurements on a NACA0015 airfoil compared to Computations with the TNO Trailing Edge Noise Model *The science of making torque from wind, Crete, Greece* **June 28-30, 81-92**

[32] Fogarty L.E. and Sears W.R. (1950): Potential Flow Around a Rotating, Advancing Cylindrical Blade **J.Aero.Sci., vol.17, No.9, pp. 599**

[33] Fogarty L.E. (1951): The laminar Boundary layer on a Rotating Blade **J.Aero.Sci., Vol.18 No.4**

[34] Franklin D. Harris (1966): Preliminary Study of Radial Flow Effects on Rotor Blades **Journal of the American Helicopter Soc Vol.11 No.3**

[35] Govindarajan R. (2006): Sixth IUTAM Symposium on Laminar-Turbulent Transition **Ed. Springer**

[36] Gregory N., Stuart J.T., Walker W.S. (1955): On the Stability of Three-Dimensional Boundary Layers with Application to the Flow Due to a Rotating Disk. *JSTOR* **Vol.408 No.943 p.p 155-199**

[37] Gregory N. and Walker, W.S. (1960): Experiments on the effect of suction due to a rotating disk **J. Fluid Mech. 9,225-234**

[38] Groenewoud, G.J.H van; Boermans, L.M.M. and Ingen, J.L. van (1983): Investigation of laminar-turbulent transition of the boundary layer on the 25m HAT wind turbine. (In Dutch) **Report LR-390, Faculty of Aerospace Engineering, TU Delft, 1983**

[39] Henkes R.A.W.M. and Ingen J.L. van (1995): Transitional Boundary Layers in Aeronautics **Proceedings of the Colloquium, 'Transitional Boundary layers in Aeronautics', Amsterdam, 6-8 December**

[40] Hansen A.G , Herzig H.Z. (1956): Cross flow in laminar incompressible boundary layers **NACA-TN-3651**

[41] Hansen A.G. (1964): Similarity Analyses of Boundary Value Problems in Engineering **Ed. Prentice-Hall**

[42] Hansen M.O.L. (2000): Aerodynamics of Wind Turbines **Ed. James X James**

[43] Hansen, M.O.L ; Sørensen, J.N. ; Shen, W.Z. (2003): Vorticity-velocity formulation of the 3D Navier Stokes equations in cylindrical coordinates **Int. J. Numer. Meth. Fluids, vol: 41, pages: 29-45**

[44] Hansen M.O.L. , Michelsen J.A, Sørensen N.N., Johansen J., Hirsch C., Ramboer J., Ekatarinaris J., Voutsinas S., S.Conway (2004): Technical report Knowblade project : WP-1 Improved Power Performance Prediciton **Technical University of Denmark MEK-FM-2004-02**

[45] Hua Y, Shen W.Z. , Sørensen J.N., Zhu W.J. (2010): Determination of the Angle of Attack on the Mexico Rotor using Experimental Data *The science of making torque from wind, Crete, Greece* **June 28-30, 47-57**

[46] Ingen J.L. van (1965): Theoretical and Experimental investigations of Incompressible Laminar Boundary Layers with and without suction. Technological University Delft **Report VTH-124**

[47] Ingen J.L. van (1995):Some Introductory Remarks on Transition Prediction Methods Based on Linear Stability Theory **Proceedings of the Colloquium 'Transitional Boundary Layers in Aeronautics' 6-8 Dec Amsterdam**

[48] Ingen J.L. van, Schepers (2010): Prediction of boundary layer transition on wind turbine blades using e^n method and a comparison with measurements **EWEC 2010 - Abstract- not published**

[49] Johansen J. and Sørensen J.N. (1999): Prediction of Laminar/Turbulent Transition in Airfoils Flows **J. Aircraft, Vol. 36, No.4 pp. 731-734**

[50] Karimipanah M. T., Olsson E. (1993): Calculation of Three-Dimensional Boundary layers on Rotor Blades Using Integral Methods **Journal of Turbomachinery pp. 342-353 Vol.115, April**

[51] Keller, H.B. (1974): Accurate difference methods for non-linear two-point boundary value problems **SIAM J. Numer. Anal. Vol.11, No.2 pp. 305-320**

[52] Kreplin H-P., Vollmers H., Meier H.U. (1982): Measurements of the Wall Shear Stress on an Inclined Prolate Spheroid **Z. Flugwiss. Weltraumforsch. 6, Heft 4 pp. 248-252**

[53] Koyama H., Masuda S., Ariga I., Watanabe I. : (1979) Stabilizing and Destabilizing Effects of Coriolis Force on Two-Dimensional Laminar and Turbulent Boundary Layers **Journal of Engineering for Power Vol. 101, January**

[54] Kohama Y.P. (2000): Three-dimensional boundary layer transition study **Current Science, Vol. 79, No.6, 25 sep**

[55] Kierzenka J., Shampine L. F. (2001): A BVP Solver based on Residual Control and the MATLAB PSE **ACM Vol.27 (3)**

[56] Lakshminarayana B. and Govindat T.R. (1981): Analysis of Turbulent Boundary Layer on Cascade and Rotor Blades of Turbomachinery **AIAA Journal Vol.19 No.10, pp. 1333-1341**

[57] Lin R-S. and Reed H.L. (1993): Effect of Curvature on Stationary Crossflow Instability of a Three-Dimensional Boundary layer **AIAA Journal Vol.31, No.9, September**

[58] Lighthill M.J. (1952) : On sound generated aerodynamically: I.General Theory. *Proceedings of the Royal Society of London, Series A (Mathematical and Physical Sciences)* **211** 564-587.

[59] Lingwood R.J. (1995): Stability and Transition of the Boundary Layer on a Rotating Disk **Cambridge University PhD Dissertation, PhD 20020**

[60] Lingwood R.J. (1995): Absolute instability of the boundary layer on a rotating disk **J. Fluid Mech., vol. 299, pp. 17-33**

[61] Lingwood R.J. (1996): An experimental study of absolute instability of the rotating-disk bondary-layer flow **J. Fluid Mech., vol. 314, pp. 373-405**

[62] Lingwood R.J. (1999): On the application of the e^n method to three-dimensional boundary-layers flows **Eur. J. Mech B/Fluids 18 581-620**

[63] Mack L.M. (1979): On the Stability of the Boundary layer on a Transonic Swept Wing **17th Aerospace Sciences Meeting AIAA Paper 79-0264**

[64] Mack L.M. (1979): Three-Dimensional Effects in Boundary-Layer Stability in **"Twelfth Symposium on Naval Hydrodynamics", pp. 63-76, National Academy of Sciences, Washington, D.C.**

[65] Mack L.M. (1984): Boundary-Layer Linear Stability Theory **Special Course on Stability and Transition of Laminar Flow AGARD Report No.709**

[66] Mack L.M. (1988): Stability of Three-Dimensional Boundary Layers on Swept Wings at Transonic Speeds **IUTAM Symposium Transsonicum III, Gottingen**

[67] Madsen H. Aa and Bak C., Paulsen U.S., Gaunaa M., Sørensen N.N., Fuglsang P., Romblad J. and Olsen N.A., Enevoldsen P. and Laursen J. , and Jensen L. (2010): The DAN-AERO MW Experiments **AIAA 2010-645**

[68] Mager A. (1951): Generalization of the Boundary-Layer Momentum-Integral equations to three-dimensional flows including those of rotating system **NACA TN 1067**

[69] Masuda S. and Matsubara M. (1989): Visual Study of Boundary Layer Transition on Rotating Flat Plate **Proceedings on the 3rd IUTAM Symposium on Laminar-Turbulent Transition Toulouse / France**

[70] Martinez H.G.G., Shen W.Z. , Sørensen J.N. (2007): 3D boundary layer study on a rotating wind turbine blade **Journal of Physics: Conference series 75 (2007)-012032**

[71] Matsson J.E.O. and Alfredsson P.H. (1990): Curvature- and rotation-induced instabilities in channel flow **J. Fluid Mech., vol. 210, pp. 537-563**

[72] Matubara M. and Masuda S. (1991) : Three-Dimensional Instability in Rotating Boundary Layer **FED-Vol. 114, Boundary Layer Stability and Transition to Turbulence ASME**

[73] McCroskey W.J. (1971): Measurements of Boundary Layer Transition, Separation and Streamline direction on rotating blades **NASA TN D-6321**

[74] McCroskey W.J. and Dwyer H.A. (1970): Methods of Analyzing propeller and rotor Boundary Layers with cross flow **NASA-SP-228**

[75] Michelsen J.A (1988) : General curvilinear transformation of the Navier-Stokes equations in a 3D polar rotating frame **Danmarks Tekniske Universitet, ET-AFM 98-01**

[76] Meier H.U. and Kreplin H-P. (1980): Experimental Investigation of the Boundary Layer Transition and Separation on a Body of Revolution **Z. Flugwiss. Weltraumforsch. 4, Heft 2 pp.65-71**

[77] Mikkelsen R., Michelsen J.A., Sørensen J.N., Andersen P. (2002): Modelling of 3D Transition for Computations on Ship Propellers **Technical University of Denmark, G3RD-CT-2002-00818**

[78] Nayfeh A.H. :(1980): Stability of Three-Dimensional Boundary Layers *AIAA J.* **18 (4)** 406-415

[79] Olsen N.A. (1994): Laminar/Turbulent Omslagsmodel for Granselagstromninger **Danmarks Tekniske Hojskole , AFM-EP-94-02**

[80] Ozgen S. (2004) :Effect of heat transfer on stability and transition characteristics of boundary-layers *International Journal of Heat and Mass Transfer* **47 4697- 4712**

[81] Pedersen E.D. (1991): Granselagsstabilitet **Danmarks Tekniske Hojskole , AFM-EP-91-01**

[82] Potter M.C. and Chawla M.D. (1971): Stability of Boundary layer Flow Subject to Rotation **The Physics of Fluids Volume 14, Number 11**

[83] Pretsch J. (1941) : The Stability of a two-Dimensional Laminar Flow in Pressure Drop and Pressure Rise. Jahrb d. DL I p.58.

[84] Pretsch J. (1952): The excitation of unstable perturbations in a laminar friction layer **NACA TM 1343**

[85] Prokop R.M., Finlay W.H. and Chen P. (1995) : The Development and linear stability of rotating Boundary layers **Transactions of the Canadian Society for Mechanical Engineers Vol. 19, No. 4**

[86] Reed H.L and Saric W.S., Daniel Arnal (1996): Linear Stability Theory applied to Boundary Layers **Ann. Rev. Fluid. Mech. 28:389-428**

[87] Reed H.L. and Saric W.S. (1989): Stability of Three-Dimensional Boundary layer **Ann. Rev. Fluid. Mech. 21:235-84**

[88] Reshotko E. (2008): Paths to transition in wall layers **Advances in Laminar-Turbulent transition modelling, RTO-AVT 151-VKI Series**

[89] Saric W.S. (2008): Experiments in 2-D Boundary-Layers: Stability and receptivity **Advances in Laminar-Turbulent transition modelling, RTO-AVT 151-VKI Series**

[90] Schlichting H. (1968): Boundary-Layer Theory **Ed. McGraw-Hill, Sixth Edition**

[91] Schmid P.J., Henningson D.S. (2001): Stability and Transition in Shear Flows **Ed. Springer**

[92] Schrauf G. (1994): Transition prediction using different Linear Stability Analysis Strategies **AIAA-94-1848-CP**

[93] Schrauf G. (1992): Curvature effects for three-dimensional compressible boundary-layer stability **Z. Flugwiss. Weltraumforsch. 16, 119-127**

[94] Schrauf G. (2004): Large-Scale Laminar-Flow Test Evaluated with Linear Stability Theory **Journal of Aircraft Vol.41, No.2 March-April**

[95] Schrauf G., Perraud J., Lam F., Stock H.W., Vitiello D., Abbas A. (1996): Transition Prediction with Linear Stability Theory - Lessons Learned from the ELFIN F100 Flight Demonstrator **Proceedings of the 2nd European Forum on Laminar Flow Technology, AAAF Rep., pp. 8-58 - 8-71**

[96] Schubauer G.B. and Skramstad H.K. (1947): Laminar Boundary-Layer Oscillations and Transition on a Flat Plate, National Bureau of Standards **RP1722 Volumen 38, Feb**

[97] Sears W.R. (1950): Potential Flow Around a Rotating Cylindrical Blade **J.Aero.Sci., Vol.17 No.3 pp. 183-184**

[98] Smith A.M.O. (1956): Transition, Pressure gradient, and Stability theory **9th International Congress, Brussels Vol.4**

[99] Snel H. (1990): Scaling Laws for the Boundary Layer Flow on Rotating windturbine Blades **Proceedings of the Fourth IEA Symposium on the Aerodynamics of Wind Turbines, ETSU-N-118, Rome**

[100] Snel H., Houwink R. and Piers W.J. (1992): Sectional Prediction of 3D effects for separated flow on rotating blades **Proceedings of the Sixth IEA Symposium on the Aerodynamics of Wind Turbines, ETSU-N-125, Petten, Holland**

[101] Shen W. Z. and Sørensen J.N. (1999): Quasi-3D Navier-Stokes Model for Rotating Airfoil **Journal of Computational Physics 150, 518-548**

[102] Shen W.Z. , Sørensen J.N. and Mikkelsen R.F (2005) : Tip Loss Correction for Actuator/Navier-Stokes Computations *Journal od Solar Energy Engineering* **MAY 2005, Vol. 127 209-213**

[103] Shen W.Z., Hansen M.O.L., Sørensen J.N. (2009): Determination of the Angle of Attack on Rotor Blades *Wind Energy* **12: 91-98**

[104] Stock H.W. and Seitz A. (2004): Crossflow-Induced Transition Prediction Using Coupled Navier-Stokes and e^n Method Computations **AIAA Journal Vol.42 No. 9 September**

[105] Stock H. W. (2006): e^n Transition Prediciton in Three-Dimensional Boundary Layers on Inclined Prolate Spheroids **AIAA Journal Vol.44, No.1**

[106] Stock H.W. & E. Degenhart, (1989) : A Simplified e^n method for transition prediction in two-dimensional, incompresible boundary layers. **Z. Flugwiss. Weltraumforsch 13, 16-30**

[107] Sørensen J.N. (1986): Three-Level, Viscous-Inviscid Interaction technique technique for the prediction of separated flow past rotating wing **Danmarks Tekniske Hojskole, AFM 86-03**

[108] Sørensen N.N. (1995): General Purpose Flow Solver Applied to Flow over Hills **Ris-R-827-(EN), Ris National Laboratory, Roskilde, Denmark, June**

[109] Sørensen N.N. (2002): Transition Prediction on the NORDTANK 500/41 Turbine Rotor **Riso-R-1365(EN)**

[110] Tanner W. H., Yaggy P.F. (1966): Experimental Boundary Layer Study on Hovering Rotors **Journal of the American Helicopter Society Vol. 11 No.3**

[111] Tobak M. and Peake D.J. (1982): Topology of three-dimensional separated flows **Ann. Rev. Fluid Mech. 14:61-85**

[112] A.R. Wazzan A.R., Okamura T.T. and Smith A.M.O. (1968): Spatial and Temporal Stability Charts for the Falkner-Skan Boundary-Layers Profiles **Report NO. DAC-67086**

[113] A.R.Wazzan (1975) : Spatial Stability of Tollmien-Schlichting Waves **Prog. Aerospace Sci Vol. 16, No. 2, pp. 99-127**

[114] White F.M. (2006): Viscous Fluid Flow **Ed. McGraw-Hill, Third Edition**

[115] Yohner P.L. and Hansen A.G. (1958): Some numerical solutions of Similarity equations for Three-Dimensional Laminar Incompressible Boundary Layers **NACA TN 4370**